



저작자표시-비영리-변경금지 2.0 대한민국

이용자는 아래의 조건을 따르는 경우에 한하여 자유롭게

- 이 저작물을 복제, 배포, 전송, 전시, 공연 및 방송할 수 있습니다.

다음과 같은 조건을 따라야 합니다:



저작자표시. 귀하는 원저작자를 표시하여야 합니다.



비영리. 귀하는 이 저작물을 영리 목적으로 이용할 수 없습니다.



변경금지. 귀하는 이 저작물을 개작, 변형 또는 가공할 수 없습니다.

- 귀하는, 이 저작물의 재이용이나 배포의 경우, 이 저작물에 적용된 이용허락조건을 명확하게 나타내어야 합니다.
- 저작권자로부터 별도의 허가를 받으면 이러한 조건들은 적용되지 않습니다.

저작권법에 따른 이용자의 권리는 위의 내용에 의하여 영향을 받지 않습니다.

이것은 [이용허락규약\(Legal Code\)](#)을 이해하기 쉽게 요약한 것입니다.

[Disclaimer](#)

Doctoral Thesis

All-Solid-State Lithium-Ion Batteries using
Sheet-Type Electrodes and Solid Electrolyte
Films and Their Diagnostic Study

Young Jin Nam

Department of Energy Engineering
(Battery Science and Technology)

Graduate School of UNIST

2019

All-Solid-State Lithium-Ion Batteries using Sheet-Type Electrodes and Solid Electrolyte Films and Their Diagnostic Study

Young Jin Nam

Department of Energy Engineering
(Battery Science and Technology)

Graduate School of UNIST

All-Solid-State Lithium-Ion Batteries using Sheet-Type Electrodes and Solid Electrolyte Films and Their Diagnostic Study

A dissertation
submitted to the Graduate School of UNIST
in partial fulfillment of the
requirements for the degree of
Doctor of Philosophy

Young Jin Nam

12 / 07 / 2018

Approved by



Advisor

Youngsik Kim

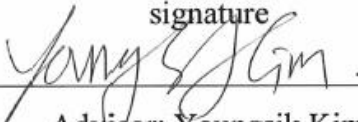
All-Solid-State Lithium-Ion Batteries using Sheet-Type Electrodes and Solid Electrolyte Films and Their Diagnostic Study

Young Jin Nam

This certifies that the dissertation of Young Jin Nam is approved.

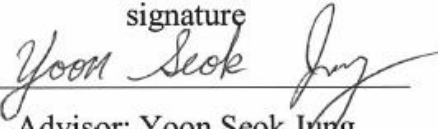
12 / 07 / 2018

signature



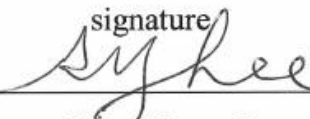
Advisor: Youngsik Kim

signature



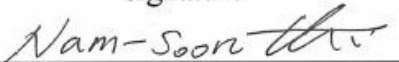
Advisor: Yoon Seok Jung

signature



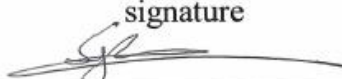
Sang-Young Lee

signature



Nam-Soon Choi

signature



Seok Ju Kang

Abstract

Bulk-type all-solid-state lithium batteries (ASLBs) using sulfide solid electrolytes (SEs) are considered as a promising candidate to solve the safety issues originating from the use of flammable organic electrolytes. Moreover, several state-of-the-art sulfide solid electrolytes shows extremely high ionic conductivity over 10^{-2} S cm⁻¹, compared to conventional liquid electrolytes. However, to develop bulk-type ASLBs, it encountered many technical challenges such as huge interfacial resistances between active materials and SEs, high contents of SEs in ASLBs, scalable fabrication and reliable test protocol. To fulfill these requirements, sheet-type ASLBs using a scalable wet-slurry process can provide a breakthrough in the architecture and fabrication of composite structure.

The first part of my thesis is sheet-type ASLBs using bendable solid electrolyte films and dry-/slurry- mixed electrodes, which are prepared by wet-slurry process. In the first case, the facile and scalable fabrication of bendable solid electrolyte films reinforced with a mechanically compliant NW-scaffold, which enables the fabrication of free-standing and stackable ASLBs with high energy density and high rate capabilities. For the second case, the comparative study for electrodes fabricated by dry- and slurry- mixing process was performed. The information provides insights for a need to develop well-designed electrode with better ionic contacts and to improve the ionic conductivity of SEs. Pouch-type 80 x 60 mm² all-solid-state LiNi_{0.6}Co_{0.2}Mn_{0.2}O₂/graphite full-cells fabricated by the slurry process show high cell-based energy density (184 W h kg⁻¹ and 432 W h L⁻¹). Furthermore, their excellent safety is also demonstrated by simple tests (cutting with scissors and heating at 110°C).

The second part is a reliable electrochemical analysis of sheet-type ASLBs. Even though the well-developed sheet-type ASLBs using sulfide SEs have been demonstrated, their reliable electrochemical test protocols have not been developed. In this regard, in this study, from the in-depth study of ASLBs using novel bulk-type all-solid-state three-electrode cells, even for the cells having thin SE layers, kinetic behaviors of Li-In(-SE) CE and internal short circuits (ISC) by penetrating growth of Li metal during charging at high C-rates are revealed. In addition, unique durability of LiNi_{0.6}Co_{0.2}Mn_{0.2}O₂/graphite or LiNi_{0.6}Co_{0.2}Mn_{0.2}O₂/Si-C full-cells upon discharge to 0 V was described.

In the last study, the pressure monitoring system for sheet-type ASLBs is demonstrated. The state-of-charge (SOC) values were estimated from volume changes of graphite electrodes in LiNi_{0.6}Co_{0.2}Mn_{0.2}O₂/graphite full-cells. The behavior of rearrangement of particles in electrode during cycling is also observed.

These results hold great promise for practical sheet-type all-solid-state technology in terms of fabrication and battery architecture as well as provision of in-depth insights into developing reliable electrochemical test protocols.

Acknowledgements

I would foremost like to express my sincere gratitude to my advisor, Prof. Yoon Seok Jung, whose support and passion have made the completion of my Ph.D study. I could not have imagined having a better advisor and mentor for my Ph.D study.

Besides my advisor, I would like to thank the rest of my thesis committee: Prof. Youngsik Kim, Prof. Sang-Young Lee, Prof. Nam-Soon Choi, and Prof. Seok Ju Kang, for their insightful comments and encouragement, but also for the hard question which incited me to widen my research from various perspectives.

I am also grateful to our group people, Dong Hyun Kim, Sung Hoo Jung, Dae Yang Oh, Hiram Kwak, A Reum Ha, Woo Hyun An, Han Ah Lee for making my pleasurable memories. Especially, I am thankful to Dr. Kern Ho Park, whose advice always cheered me up whenever I struggled.

Most of all, I cannot thank enough to my parents and brother for their endless love and support.

Contents

Abstract	i
List of Figures	vi
List of Tables	xiv
Nomenclature	xv
1. Introduction	1
2. Background	5
2.1. Principle of Lithium Secondary Batteries	5
2.2. Overview of Bulk-Type Inorganic All-Solid-State Lithium Batteries	7
2.2.1. Conductivity of Solid Electrolytes	7
2.2.2. Electrochemical Stability of Solid Electrolytes	8
2.2.3. Interface Compatibility between Active Materials and Solid Electrolytes	9
2.2.4. Electrochemical test protocol for All-Solid-State Lithium Batteries	9
3. Experimental	12
3.1. Preparation of materials	12
3.2. Materials characterization	12
3.3. Electrochemical characterization	14
4. Results and Discussion	20
4.1. Sheet-Type Electrodes & Solid Electrolyte Films	20
4.1.1. Solid Electrolyte Films	20
4.1.1.1. Properties of Solid Electrolyte Films	21
4.1.1.2. Sheet-Type All-Solid-State Lithium-Ion Batteries using Solid Electrolyte Films	32
4.1.2. Sheet-Type Electrodes	44
4.1.2.1. Comparison of Electrodes Fabricated by Dry-mixing and Wet-slurry processes	45
4.1.2.2. Electrodes Fabricated by Premixing Process	62
4.1.2.3. Practical All-Solid-State NCM622/Gr Full-Cells	66
4.2. Diagnostic Study for Sheet-Type All-Solid-State Lithium-Ion Batteries	70
4.2.1. All-Solid-State Three-Electrode Cells	70

4.2.1.1. Reliable Electrochemical Test Protocols for All-Solid-State Half-Cells (Sn/Li-In) ----	72
4.2.1.2. Internal Short-Circuit Behavior for All-Solid-State Full-Cells (NCM/Gr) -----	82
4.2.1.3. 0 V dischargeability for All-Solid-State Full-Cells (NCM/G and NCM/Si-C) -----	94
4.2.2. Pressure Monitoring System -----	99
4.2.2.1. SOC Estimation of Graphite Electrode from Pressure Change of NCM/Gr full-cells -	100
4.2.2.2. Rearrangement of Particles in Electrodes During Cycling -----	109
5. Conclusion -----	113
References -----	114

List of Figures

Figure 1. Schematic diagram of the working principle of lithium ion battery.

Figure 2. Schematic diagram of a typical bulk-type all-solid-state cell.

Figure 3. Schematic diagram of bulk-type three-electrode all-solid-state cells.

Figure 4. Schematic diagram of the operando stress measurement of bulk-type all-solid-state batteries.

Figure 5. Schematic diagram showing the fabrication of bendable sulfide NW-SE films with two different structures (SE-NW-SE and NW-SE-NW). FESEM and photo images are also provided.

Figure 6. TGA curve of PTTA NW under Ar.

Figure 7. Photo and FESEM images of the poly(paraphenylene terephthalamide) (PPTA) NW scaffold.

Figure 8. a) Photo images of the conventional SE pellet and bendable NW-SE films. The pellets have a diameter of 1.3 cm. Note the cracks in the conventional SE pellet, as indicated by the arrow. b) Photo images of 3×3 cm² bendable NW-SE films (NW-SE-NW). c) Photo and FESEM images of 1.5×2.0 cm² bendable NW-SE films (NW-SE-NW) before and after bending tests. The diameter of rods is provided. Li₃PS₄ (LPS) was used as the SE.

Figure 9. FESEM images of the a) LPS powders and b-d) cold-pressed pellets.

Figure 10. First two charge-discharge voltage profiles of the a) LiTiS₂/Li-In (LTS/Li-In) and b) Li₄Ti₅O₁₂/Li-In (LTO/Li-In) all-solid-state cells at 30 °C. The current densities of the LTS/Li-In and LTO/Li-In cells were 50 mA g_{LTS}⁻¹ (55 μA cm⁻²) and 22 mA g_{LTO}⁻¹ (55 μA cm⁻²), respectively.

Figure 11. a) Variations in discharge capacities versus cycle number, and b) discharge voltage profiles at different C-rates of LiTiS₂/Li₄Ti₅O₁₂ (LTS/LTO) all-solid-state cells using the conventional SE pellet and bendable NW-SE films as the SE layer at 30 °C.

Figure 12. a) Nyquist plots of LiTiS₂/Li₄Ti₅O₁₂ (LTS/LTO) all-solid-state cells using the conventional SE pellet and bendable NW-SE films as the SE layer at 30 °C. Voigt-type equivalent circuit models used

for fitting the EIS results for b) the SE and the SE-NW-SE cells and c) the NW-SE-NW cell in Figure 12a. The solid lines indicate the fitting results using Voigt-type equivalent circuit model.

Figure 13. First charge-discharge voltage profiles of the prototype free-standing LTS/LTO sheet battery at $89 \mu\text{A cm}^{-2}$ at $30 \text{ }^\circ\text{C}$. A photo image of the LTS/LTO sheet battery is shown in the inset.

Figure 14. First two charge-discharge voltage profiles of the a) $\text{LiCoO}_2/\text{Li-In}$ (LCO/Li-In) and b) $\text{Li}_4\text{Ti}_5\text{O}_{12}/\text{Li-In}$ (LTO/Li-In) all-solid-state cells at $30 \text{ }^\circ\text{C}$. The results of the pristine and heat-treated LCO are compared. The current densities of the LCO/Li-In and LTO/Li-In cells were $14 \text{ mA g}_{\text{LCO}}^{-1}$ (0.11 mA cm^{-2}) and $12 \text{ mA g}_{\text{LTO}}^{-1}$ (0.11 mA cm^{-2}), respectively.

Figure 15. a) Schematic diagram, b) cross-sectional FESEM image and EDS elemental maps, and c) photo images of the free-standing $\text{LiCoO}_2/(\text{SE-NW-SE})/\text{Li}_4\text{Ti}_5\text{O}_{12}$ (LCO/(SE-NW-SE)/LTO) all-solid-state cell.

Figure 16. First charge-discharge voltage profiles of the free-standing LCO/LTO all-solid-state mono-cells with different-structured SE films (SE-NW-SE, NW-SE-NW, pNW-SE-pNW) and the free-standing bipolar cell constructed by stacking two free-standing mono-cells (LCO/(SE-NW-SE)/LTO) at $14 \text{ mA g}_{\text{LCO}}^{-1}$ ($= 0.11 \text{ mA cm}^{-2}$) at $30 \text{ }^\circ\text{C}$.

Figure 17. Cycle performances of the free-standing LCO/LTO all-solid-state cells. The data using 0.35 wt.% of LiNbO_3 -coated LCO with the bendable NW-LPS-NW film is also represented for comparison.

Figure 18. a) FESEM image and elemental maps of the PEO/LiTFSI-coated NW (pNW). b) Bright-field and c) dark-filed images of the FIB-cross-sectioned pNW. The line scanning energy dispersive spectroscopy (EDS) result for S $\text{K}_{\alpha 1}$ signal is also provided. The arrows indicate the coating layers.

Figure 19. Comparison of the energy densities of the all-solid-state battery as a function of the overall weight fraction of SEs varied by electrode chemistry (Ref. 122) and , the presence of SE coating (Ref. 24), and the bendable NW-SE films

Figure 20. Comparison of all-solid-state lithium-ion battery (ASLB) electrodes fabricated by dry-mixing and wet-slurry processes. Photographs of a) a dry-mixture of active materials, SEs, and super C65 without polymeric binders and b) a slurry comprised of active materials, SEs, super C65, and polymeric binders in xylene. c) Sheet-type NCM622 electrode fabricated by the wet-slurry process.

Schematic diagrams representing the microstructures of ASLB electrodes a) by dry-mixing process without binders and b) by wet-slurry process using binders. Active materials, SEs, super P, and polymeric binders (NBR) are shown in gray, yellow, black, and green, respectively.

Figure 21. a) Raman and b) FTIR spectra for NBR.

Figure 22. a) XRD pattern and b) Arrhenius plot of Li-ion conductivity for as-prepared $\text{Li}_6\text{PS}_5\text{Cl}$. The Bragg position for argyrodite $\text{Li}_6\text{PS}_5\text{Cl}$ (CIF no. 418490) is shown in a panel a. Conductivity after exposure to anhydrous xylene is also provided in a panel b.

Figure 23. First-cycle charge-discharge voltage profiles at 0.1C and 30 °C for all-solid-state NCM622/Li-In half-cells employing dry- and slurry-mixed electrodes with a) the lower mass loading and b) the higher mass loading of NCM622.

Figure 24. FESEM images of a) NCM622 and b) graphite. c) The EDXS elemental maps of Ni and Nb for NCM622, which correspond with (a).

Figure 25. First-cycle discharge capacity for the dry- and slurry-mixed NCM622 electrodes as a function of weight fraction of active materials. The NCM622/Li-In all-solid-state half-cells were cycled between 3.0-4.3 V (vs. Li/Li⁺) at 0.1C and 30 °C. The data were plotted from those in Figure 23.

Figure 26. Cross-section FESEM images of a) dry- and b) slurry-mixed electrode with 85 wt.% of active materials and their corresponding EDXS elemental maps for Ni, sulfur, and nitrogen.

Figure 27. Discharge capacities for all-solid-state NCM622/Li-In half-cells cycled between 3.0-4.3 V (vs. Li/Li⁺) varied by C-rates at 30 °C. The C-rates for charge and discharge were the same.

Figure 28. Discharge capacities as a function of cycle number varied by different C-rates for the NCM622 electrodes fabricated by a) dry-mixing and b) wet-slurry processes. The NCM622/Li-In all-solid-state half-cells were cycled between 3.0-4.3 V (vs. Li/Li⁺) at 30 °C.

Figure 29. FESEM surface images of NCM622 electrodes fabricated by dry-mixing process with a) ~70 wt.% (D70) and b) ~85 wt.% of NCM622 (D85) and wet-slurry process using NBR with c) ~70 wt.% (W70) and d) ~85 wt.% (W85) of NCM622. Their corresponding EDXS elemental maps for sulfur are also shown.

Figure 30. Nyquist plots at 30 °C for all-solid-state NCM622/Li-In half-cells employing dry- and slurry-mixed electrodes with a) the lower mass loading and b) the higher mass loading.

Figure 31. a) Equivalent circuit model for NCM622/Li-In all-solid-state half-cells. b) Resistance values (R_2 in a panel a) as a function of weight fraction of active materials for the dry- and slurry-mixed NCM622 electrodes. The data were obtained from Nyquist plots in Figure 30.

Figure 32. Transient discharge voltage profiles at 30 °C and their corresponding polarization (ΔV) curves for all-solid-state NCM622/Li-In half-cells employing dry- and slurry-mixed electrodes with a) ~70 wt.%, b) ~80 wt.%, and c) ~85 wt.% NCM622, obtained by GITT. The enlarged view where QOCV and CCV are indicated is shown in the inset in a. The polarization data were plotted by subtracting CCV from QOCV in the transient voltage profiles in transient discharge voltage profiles.

Figure 33. Results of NCM622 electrodes fabricated by wet-slurry process using a premixed powder of NCM622 and SEs. a) Schematic diagram of premixing process for NCM622 and SE powders by mechanical milling. b) XRD patterns of $\text{Li}_6\text{PS}_5\text{Cl}$, pristine NCM622, and NCM622 premixed with $\text{Li}_6\text{PS}_5\text{Cl}$. c) Cross-sectional FESEM images of wet-mixed NCM622 electrodes without and with premixing process and their corresponding EDXS elemental maps for Ni (red) and sulfur (green).

Figure 34. Electrochemical performances of NCM622 electrodes fabricated by wet-slurry process using a premixed powder of NCM622 and SEs. a) First-cycle charge-discharge voltage profiles at 0.1C, b) Nyquist plots, and c) transient discharge voltage profiles and their corresponding polarization (ΔV) curves for slurry-mixed NCM622 electrodes without and with premixing process, and their corresponding polarization curves.

Figure 35. Discharge capacities as a function of cycle number varied by different C-rates for the NCM622 electrodes fabricated by wet-slurry process without and with pre-mixing. The NCM622/Li-In all-solid-state half-cells were cycled between 3.0-4.3 V (vs. Li/Li^+) at 30 °C.

Figure 36. First-cycle charge-discharge voltage profiles for the wet-slurry fabricated graphite electrode at 0.025C and 30 °C. The composition of graphite, SE, and NBR was 58.6:39.1:2.3 weight ratio. The mass loading of the graphite electrode was 18 mg cm^{-2} .

Figure 37. Results of NCM622/graphite all-solid-state full-cells. a) Photograph of $80 \times 60 \text{ mm}^2$ pouch-

type NCM622/graphite full-cell and its cross-sectional FESEM image. b) First-cycle charge-discharge voltage profiles of pelletized and pouch-type full-cells of NCM622/graphite at 0.025C. The pelletized cell and pouch-cell were tested at 30 °C and 25 °C, respectively. The detailed specifications are provided in Table 4. Photographs of 80 × 60 mm² pouch-type NCM622/graphite all-solid-state full-cells c) after cutting with scissors and d) being placed on the hot plate at 111 °C for > 1 h.

Figure 38. First-cycle discharge-charge voltage profiles for Sn/Li-In all-solid-state cells with two different electrode mass loadings.

Figure 39. First two-cycle discharge-charge voltage profiles Sn/Li cells using liquid electrolytes at 0.054 and 0.27 mA cm⁻² at the first and second cycle, respectively.

Figure 40. Results for two different types of all-solid-state three-electrode cells. Schematics of all-solid-state three-electrode cells are shown in Figure 3a) type 1 (referred to as “cell-1”) and b) type 2 (referred to as “cell-2”). a) Discharge-charge voltage profiles for Sn/Li-In all-solid-state three-electrode cells at different current densities. b) Discharge-charge voltage profiles of each electrode for Sn/Li-In all-solid-state three-electrode cells at 0.045 mA cm⁻².

Figure 41. Comparison of the discharge-charge voltage profiles of each electrode for Sn/Li-In all-solid-state three-electrode cells using Li_{0.5}In or Li metal as REs.

Figure 42. Electrochemical results for Sn/Li-In(-SE) all-solid-state three-electrode cells with different CEs (counter electrodes). a) Discharge-charge voltage profiles (WE vs. CE) for the cells with different CEs where three different weight ratios of Li_{0.5}In/SE were used. The numbers indicate the current density in mA cm⁻². b) Discharge-charge voltage profiles for each electrode at 0.11 mA cm⁻². The arrows indicate the terminal voltage of CEs (Li_{0.5}In or Li_{0.5}In-SE) upon discharge (delithiation for CEs). c) Terminal voltage for CEs (Li_{0.5}In or Li_{0.5}In-SE) upon discharge (delithiation for CEs) as a function of current density, which is plotted from the data in (b) and Figure 43.

Figure 43. Discharge-charge voltage profiles of each electrode for Sn/Li-In all-solid-state three-electrodes with different CEs using three different weight ratios of Li_{0.5}In/SE. The results of cycling at four different current densities are shown. Figure 42b corresponds with (a).

Figure 44. Cross-sectional FESEM images for a) Li_{0.5}In and b) Li_{0.5}In-SE (20 wt% of SE) CEs and their corresponding EDXS elemental maps.

Figure 45. Results for concentration of Li^+ ions in cross-sectioned CEs ($\text{Li}_{0.5}\text{In}$ or $\text{Li}_{0.5}\text{In-SE}$ with 80:20 weight ratio) for Sn/Li-In(-SE) all-solid-state cells. Cross-sectional TOF-SIMS maps of Li^+ ions for a) $\text{Li}_{0.5}\text{In}$ and b) $\text{Li}_{0.5}\text{In-SE}$ CEs. The dashed lines indicate the outer surface of CEs. A scale bar with the maximum ion counts in a.u. is displayed in the right of (b). Schematics showing concentration of Li^+ ions in cross-sectioned a) $\text{Li}_{0.5}\text{In}$ and b) $\text{Li}_{0.5}\text{In-SE}$ CEs.

Figure 46. Cross-sectional FESEM images and the corresponding EDXS elemental maps for NCM/Gr all-solid-state full-cells using thin SE layer (50–60 μm).

Figure 47. Electrochemical performances of NCM/Li-In, Gr/Li-In-SE, and Si-C/Li-In-SE all-solid-state cells. First two-cycle voltage profiles of a) NCM/Li-In, c) Gr/Li-In-SE, and e) Si-C/Li-In-SE all-solid-state cells at 0.1C, 0.1C, and 0.11 mA cm^{-2} , respectively. The corresponding rate capabilities for a) NCM/Li-In, c) Gr/Li-In-SE, and e) Si-C/Li-In-SE all-solid-state cells are shown.

Figure 48. Results for NCM/Gr all-solid-state three-electrode cells employing thin SE layers (50–60 μm), suffering from ISC by penetrating growth of Li metal. a) Charge-discharge voltage profiles and the corresponding differential capacity plots at different C-rates. Note the abnormal plateaus plotted in red during charge at high C-rates. b) Transient charge-discharge voltage profiles for each electrode at different C-rates. Note the voltage region of Gr, which is lower than 0 V (vs. Li/Li^+) at high C-rate, 1C, shown in thick red line.

Figure 49. Transient charge-discharge voltage profiles of each electrode for NCM/Gr all-solid-state three-electrode cells at different current densities. Note the voltage region of Gr, which is lower than 0 V (vs. Li/Li^+) at high C-rate, 1C, shown in bold red line.

Figure 50. a) Charge-discharge voltage profiles and their corresponding differential capacity plots for NCM/Li all-solid-state cells at 30 $^{\circ}\text{C}$ and various C-rates. b) Charge and discharge capacity varied by C-rates and the corresponding Coulombic efficiency as a function of cycle number. Note the abnormal plateau plotted in red at 1C in (a) and the corresponding low Coulombic efficiencies in (b), indicating the soft ISC by penetrating growth of Li metal.

Figure 51. First-cycle discharge (lithiation) voltage profiles for Gr/Li-In all-solid-state cells at different C-rates, which were used for ^7Li MAS NMR spectroscopy measurements (Figure 51b). After the discharge, the mixtures of SE layers and Gr electrodes, collected from the disassembled cells, were

subjected to the ^7Li MAS NMR spectroscopy measurements. Results for NCM/Gr all-solid-state three-electrode cells employing thin SE layers (50–60 μm), suffering from ISC by penetrating growth of Li metal. a) ^7Li MAS-NMR spectra for the mixtures of SE layers and Gr electrodes collected from the Gr electrodes after lithiation at 0.1C or 2C. The corresponding voltage profiles are provided in Figure 51a. b) Schematic illustrating Gr/Ni-NW/Li-In all-solid-state three-electrode cells and c) the corresponding transient charge-discharge voltage profiles at 2C for Gr and Ni-NW electrodes. While the current flows between Gr and Li-In electrodes, the voltage of Ni-NW electrodes was measured to detect the ISC.

Figure 52. Schematic showing the ISC induced by penetration of Li metal for NCM/Gr all-solid-state cells during charge at high C-rates.

Figure 53. Results for NCM/Gr all-solid-state three-electrode cells employing thick SE layers (730 μm), being free from ISC. a) Charge-discharge voltage profiles and the corresponding differential capacity plots at different C-rates. b) Charge-discharge voltage profiles for each electrode at different C-rates. Note the voltage region of Gr which is lower than 0 V (vs. Li/Li^+) at high C-rate, 1C, shown in bold red line.

Figure 54. Cross-sectional FESEM images and their corresponding EDXS elemental maps for a) NCM and b) Gr electrodes of NCM/Gr all-solid-state full-cells using thin SE layer (50–60 μm) before cycling and after 10 cycles at 0.2C.

Figure 55. Results for NCM/Gr and NCM/Si-C all-solid-state three-electrode cells discharged to 0 V. Transient charge-discharge voltage profiles for each electrode for a) NCM/Gr and b) NCM/Si-C cells during discharge to 0 V. Note the higher cutoff voltage for Si-C electrode in (b) than that for Gr electrode in (a) (indicated by ‘*’) during normal discharge. Also note the lower terminal voltage for NCM electrode in NCM/Gr cell (indicated by an arrow) in (a) than that for NCM electrode in NCM/Si-C cell in (b) upon discharge to 0 V.

Figure 56. Transient charge-discharge voltage profiles of each electrode for a) NCM/Gr and b) NCM/Si-C all-solid-state three-electrode cells during discharge to 0 V. Figure 55 is the enlarged view in x-axis.

Figure 57. Charge-discharge voltage profiles of a, c) NCM electrodes, b) Gr electrode, and d) Si-C electrode for NCM/Gr or NCM/Si-C all-solid-state three-electrode cells during discharge to 0 V.

Figure 58. Cycling performances of NCM/Gr and NCM/Si-C all-solid-state cells during discharge to 0 V. The corresponding charge-discharge voltage profiles are shown in Figures 55, 57, and 58.

Figure 59. First charge-discharge voltage profiles of the graphite half-cells with different weight fraction of LGPS.

Figure 60. First charge-discharge voltage profiles of the NCM/graphite full-cells with different weight fraction of LGPS in graphite electrode.

Figure 61. a) ex-situ XRD patterns of NCM and graphite electrodes at charge with different weight fraction of LGPS in graphite electrode at charged (dash line) and charge-discharged (solid line). b) Photographs of Gr electrodes with LGPS and LPSCl at charged.

Figure 62. First charge-discharge voltage profiles of the NCM/LTO full-cells and the corresponding pressure change curve.

Figure 63. a) Voltage profile of NCM/Gr full-cell and simulation of NCM and graphite electrode, respectively. b) Pressure change of NCM/Gr full-cell, Gr electrode, NCM/LTO, respectively.

Figure 64. a) Voltage profile of NCM/Gr full-cell with 0 wt% LGPS in graphite electrode and the corresponding differential capacity plot. b) Voltage profiles of NCM/Gr full-cells with 10, 20 wt% LGPS and the corresponding differential capacity plot. The points (a-e, e' and e'') are estimated from pressure change of NCM/Gr full-cell in a).

Figure 65. First and fifth voltage profiles of NCM/Gr full-cell with 0 wt% LGPS and the corresponding pressure change.

Figure 66. Cross-sectional FESEM images of Gr electrode with 0 wt% LGPS of a) before cycling and b) after 1 cycle.

Figure 67. Cross-sectional FESEM images of Gr electrode with 20 wt% LGPS of after 1 cycle.

Figure 68. First and fifth voltage profiles of NCM/Gr full-cell with 0 wt% LGPS and the corresponding pressure change.

List of Tables

Table 1. Major characteristics of the NW-SE films.

Table 2. Major characteristics of the LGPS-based SE films

Table 3. Characteristics of dry- and slurry-mixed NCM622 electrodes for ASLBs.

Table 4. Characteristics of NCM622/graphite all-solid-state full-cells

Table 5. Coulombic efficiency for NCM/Gr all-solid-state full-cells.

Table 6. SOC estimation of graphite electrode from the results of pressure change.

Nomenclature

LIBs	Lithium-ion batteries
LEs	Liquid electrolytes
EVs	Electronic vehicles
ESS	Energy storage system
SEs	Solid electrolytes
ASLBs	All-solid-state lithium batteries
PLD	Pulsed laser deposition
WEs	Working electrodes
CEs	Counter electrodes
REs	Reference electrodes
SEI	Solid electrolyte interfaces
MCI	Mixed conducting interphases
FESEM	Field-emission scanning electron microscopy
CP	Cross-section polisher
TGA	Thermal gravimetric analysis
HRTEM	High-resolution transmission electron microscopy
EDXS (EDS)	Energy-dispersive X-ray spectroscopy
FTIR	Fourier-transform infrared spectroscopy
TOF-SIMS	Time of flight secondary ion mass spectrometry
MAS-NMR	Magic angle spinning nuclear magnetic resonance spectroscopy

1. Introduction

Since the first commercialization of conventional lithium-ion batteries (LIBs) using organic liquid electrolytes (LEs) by Sony Corporation, they have been emerged as one of major energy storage sources due to its high energy density and power density.¹⁻⁶ The most important advantage of conventional LIBs is high energy density due to their high voltage of $> 4V$, which originates from the lowest negative electrochemical potential ($-3.040 V$ vs. the standard hydrogen electrode).¹⁻⁵ However, conventional LIBs using organic LEs encounter the safety concerns because of their flammability and possible leakages.¹⁻⁹ Moreover, as the state-of-art LIBs are required to meet the requirements of large-scale energy storage sources such as electronic vehicles (EVs) and energy storage system (ESS),³⁻⁴ their engineering efforts such as higher voltage cut-off and thinner the separators ($\leq 10 \mu m$) are accelerating the safety issues, which originated from gas evolution¹⁰⁻¹¹ and internal short-circuits (ISCs)¹²⁻¹³.

All-solid-state lithium or lithium-ion batteries (ASLBs) using inorganic solid electrolytes have attracted the interest due to the safety advantages and the potentials of high energy density, which is enabled by the use of Li metal as anode and bipolar stacked battery system.^{7-9 14-15} The opportunity of broad operating temperature ranges, which is originated from high thermal stability of SEs, offers also enormous merits from the viewpoint of large-scale energy storage applications.¹⁵ Furthermore, the intrinsic nature of inorganic SEs, compared to that of LEs, have several superior advantages of electrochemical behaviors. First, the mobile ion is only cation, which is Li-ion in its frameworks. Thus, as the lithium transfer number is 1, it is called the single ionic conductor.^{7-8, 14-15} Second, as it does not suffer from de-solvation behaviors at the interface between active materials and solid electrolytes, it has much less charge transfer resistance, compared to that of organic LEs.^{5, 16-18} Considering superior merits, if it is performed under the equal- environments such as same ionic conductivity, the batteries using SEs may show an outstanding performance.¹⁸

Thin-film ASLBs using LiPON ($Li_{3.3}PO_{3.9}B_{0.17}$), which is a well-known commercialized SE material, have been outperformed.¹⁹⁻²² But, as they were fabricated by vacuum deposition process, it is hard to make a thick electrode (tens of micrometers).¹⁹⁻²² Moreover, the low ionic conductivity at room temperature (RT) of LiPON is limited to small-scale energy storage sources.²¹⁻²² Thus, it is difficult to compete to conventional LIBs from viewpoint of manufacturing cost and energy density.²¹⁻²² In the other hands, bulk-type ASLBs have attracted the promising potentiality such as scalable fabrication, higher energy density by enabled thick and bipolar electrodes.^{7-8, 15} Because the microstructures of electrode in bulk-type ASLBs also are similar to conventional LIBs electrodes,⁷⁻⁸ if SEs are superionic conductor ($\sim 10^{-2} S cm^{-1}$), bulk-type ASLBs may be expected outstanding performance due to its intrinsic nature of SEs.¹⁵ However, there are several requirements such as scalable and cost-effective fabrication protocol, ionically and electronically well-designed electrode and most-importantly, highly conductive solid electrolyte, compared to ionic conductivity of LEs ($\sim 10^{-2} S cm^{-1}$), and others.^{7-8, 23-29}

To date, highly conductive SEs have been reported. Among them, Oxide and Sulfide inorganic SEs have been particularly investigated due to moderately ionic conductivity ($> 10^{-4}$ S cm $^{-1}$ at RT). The perovskite $\text{Li}_{3-x}\text{La}_{2/3-2x}\text{Ti}_{1/3-2x}\text{TiO}_3$ ($0 < x < 0.16$) (LLTO),³⁰ the NASICON-structured $\text{Li}_{1.3}\text{Al}_{0.3}\text{Ti}_{1.7}(\text{PO}_4)_3$ ³¹ and the garnet-structured $\text{Li}_7\text{La}_3\text{Zr}_2\text{O}_{12}$ (LLZO)³² are the well-known oxide SEs chemistry. Although their fabrications of bulk-type ASLBs using air-stable oxide SEs have also been investigated, sintering process at high temperature (~ 800 °C) is necessary to require the two-dimensional intimate contacts between active materials and SEs.³³⁻³⁴ Unfortunately, the undesired interfacial reaction by mutual diffusion of elements between LLZO and LiCoO_2 was inevitable, resulting in their extremely poor electrochemical performance.³³⁻³⁴ On the other hand, superior performances of bulk-type ASLBs have been reported using sulfide SEs such as glass-ceramic $\text{Li}_2\text{S-P}_2\text{S}_5$ (e.g., $\text{Li}_7\text{P}_3\text{S}_{11}$, 4.1×10^{-3} S cm $^{-1}$),³⁵ thio-LISICON ($\text{Li}_{3.25}\text{Ge}_{0.25}\text{P}_{0.75}\text{S}_4$, 2.5×10^{-3} S cm $^{-1}$),³⁶ argyrodite $\text{Li}_6\text{PS}_5\text{X}$ (X; Cl, Br, I, 3.2×10^{-3} S cm $^{-1}$),³⁷⁻³⁸ $\text{Li}_{10}\text{GeP}_2\text{S}_{12}$ (LGPS, 1.2×10^{-2} S cm $^{-1}$),¹⁴ and $\text{Li}_{9.5}\text{Si}_{1.74}\text{P}_{1.44}\text{S}_{11.7}\text{Cl}_{0.3}$ (LiSiPSCl, 2.5×10^{-2} S cm $^{-1}$).¹⁵ Although it generates toxic H_2S gas due to their instability in air,³⁹⁻⁴⁰ sulfide SEs are the most promising alternative candidate of inorganic SEs because of the following properties. First, it shows higher ionic conductivity ($\sim 10^{-2}$ S cm $^{-1}$), compared to that of LEs, than oxide SEs. As the development of superionic sulfide SEs are considered a breakthrough, the investigation of ASLBs using sulfide SEs have been accelerated. Second, sulfide SEs show moderate Young's moduli in between those of organic polymer electrolytes and oxide SEs.²⁴ Thus, as their deformability enables intimate contacts between active materials and SEs by simple cold-pressing,^{24, 26} the undesired interfacial reaction during fabrication of ASLBs using sulfide SEs may be avoided.

Most efforts for development of bulk-type ASLBs are focused on the ionic conductivity of SEs including design strategies^{8, 36, 41-43} and analysis of conduction mechanism using first principle computation techniques.⁴⁴⁻⁴⁸ Owing to systematic approaches, the superionic conductive sulfide SEs including LGPS¹⁴ and LiSiPSCl¹⁵ have been developed in the past few years. However, there is a discrepancy between high conductive sulfide SEs and poor electrochemical performance of ASLBs, which is originated from microstructure of electrode including the following properties. First, ASLB using inorganic SEs suffer from limited solid-solid ionic contacts due to inherent property. In practice, from the high porosity of composite electrode (~ 30 %), it indicates that poor ionic contacts between active materials and SEs.²³ To improve poor ionic contacts, the SE coating techniques such pulsed laser deposition (PLD),^{24, 49} single-step wet-chemical fabrication²⁵ and homogeneous SE solution^{26-27, 50-52} have been reported. Thus, improved SE coverages onto surface of active materials match well with their systematic and complementary analysis results.^{26-27, 52} Second, understanding and controlling the interfacial chemistries are important to develop the high performance ASLBs. From the theoretical and experimental studies on electrode-SE interfaces, the narrow electrochemical stability of SEs has been reported.⁵³⁻⁵⁴ Accordingly, it has been shown that the electrochemical performance of ASLBs is affected

by ionic conductivity as well as electrochemical stability and interface compatibility.⁵⁵ Therefore, stable passivating interfaces, which is only ionically conductive layer, should be formed between active materials and SEs for high performance of ASLBs.⁵³⁻⁵⁶ Third, surface modification of active materials should be provided as necessary. Although sulfide SEs may be formed oxidation layer with electronically insulating, the reactions of sulfide SEs and oxide cathodes are a fatal flaw due to their electronical conducting ability.^{53 54} Moreover, the interfacial reactions between sulfide SEs and oxide cathode are highly favorable, thereby deteriorating interfacial layer due to formation of transition metal sulfide^{53 54 57 58} and mutual diffusion of elements⁵⁸. Thus, to solve the incompatibility issue, the protective coating materials on oxide cathode have been reported.^{56, 59-63}

From the viewpoint of optimal method of processing, there are several requirements such as low cost, scalable fabrication, enough mechanical stability and excellent stability in dry air.⁷⁻⁸ In most studies, the pelletized electrodes, which consist of inorganic SEs, active materials and carbon additives, were too mechanical unstable to be scaled up.^{8, 25, 27, 29, 64-65} Thus, the addition of polymer is essential to enhance mechanical property and adhesion with current collectors, which allows fabrication of large-scale sheet-type electrode. Accordingly, sheet-type electrode and SE films using slurry process are considered as ideal solution.^{8, 29, 64-65}

Reliable electrochemical test protocols are a prerequisite in research and development for advanced LIBs. Most importantly, the in-depth study of all-solid-state full-cells, which is imperative for practical applications, really hasn't been reported very much.⁶⁶⁻⁶⁸ Unfortunately, as the technology level of ASLBs is still in its early stages, most studies have paid much attention to scalable fabrication and energy density (Wh/kg_{cell}),^{25, 27, 29, 64-65} which is far too low to compete with that of conventional LIBs. Although several studies of all-solid-state full-cells have been reported, they have paid much attention to not only electrochemical analysis in half-cells but fabrication of sheet-type all-solid-state full-cells.^{25, 27, 64-65} Thus, the development of reliable all-solid-state three-electrode cells is imperative. Furthermore, most electrochemical performances of ASLBs have been reported under high external pressure (tends of MPa).⁶⁶⁻⁶⁷ Even though the ionically and electronically well-designed electrode are fabricated, their conduction pathways might be deteriorated by volume changes of active materials and side reaction of SEs.⁶⁷ From the viewpoint of practical applications in terms of large-scale and moderate operation conditions (e.g., low external pressure), it has a strong influence on their electrochemical performance. In this regard, understanding and controlling of pressure changes at the interface should be also necessarily studied.

In this work, strategies for achieving high performance and the reliable electrochemical analysis of sheet-type ASLBs are demonstrated. The first part is for achieving high performance of sheet-type ASLBs using slurry process. The facile and scalable fabrication of sheet-type electrode and SE films are suggested by using polymeric binder and porous polymer membrane, respectively. And the

systematic and complementary analysis are discussed mainly on the aspect of their designed cell architecture. The second part is for reliable electrochemical analysis using a novel bulk-type all-solid-state three-electrode cell and pressure monitoring system. The three-electrode cells provide the electrochemical test protocol, thereby enabling diagnosis of failure modes for ASLBs. In particular, the earlier termination of CEs (Li-In alloy) than WEs (Sn) in all-solid-state half-cells is solved by percolating Li-In alloy with SEs. In addition, the failure mechanism of $\text{LiNi}_{0.6}\text{Co}_{0.2}\text{Mn}_{0.2}\text{O}_2/\text{graphite}$ full-cells having only 50-60 μm -thick SE layers at high C-rates is also revealed. Further, a unique dischargeability to 0 V for $\text{LiNi}_{0.6}\text{Co}_{0.2}\text{Mn}_{0.2}\text{O}_2/\text{graphite}$ or $\text{LiNi}_{0.6}\text{Co}_{0.2}\text{Mn}_{0.2}\text{O}_2/\text{Si-C}$ full-cells is described. Lastly, the interfacial behaviors at the graphite electrode in $\text{LiNi}_{0.6}\text{Co}_{0.2}\text{Mn}_{0.2}\text{O}_2/\text{graphite}$ full-cells with various amounts of LGPS in graphite electrode were investigated. Moreover, the state-of-charge (SOC) values, which is the most important factor of tracking the abnormal behavior in lithium rechargeable batteries, were successfully estimated from volume changes of graphite electrode in $\text{LiNi}_{0.6}\text{Co}_{0.2}\text{Mn}_{0.2}\text{O}_2/\text{graphite}$ full-cells. As the rearrangement of particles in electrode during cycling was also observed, it will be possible to imperative issues in the practical all-solid-state technology.

2. Background

2.1. Principle of Lithium Secondary Batteries

Since the first commercialization of rechargeable LIBs, the major active materials of LiCoO_2 and graphite are used as cathode and as anode, respectively.¹⁻⁴ The working principle of LIBs are illustrated in Figure 1. The basic elements of LIBs are cathode (positive electrode), anode (negative electrode), separator and liquid electrolyte, which consist of Li salts dissolved in aprotic solvent. In charge process, when an external electrical energy is provided into LIB cells, which is nonspontaneous reaction, the Li-ions are moved from cathode materials to anode materials through electrolytes. And then, reduction reaction occurs at anode materials. In discharge process, which is spontaneous reaction where energy is released to supply power, the movements of Li-ions change reverse.

As the role of electrolyte is an ionic conductor and electronic insulator, the basic electrolyte should meet requirements:⁵ (1) To be good ionic conductor and electronic insulator. (2) To have wide electrochemical window. (3) To remain inert to all cell components, especially the charged surfaces of active materials. (4) To remain liquid in a wide temperature range. (5) To be safe (low flammability), nontoxic and economical. However, as conventional liquid electrolytes (LEs) are decomposed at the surface of active materials, it has a great effect on the performance of LIBs.²⁻⁵ Moreover, the dissolution of transition metal from oxide cathode materials ($\text{LiNi}_x\text{Co}_y\text{Mn}_z\text{O}_2$) and polysulfide for sulfur-carbon cathodes are a main factor of the degradation of conventional LIBs.²⁻⁵ Fortunately, as the electronically insulating solid electrolyte interface (SEI) layer is formed, graphite has been successfully employed in LIBs. Furthermore, for improvement of safety, the characteristics of separator should be also considered the following requirements:⁶ (1) To be electronic insulator. (2) To be sufficient physical strength to allow easy handling. (3) To have high thermal stability (low shrinkage). (4) To have chemical resistance with liquid electrolyte and electrode reactants. (5) To be readily wetted by electrolyte. (6) To be uniformly and thinner thickness. Unfortunately, as the conventional LEs has narrow operating temperature range and its flammability, the state-of-art LIBs are struggling to solve the safety problem until now.^{2, 5, 12, 69}

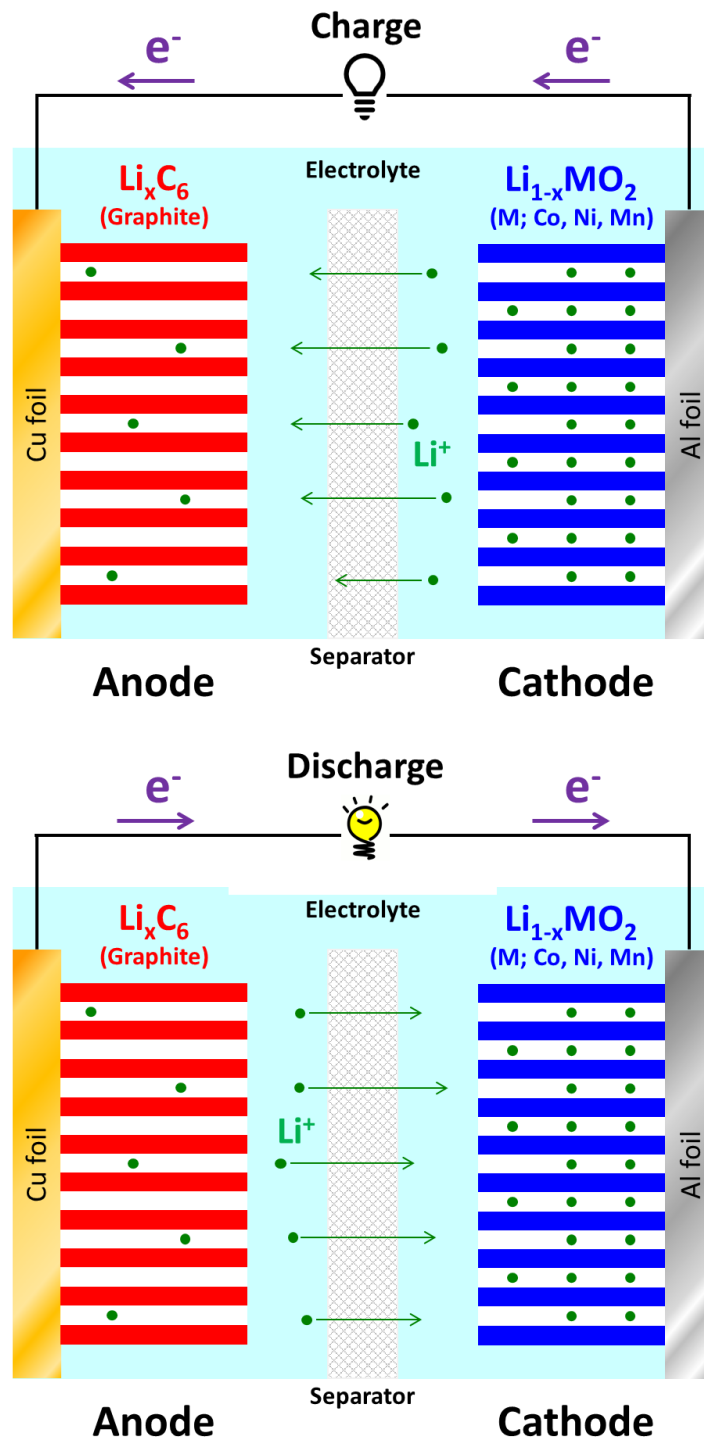


Figure 1. Schematic diagram of the working principle of lithium ion battery.

2.2. Overview of Bulk-Type Inorganic All-Solid-State Lithium Batteries

2.2.1. Conductivity of Solid Electrolytes

As the one of merits of sulfide solid electrolytes (SEs) is single ionic conductor, the strategies of well-designed immobile crystal structure framework, which provides good Li-ion conduction pathways, are imperative for achieving high ionic conductivity. For superionic conductive SEs, their crystal structure framework has distinguishing features: 1) the favorable hopping sites for mobile. 2) the long-range of connectivity between favorable hopping sites with low energy barrier. 3) the chemistries of materials (e.g.; the highly polarizable and larger anions). Thus, the overall conductivity is expressed by the following equation. ^{8, 70-71}

$$\sigma = \frac{A}{T} n_c \exp\left(-\frac{E_a}{k_B T}\right)$$

where, A is constant related to the crystal structure, n_c is the concentration of mobile-ion carriers (e.g., vacancy or interstitial), E_a is the activation energy for ion transport, T is temperature in K, and k_B is the Boltzmann constant.

Generally, as the isovalent substitution of larger and more polarizable ions tends to increase the ionic conductivity of SEs, sulfide SEs show higher conductivity than oxide SEs. ^{36, 45} Among the sulfide glass electrolytes, the famous binary system is $\text{Li}_2\text{S}-\text{P}_2\text{S}_5$ such as $\text{Li}_7\text{P}_3\text{S}_{11}$ (70 Li_2S -30 P_2S_5 , which has an equimolar mixture of isolated PS_4^{3-} and $\text{P}_2\text{S}_7^{4-}$) and Li_3PS_4 (75 Li_2S -25 P_2S_5 , which is comprised of isolated PS_4^{3-}). Although these materials exhibit a wide range of compositions and high conductivities, the crystal structure of metastable $\text{Li}_2\text{S}-\text{P}_2\text{S}_5$ glass-ceramics are highly complicated. ⁷²⁻⁷⁴ For example, the ionic conductivities of Li_3PS_4 are significantly different depending on the structure (e.g.; $\gamma\text{-Li}_3\text{PS}_4$: $3 \times 10^{-7} \text{ S cm}^{-1}$ vs. $\beta\text{-Li}_3\text{PS}_4$: $\sim 10^{-4}\text{-}10^{-3} \text{ S cm}^{-1}$). ⁷³ Especially, the structure of $\text{Li}_4\text{P}_2\text{S}_6$, which is crystallized from the sulfur loss of $\text{Li}_4\text{P}_2\text{S}_7$, shows low conductivity due to large defect formation enthalpy and the relatively high migration barrier. ⁷⁵ In contrast, for crystalline sulfide SEs, Kanno and co-workers reported the well-known thio-lithium superionic conductor (thio-LISICON, $\text{Li}_{3.25}\text{Ge}_{0.25}\text{P}_{0.75}\text{S}_4$, $2.2 \times 10^{-3} \text{ S cm}^{-1}$ at 25°C), ³⁶ which was the first crystalline ionic conductor along the $\text{Li}_3\text{PS}_4\text{-Li}_4\text{MS}_4$ tie line. And then, they also reported the extremely high conductive $\text{Li}_{10}\text{GeP}_2\text{S}_{12}$ (LGPS, $1.2 \times 10^{-2} \text{ S cm}^{-1}$ at RT) ¹⁴ and $\text{Li}_{9.5}\text{Si}_{1.74}\text{P}_{1.44}\text{S}_{11.7}\text{Cl}_{0.3}$ (LiSiPSCl , $2.5 \times 10^{-2} \text{ S cm}^{-1}$), ¹⁵ which is compared to conductivity of LEs. Ceder and co-workers claimed that LGPS is in fact a 3D ion conductor from the results of ab initio MD simulation, which is well-matched with the experimental value (the calculated overall conductivity of $9 \times 10^{-3} \text{ S cm}^{-1}$). ⁴⁴ Also, the superionic conductive of LGPS was originated from the fast in the 1D diffusion channel along the c direction from the calculated values of conductivities and activation barriers ($4 \times 10^{-2} \text{ S cm}^{-1}$ and 0.17 eV in the c-direction vs. $9 \times 10^{-4} \text{ S cm}^{-1}$ and 0.28 eV in the ab plane, respectively). ⁴⁴ In addition, they reported that the interstitial Li-ion defects is key to

develop the high conductive SEs by ab initio MD simulation.⁷⁶ Recently, the off-stoichiometric LGPS-like-structured $\text{Li}_{9.6}\text{P}_3\text{S}_{12}$ also reported ($1.2 \times 10^{-3} \text{ S cm}^{-1}$ at 25°C).¹⁵ Furthermore, the argyrodite $\text{Li}_6\text{PS}_5\text{X}$ (X; Cl, Br, I), which is comprised of isolated PS_4^{3-} and Li-coordinated S^{2-} , also shows exhibits high ionic conductivity ($> 10^{-3} \text{ S cm}^{-1}$).^{37-38, 77-78} As the substitution of X in $\text{Li}_6\text{PS}_5\text{X}$ provides the polarizability and lattice parameter of the anion sublattice without significantly changing Li-ion conduction pathways, it affects the Li occupancies and X/ S^{2-} site disorders.⁷⁷⁻⁷⁸ For the case of I anion (2.20 pm), as it is known to be existed at the different crystallographic sites of S^{2-} anion, no site disorder occurs due to larger size than S^{2-} anion (1.84 pm).⁷⁷⁻⁷⁸ However, very recently, Wolfgang and co-workers reported that the aliovalent substitution in $\text{Li}_{6+x}\text{P}_{1-x}\text{Ge}_x\text{S}_5\text{I}$ shows high ionic conductivity ($5.4 \times 10^{-3} \text{ S cm}^{-1}$ in cold-pressed state and $1.84 \times 10^{-2} \text{ S cm}^{-1}$ upon sintering) with changing significantly the Li^+ occupancies, I/ S^{2-} site disorder and activation barrier.⁷⁸ These results suggest that the structural changes and increasing lattice volume with proper combinations of anions provide an insight into the exploration of highly conductive chemistries of SEs.

2.2.2. Electrochemical Stability of Solid Electrolytes

The success of conventional LIBs must have been very difficult to develop the high performance of LIBs without the presence and development of solid electrolyte layer (SEI) layer, which is mainly originated from decomposition of organic LEs.²⁻⁵ Thus, the electrochemical stability and chemistry of LEs are considered as the one of major factors for high performance such as durability, rate capability and safety.

In this regard, the electrochemical stability of sulfide SEs is also important to develop the high performance of ASLBs. Unfortunately, as the understanding of decomposition of sulfide SEs at the interface is in a stage of infancy, they have limited electrochemical windows from the theoretical calculation.^{44-45, 54} Ceder and co-workers investigated the phase stability, electrochemical stability and Li-ion conductivity of the highly conductive $\text{Li}_{10\pm 1}\text{MP}_2\text{X}_{12}$ (where M=Ge, Si, Sn, Al, or P and X=O, S or Se) family using first principle calculations.⁴⁵ They claimed that the metastable LGPS is not stable against reduction at low potential because of their low band gap (3.6 eV) and suffer from a passivation phenomenon, where Li_2X , Li_3P and Li_xM_y alloy are generally formed as decomposition products.⁴⁵ In particular, the detrimental mixed conducting interphases (MCIs), which is originated from Li_xM_y alloy, may lead to continuous irreversible reaction. At the positive potential, the cathodic phase equilibria of sulfide SEs comprise $\text{M}_x\text{P}_y\text{S}_z$, P_2S_5 and S.⁴⁵ Thereafter, the formation of Li_2S by decomposition of LGPS at the low potential ($< 0.6 \text{ V vs. Li/Li}^+$) was observed by Jung and co-workers, thereby degrading the performance of ASLBs.⁵⁵ Moreover, their results provide an insight on the strategy for improvement of electrochemical stability of sulfide SEs, which is the isovalent substitution of oxygen for $\text{Li}_{10\pm 1}\text{MP}_2\text{S}_{12}$, based on the energy levels of valence p-orbitals of anionic species.⁴⁵ With this

background, the oxygen substitution of sulfide SEs tends to improve the electrochemical stability.⁷⁹⁻⁸²

Although the narrow electrochemical window of sulfide SEs can degrade the performance of ASLBs, it provides new insight into the design of interfacial engineering and the understanding of passivation phenomenon.

2.2.3. Interface Compatibility between Active Materials and Solid Electrolytes

Most inorganic SEs suffer from incompatibility with electrode materials and narrow intrinsic electrochemical windows, which results in the below par electrochemical performances. Thus, the understanding of phenomena at the interface between active materials and SEs is one of crucial factors for achieving high performance of ASLBs.

As the performance of ASLBs using Li_xMO_2 ($\text{M}=\text{Co}, \text{Ni}, \text{Mn}$) have been reported, the bare Li_xMO_2 exhibits much lower capacity and higher overpotential than the case of conventional LIB.^{28, 34, 49, 58-59, 61, 64, 82} This can be explained by the intrinsically low oxidation onset potential (~ 3 V vs. Li/Li^+) of sulfide SEs,^{44-45, 55, 83-86} mutually diffusion of elements (M, P, and S) at the interface and surface impurities,^{57-58, 79, 85} which lead to huge irreversible reaction during charging. Moreover, the high overpotential during cycling is also caused by the poor ionic contacts between active materials and SEs.^{23-27, 50-51, 87-88} In this regard, numerous coating materials for interfacial engineering on active materials have been reported such as LiNbO_3 ,⁵⁹ $\text{Li}_4\text{Ti}_5\text{O}_{12}$,⁶⁰ LiAlO_2 ,⁶¹ Al_2O_3 ,⁶² Li_3PO_4 ,⁶³ $\text{Li}_2\text{O}-\text{ZrO}_2$,⁶⁴ Li_3BO_3 ,⁵⁶ and $\text{Li}_{3-x}\text{B}_{1-x}\text{C}_x\text{O}_3$.⁵⁶ Importantly, Jung and co-workers reported that the interfacial reaction between LiCoO_2 and sulfide SEs is not thermodynamically stable but spontaneous decomposition by calculating the thermodynamic reaction energies.⁵⁶ Thus, the surface modification for prevention of continuous reaction by detrimental MCIs containing transition metal sulfide is important to develop the high performance ASLBs.⁵⁶

Lithium metal has been considered as ideal anode for lithium secondary batteries because of its high theoretical capacity (3862 mA h g^{-1}) and the lowest negative electrochemical potential. However, for conventional LIBs, there are tough safety matters relevant to the internal short-circuits (ISCs) caused by dendritic growth of Li metal during cycling, thereby restricting the application of practical LIBs.⁸⁹⁻⁹⁶ Unfortunately, all-solid-state Li metal batteries also suffer from internal short-circuits (ISCs)⁹⁷⁻⁹⁹ and deteriorating chemical reaction of SEs with Li metal.¹⁰⁰⁻¹⁰⁵ The penetrating growth of Li metal into the defects of SE structures, that is voids and along the grain boundaries have been reported.⁹⁷⁻⁹⁹ In this regard, the protective layer for suppressing dendritic growth of Li metal and reaction with sulfide SEs are essential for practical all-solid-state Li metal batteries.¹⁰²⁻¹⁰⁷

2.2.4. Reliable Electrochemical Test Protocols for All-Solid-State Lithium Batteries

Reliable electrochemical test protocols are prerequisite in R&D for advanced lithium rechargeable

batteries. For conventional lithium-ion batteries (LIBs) using liquid electrolytes (LEs), as many electrochemical and spectroscopic investigations have been reported,¹⁰⁸⁻¹¹³ the conventional LIBs have been employed successfully in various applications based on the in-depth study. Unfortunately, however, the unique fabrication protocol of all-solid-state lithium batteries (ASLBs), which is based on cold-pressing under high pressure (hundreds of MPa) and the use of a pelletizing mold (Figure 2), makes the design of reliable electrochemical test protocols for bulk-type ASLBs extremely challenging. Furthermore, from the viewpoint of practical applications, as the thick SE layer ($\geq 600 \mu\text{m}$) have been routinely used for the lab-scale tests of ASLBs, the thickness of SE layer should be reduced to tens of micrometers. For these reasons, only a few studies of electrochemical test protocols for bulk-type ASLBs have been reported.⁶⁶⁻⁶⁸

As Li metal has constant voltage even at high current densities, it is routinely used as a reference electrode (RE) and simultaneously as a counter electrode (CE) for conventional LIBs. However, interpretation of the performances of working electrodes (WEs) is hindered by Li metal electrodes in harsh conditions.⁹⁴⁻⁹⁶ In contrast, Li-In alloy has been used as counter electrode and reference electrode in the half-cells of ASLBs because of their flat voltage plateau at 0.62 V (vs. Li/Li⁺) as matters stand.^{14, 23, 25-28, 38, 49-52, 55-56, 58-60, 65-68, 80, 83, 85-86, 107, 114} But, as their kinetic behaviors under various electrochemical conditions have not been evaluated yet, the reliability of Li-In alloy as counter and reference electrodes in ASLBs must be carefully evaluated. In particular, when the advanced electrode materials (e.g., Sn,¹¹⁵⁻¹¹⁶ Si¹¹⁷⁻¹²¹ and S¹²²), which is under the high usage and current densities of Li-In alloy, it might show that the electrochemical performance of WEs is hindered by polarization of Li-In alloy. Furthermore, as all-solid-state lithium batteries (ASLBs) have been operated under high external pressure, volume changes of active materials and/or decomposition of sulfide SEs is not critical for deteriorating interfacial layer in terms of their ionically and electronically conduction pathways during cycling so far.⁶⁶⁻⁶⁷ From a practical perspective, as the operation conditions of large-scale ASLBs should be milder than the present, the tracking of volume changes at the interface between active materials and sulfide SEs is an essential prerequisite.

In this regard, the understanding and controlling the interfacial reactions such as decomposition of SE with Li metal or oxide cathode materials and volume changes of active materials must be required for the development of high performance of ASLBs.

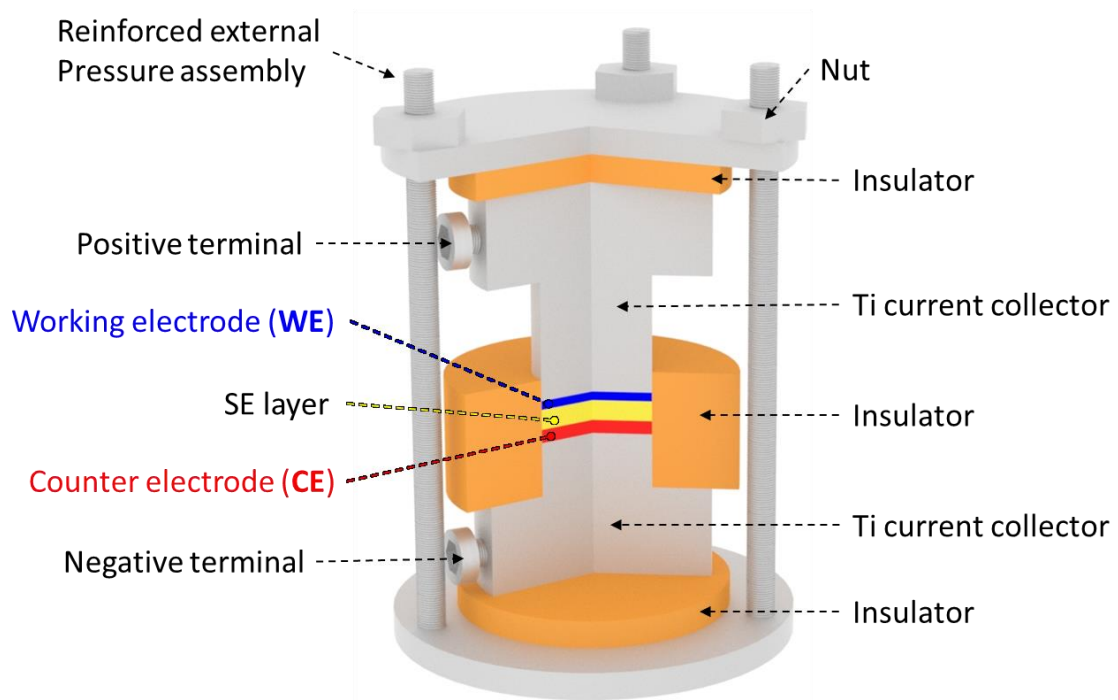


Figure 2. Schematic diagram of a typical bulk-type all-solid-state cell.

3. Experimental

3.1 Preparation of materials

For synthesis of sulfide SEs. LPS (or 75Li₂S-25P₂S₅ glass-ceramic SE) powders were prepared by mechanically milling a mixture of Li₂S (99.9%, Alfa Aesar) and P₂S₅ (99%, Sigma-Aldrich), followed by heat-treatment at 243 °C for 1 h.⁵⁵ For the preparation of LGPS powders, stoichiometric mixture of Li₂S, P₂S₅, and GeS₂ (99.9%, American Elements) powders were pelletized under 370 MPa and subjected to heat treatment at 550 °C for 10 h.⁵⁵ Argyrodite Li₆PS₅Cl SE powders were prepared by mechanical-milling and subsequent heat-treatment under inert atmosphere. After a stoichiometric mixture of Li₂S (99.9%, Alfa Aesar), P₂S₅ (99%, Sigma-Aldrich), and LiCl (99.99%, Sigma Aldrich) was ball-milled at 600 rpm for 10 h at room temperature in a ZrO₂ vial with ZrO₂ balls using a planetary ball mill (Pulverisette 7PL; Fritsch GmbH).²⁷ The resulting powders were heat-treated at 550 °C for 5 h in a sealed quartz tube. The as-prepared SE powders of LPS, LGPS and LPSCl showed a Li-ion conductivity of 1.0×10^{-3} S cm⁻¹, 6.0×10^{-3} S cm⁻¹, 3.0×10^{-3} S cm⁻¹ at 30 °C, respectively.

For the sheet-type solid electrolyte films (NW-SE films). Anhydrous toluene (99.8%, Sigma-Aldrich) was used, after removal of a trace amount of water by using CaH₂, as a solvent to disperse the SE powders for the doctor-blade method. Prior to using, the PPTA non-woven (thickness: ~16 μm, porosity: ~70%, Kuraray) was dried overnight under vacuum. In addition, Ni-coated NW, as a current collector, was obtained by depositing Ni on NW using a DC sputtering system (Sorona, SRN-120) at 700 W for 25 min at 10 mTorr under Ar. The pNW was prepared by dipping NW in a solution of LiTFSI (99.95%, Sigma-Aldrich) and PEO (average Mw ~5,000,000, Sigma-Aldrich) dissolved in anhydrous acetonitrile (99.8%, Sigma-Aldrich) (LiTFSI:PEO = 1:8 mole ratio), and subsequently drying in an Ar-filled dry box. LTS powders were prepared by mechanical milling.¹²³ 33.8 mg of Li₃N (99.4%, Alfa Aesar) and 216.4 mg of TiS₂ (99.9%, Sigma-Aldrich) powders were mechanically milled at 500 rpm for 2 h using a planetary ball mill (Pulverisette 7PL; Fritsch GmbH) containing a steel vial and ZrO₂ balls.

For the sheet-type electrodes and diagnostic study of ASLBs. The premixing process was carried out by milling a mixture of NCM622 and SE powders with ZrO₂ balls at 1000 rpm for 6 min using Thinky Mixer. LiNbO₃ (1.4 wt%) was coated on NCM622 powder using the wet-chemical method, before using the electrodes.^{26, 59}

3.2 Materials characterization

For the sheet-type solid electrolyte films (NW-SE films). FESEM images were obtained using an S-4800 (Hitachi). The cross-sectioned mono-cell (LCO/(SE-NW-SE)/LTO) was prepared by coating glue on both sides of the sample in order to maintain its form and to avoid exposure to H₂O in air. After polishing the cross-sectioned surface at 5 kV for 13 h with an Ar ion beam (JEOL, SM-0910),

FESEM images of the cross-section were obtained using a Quanta 3D FEG (FEI, SE mode); the sample was prepared entirely in a dry room. The amount of residual Li_2CO_3 in the LiCoO_2 powders was measured by Warder's titration method¹²⁴ using an Auto Titrator. The TGA data were obtained from 25 °C to 900 °C at 5 °C min^{-1} under Ar with a SDT Q600 (TA Instrument). For the HRTEM and EDS analyses of the *p*NW film, a 30 keV Ga^+ ion beam was used for sectioning. The HRTEM images and EDS line scanning were obtained using JEM-2100F (JEOL) with 200 kV and 0.105 mA. Porosity values of the cold-pressed pellets were obtained by the following Equation.

$$\text{Porosity [\%]} = 100 - 100 \frac{\left(\frac{M}{\rho}\right)}{\left[\left(\frac{\pi}{4}\right) \cdot D^2 \cdot t\right]}$$

where M : weight of the pellet ($M = 0.15$ g), D : diameter of the pellet ($D = 1.3$ cm), t : thickness of the pellet ($t_{\text{LPS}} = 0.070$ cm, $t_{\text{LGPS}} = 0.067$ cm), ρ : apparent density ($\rho_{\text{LPS}} = 1.87$ g cm^{-3} , $\rho_{\text{LGPS}} = 2.035$ g cm^{-3})^{24, 125}

For the sheet-type electrodes. The FESEM images were obtained using an S-4800 (Hitachi). Cross-sectional surfaces of the electrodes were prepared by polishing at 5 kV for 13 h with an Ar ion beam (JEOL, SM-0910). The FESEM images and the corresponding EDXS elemental maps of cross-sectioned electrodes were obtained using a JSM-7000F (JEOL). For the XRD measurements, samples were sealed with a beryllium window and mounted on a D8-Bruker Advance diffractometer (Cu K_α radiation: 1.54056 Å) at 40 mA and 40 kV. The Raman and Fourier-transform infrared (FTIR) spectra were measured with a 532 nm ND-YAG laser using an Alpha300S (Witec Instruments) and in a wide range of frequencies from 800 to 4000 cm^{-1} using a Cary 670 (Agilent).

For the diagnostic study of ASLBs. For the results of diagnosis of failure mode of ASLBs using three-electrode cells, the cross-sectional surfaces of the samples were prepared by polishing at 1.5 kV for 4 h with an Ar ion beam (HITACHI, IM4000). The FESEM images and the corresponding EDXS elemental maps were obtained using an S-4800 (HITACHI). TOF-SIMS analyses were conducted on a TOF SIMS 5 (ION-TOF GmbH, Heisenbergstraße, Münster). A 25-keV pulsed Bi^+ ion source was employed for analysis and sputtering. The TOF-SIMS imaging areas were $300 \times 300 \mu\text{m}^2$ and $450 \times 450 \mu\text{m}^2$ for the cross-sectioned Li-In and Li-In-SE CEs, respectively. The base pressure of the analysis chamber was maintained at $<5.0 \times 10^{-10}$ Pa during all analyses. The ^7Li MAS-NMR spectra were obtained at 233.12 MHz at a rotor frequency of 25 kHz with 1.2 μs of 90° pulses using an Agilent VNMRS 600 MHz Solid NMR spectrometer with 1.6 mm HXY Fast MAS probe. Chemical shift for ^7Li is referenced to LiCl powder. For the ex-situ ^7Li MAS-NMR measurements, after the Gr electrodes for Gr/Li-In all-solid-state half-cells were lithiated at 0.1C for 8 h or at 2C for 20 min, the Gr electrodes and the SE layers, which were in contact with the Gr electrodes, were carefully collected and subjected to the measurements without exposure to air.

3.3 Electrochemical characterization

For the sheet-type solid electrolyte films (NW-SE films). Li⁺ ion conductivity of the SEs was measured by an alternating current (AC) method using a Li⁺-ion blocking cell (Ti/SE/Ti) at 30 °C. The LCO/LTO all-solid-state cell was fabricated from a 15 mg of a mixture of LCO and LGPS with 70:30 weight ratio and 24 mg of a mixture of LTO, LPS, and super P with 49.8:49.8:0.5 weight ratio were used as positive and negative composite electrodes, respectively. Furthermore, the LTS/LTO all-solid-state cell was fabricated from 4.5 mg of a mixture of LTS, LPS, and super P with 32.3:64.5:3.2 weight ratio and 10 mg of a mixture of LTO, LPS, and super P with 33.1:66.1:0.8 weight ratio were used as composite electrodes. For fabrication of the all-solid-state cell using the bendable NW-SE film, electrode powders of a composite were spread on the top of the NW-SE film and the cell was pelletized by pressing at 370 MPa. Electrode powders of another electrode were then spread on the other side of the NW-SE film, and then pressed at 370 MPa. All the powders were pressed in a polyaryletheretherketone (PEEK) mold (diameter = 13 mm) with Ti metal rods as current collectors (Figure 2). To fabricate free-standing LCO/LTO all-solid-state sheet cells, the composite electrodes were prepared by cold-pressing the electrode-coated Ni foil with the Ni-coated NW at 370 MPa. The as-prepared composite electrode on Ni-coated NW were then cut and assembled with the bendable SE film by pressing at 370 MPa. All the processes for preparing the SEs and fabricating the all-solid-state cells were performed in an Ar-filled dry box. The electrochemical impedance spectroscopy (EIS) study was performed using an Iviumstat (IVIUM Technologies Corp.).

For the sheet-type electrodes. The Li-ion conductivity of the Li₆PS₅Cl SE pelletized under 370 MPa was measured using an AC (alternating current) impedance method with a Ti/SE/Ti Li-ion blocking cell. The dry-mixed electrodes were obtained by manual mixing of active materials (NCM622), SE powders (LPSCl), and carbon additives (Super C65) with the target compositions. The wet-slurry fabricated electrodes were obtained by the following procedure. Slurries were prepared by mixing targeted amounts of SE powders, active materials (NCM622 or graphite powders), nitrile butadiene rubber (NBR), and carbon additives (only for cathode) in anhydrous xylene. After the as-prepared slurries were coated on current collectors using the doctor blade method, the electrodes were obtained by heating at 120 °C and subsequent drying under vacuum overnight. For fabrication of the NCM622/Li-In half-cells, the mixed electrode powders for dry-mixed electrodes (or the slurry mixed electrodes) were put on the surfaces of the pre-pelletized SE layer (150 mg). For fabrication of the NCM622/graphite full-cells, the SE layers were coated directly on the as-formed graphite electrode by the doctor-blade method using a xylene-NBR-based slurry. The negative electrodes of Li_{0.5}In (nominal composition) powders for the half-cells or the slurry-mixed graphite electrodes for the full-cells were put on the other side of the SE layer. Then, all the assembled components were pressed at 370 MPa in a PEEK (polyether ether ketone) mold (diameter of 13 mm) with Ti metal rods as current collectors

(Figure 2). The pelletized NCM622/graphite full-cells were cycled at 0.025C and 30 °C between 2.50–4.20 V for the first two cycles, 2.50–4.25 V for the subsequent two cycles, and 2.50–4.30 V for the following cycles. The pouch-type NCM622/graphite full-cells were fabricated by sealing an assembly of the wet-slurry fabricated electrodes and SE layer (positive electrodes: 80 × 60 mm², negative electrodes and SE layers: 83 × 63 mm²) in a pouch, and then pressing subsequently at 492 MPa. The pouch-type full-cells were cycled at 0.025C and 25 °C between 2.5–4.2 V. All the procedures for fabrication of the electrodes and cells were performed in an Ar-filled dry box in which H₂O was controlled to < 1 ppm. The EIS measurements were performed with amplitude of 10 mV and frequency range from 5 mHz to 1.5 MHz using an Iviumstat (IVIUM Technologies Corp.). After the cells were discharged to 3.7 V (vs. Li/Li⁺) at 0.1C at the second cycle, a constant voltage of 3.7 V (vs. Li/Li⁺) was applied until the current decreased to 0.025C, followed by rest for 3 h to restore equilibrium. The GITT measurements were carried out with a pulse current of 0.6C for 60 s and rest for 2 h at the second cycle. The contact areas between NCM622 and SE particles (*S*) were obtained by the GITT measurements using the following equation.^{26-27, 52}

$$D = \frac{4}{\pi\tau} \left(\frac{m_{\text{NCM}} \cdot V_{\text{M}}}{M_{\text{NCM}} \cdot S} \right)^2 \cdot \left(\frac{\Delta E_{\text{S}}}{\Delta E_{\text{t}}} \right)^2$$

where *D*: chemical diffusion coefficient of NCM622, *S*: contact area between electrolyte and active materials, τ : pulse duration (60 s), ΔE_{S} : steady-state voltage change, ΔE_{t} : transient voltage change, M_{NCM} : molecular weight of the host, Ni_{0.6}Co_{0.2}Mn_{0.2}O₂ (90.13 g mol⁻¹), m_{NCM} : mass of the host in the sample (varied depending on the mass loading), V_{m} : molar volume of the sample (the value used was for LiNi_{1/3}Co_{1/3}Mn_{1/3}O₂, 20.29 cm³ mol⁻¹).¹²⁶

The chemical diffusion coefficient (*D*) of 1.72 × 10⁻¹¹ cm² s⁻¹ for NCM622 was obtained from a GITT result using a NCM622/Li cell with LE. The surface coverage values were obtained by dividing the contact area between active materials and SEs obtained by the as-described GITT analysis by the surface areas of NCM622 powders obtained by N₂ adsorption-desorption isotherm experiment (0.64 m² g⁻¹).

For the diagnostic study of ASLBs using three-electrode cells. The Sn electrodes for all-solid-state half-cells were obtained by manual mixing of Sn (99%, 10 μm, Sigma-Aldrich) and SE powders (Li₆PS₅Cl) with the weight ratio of 70:30. The wet-slurry-fabricated electrodes were obtained by the following procedure. Slurries were prepared by mixing active materials (NCM or Gr or Si-C powders), SE powders, nitrile-butadiene rubber (NBR), and carbon additives (only for positive electrodes) in anhydrous xylene with the weight ratios of 68.1:29.2:1.4:1.3, 58.6:39.1:2.3:0.0, and 59.4:39.6:1.0:0.0 for the NCM, Gr, and Si-C electrodes, respectively. After the as-prepared slurries were coated on current collectors (Al and Ni foil for the NCM and Gr (or Si-C) electrodes, respectively) using the doctor blade method, the electrodes were obtained by heating at 120 °C and subsequent drying overnight under vacuum. The CEs for the half-cells were fabricated by mixing Li metal (FMC Lithium

Corp.) and In powders (99%, Sigma-Aldrich) with or without SE powders with the targeted weight ratios using Thinky mixer at 2000 rpm for 1 min. The amount of $\text{Li}_{0.5}\text{In}$ or $\text{Li}_{0.5}\text{In-SE}$ CEs was controlled so that the CEs accommodate more than two times higher full capacity for WEs by full lithiation of $\text{Li}_{0.5}\text{In}$ to LiIn . For example, the amount of Li-In(-SE) CEs for Sn electrode was set to accommodate a capacity of $959 \text{ mA h g}_{\text{Sn}}^{-1}$ for WEs. For the fabrication of the Sn/ Li-In(-SE) half-cells, the mixed Sn WE and Li-In(-SE) CE powders were spread on the other surfaces of the pre-pelletized SE ($\text{Li}_6\text{PS}_5\text{Cl}$) layer (150 mg). The Sn electrode for liquid-electrolyte-cells was prepared by spreading the Sn powders, super P, and poly(acrylic acid) (PAA) binder on a piece of Cu foil in a weight ratio of 70:10:20. The mass of Sn electrode was $4.7 \text{ mg}_{\text{electrode}} \text{ cm}^{-2}$ ($3.3 \text{ mg}_{\text{Sn}} \text{ cm}^{-2}$). For the liquid-electrolyte-cell tests, 2032-type coin cells using Li metal as the counter and reference electrode were used. A solution of LiPF_6 (1.0 M) dissolved in a mixture of ethylene carbonate (EC), ethyl methyl carbonate (EMC), and dimethyl carbonate (DMC) (3:4:3 v/v) (Panax Etec) was used as the electrolyte. A porous polypropylene (PP)/polyethylene (PE)/PP tri-layer film (Celgard Inc.) was used as the separator. For the NCM/Li all-solid-state cells, the wet-slurry fabricated NCM electrodes, $120 \mu\text{m}$ Li metal foils (HONJO METAL), and the $\text{Li}_6\text{PS}_5\text{Cl}$ pellet as the SE layer were used. For fabrication of the NCM/Gr (or NCM/Si-C) full-cells with the thick SE layers, the slurry-prepared electrodes were assembled with pre-pelletized SE layers. For fabrication of the NCM/Gr full-cells with the thin SE layers ($50\text{--}60 \mu\text{m}$), the SE layers were coated directly on the as-formed Gr electrode by the doctor-blade method using a xylene-NBR-based slurry. The np ratios (the areal capacity ratio of negative to positive electrodes) for NCM/Gr and NCM/Si-C full cells were approx. 1.1. For fabrication of three-electrode cells (Figure 3), after the WE/SE/CE assembly for the half-cells or full-cells were pressed at 370 MPa, additional SE layers (120 mg of $\text{Li}_6\text{PS}_5\text{Cl}$) were put on top of the WEs (Figure 3b). Finally, the $\text{Li}_{0.5}\text{In}$ powders or Li metal foils as RE were put on the top of the SE layer, forming RE/SE/WE/SE/CE, followed by pressing at 74 MPa or 15 MPa, respectively. For the NCM/Gr (or NCM/Si-C) three-electrode cells, a small piece of Al current collectors was carefully removed in order to connect the RE and WE layers through the SE layer as illustrated in Figure 3b. For the ex-situ ^7Li MAS-NMR measurements, the slurry-fabricated Gr electrodes and 150 mg of $\text{Li}_6\text{PS}_5\text{Cl}$ powders ($\sim 730 \mu\text{m}$) as the SE layer were employed. For the Gr/Ni-NW/Li-In all-solid-state three-electrode cells, the slurry-fabricated Gr electrodes were used. The Ni-NW electrode were prepared by depositing Ni on NW using a DC sputtering system (Sorona, SRN-120) at 700 W for 25 min at 10 mTorr under Ar. All the procedures were performed in a polyaryletheretherketone (PEEK) mold (diameter = 1.3 cm) with Ti metal current collectors (Figure 2). All the processes for fabricating the all-solid-state cells were performed in an Ar-filled dry box. The Sn/ Li-In(-SE) half-cells, NCM/Gr and NCM/Si-C full-cells were cycled at the targeted C-rates at 30°C between 0.0-2.0 V, 2.50-4.20 V and 1.20-4.25 V, respectively. All the all-solid-state cells were cycled under 74 MPa. The galvanostatic charge-discharge tests were carried out by applying the current

between WE and CE while the open-circuit voltage of WE/RE was measured.

For the diagnostic study of ASLBs using pressure monitoring system. The NCM622/graphite all-solid-state cells were fabricated from a 15 mg of a mixture of NCM622, LPSCl and super C65 with 70:30:3 weight ratio and 8.8 mg of a mixture of graphite, LPSCl (and/or LGPS) with 6:4 weight ratio were used as positive and negative composite electrodes, respectively. The np ratios (the areal capacity ratio of negative to positive electrodes) for NCM/Gr full cells were approx. 1.2, which is calculated from graphite electrode with LPSCl. The button load cell (CBFS, Bongshin) was used for pressure monitoring system (Figure 4). NCM/Gr full-cells with mixtures of LPSCl and LGPS (LPSCl:LGPS=100-x:x, x=0, 10, 20, 100 wt.%) were charged at same amounts of Li extracted from NCM622 electrode (4.3 V vs. Li/Li⁺) and then discharged 2.5 V at 30°C. For the ex-situ XRD measurements, NCM/Gr full-cells measured using a MiniFlex 600 (Rigaku Corp.) at 40 kV and 15 mA.

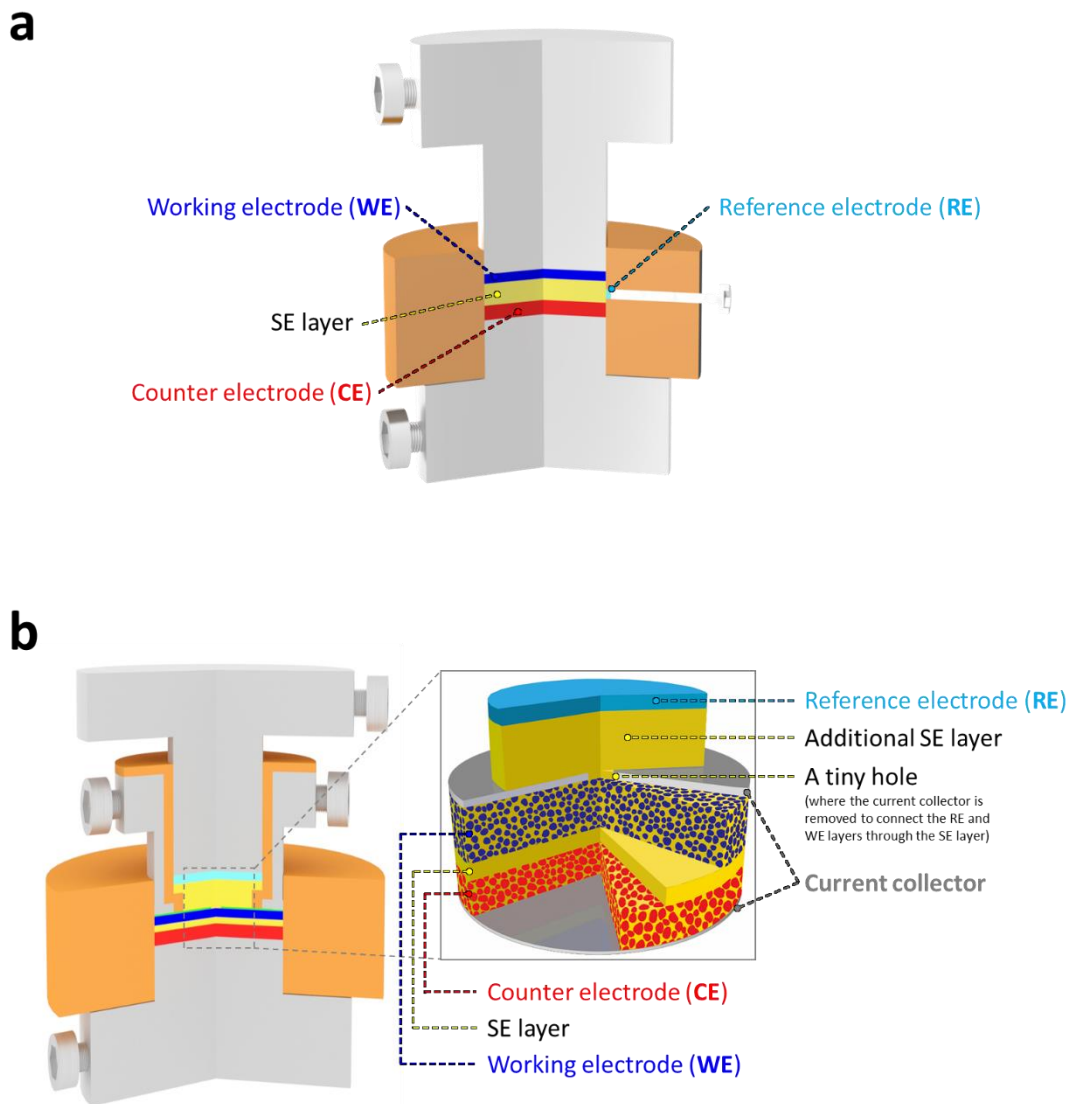


Figure 3. Schematic diagram of bulk-type three-electrode all-solid-state cells.

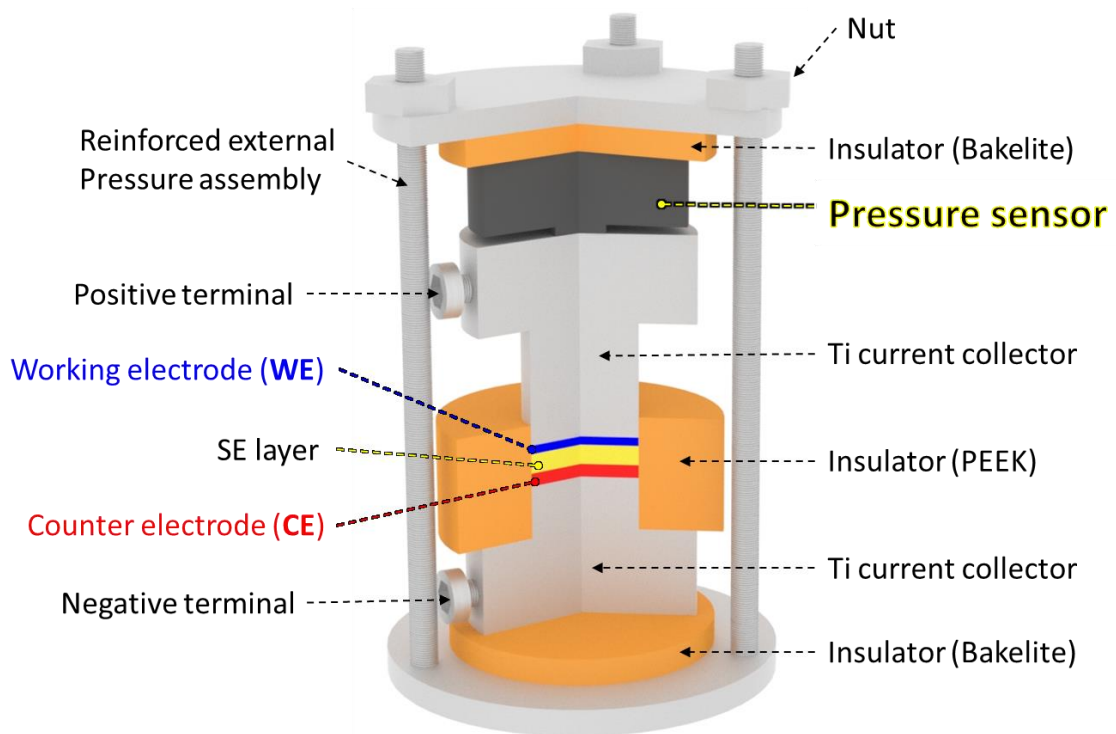


Figure 4. Schematic diagram of the operando stress measurement of bulk-type all-solid-state batteries.

4. Results and Discussion

4.1. Sheet-Type Electrodes & Solid Electrolyte Films

4.1.1. Solid Electrolyte Films

Most of the previous studies of ASLBs have not paid much attention to cell-based (not electrode-material-based) energy densities, which are far too low to compete with those of conventional LIBs. ASLBs contain excessively large amounts of SE which nullify the advantages of using high-energy electrode materials. Approximately, 30-70 wt.% of SEs are used in the composite electrodes, which, conversely, results in a 30-70% decrease in the corresponding energy density based on composite electrodes.^{7-8, 14-15, 23, 27, 55-56} In order to minimize the amount of SE in the composite electrodes, laser vapor deposition was used to directly coat the active materials (LiCoO₂ (LCO)) with SE thereby forming intimate contacts between the two.²⁴ Recently, solution-processable SE solution methods have been also investigated to deposit the SE layers on the active materials.^{26-27, 50-52} More importantly, it should be noted that the typical lab-made pellet-type ASLBs consist of a very thick (~0.5-1.0 mm) SE layer with a mass loading in the range of ~90-150 mg cm⁻².^{23, 26-27, 52, 55-56}; this very thick SE layer results, undoubtedly, in a significant decrease in the energy density of the cell. From the viewpoint of cell energy density and scalable fabrication, the technology level of ASLBs is also in a stage of infancy.^{25, 27, 29, 64} In this regard, the scalable fabrication of ASLBs using slurry process is essential.

In this part, the first ever bendable and thin sulfide SE films reinforced with a mechanically-compliant poly(paraphenylene terephthalamide) (PPTA) non-woven (NW) scaffold were fabricated by facile scalable process, which enables the fabrication of free-standing and stackable ASLBs with high energy and high rate capabilities. The free-standing and stackable ASLB consists of a LiCoO₂ cathode, a Li₄Ti₅O₁₂ anode, and a thin (~70 μm) NW-reinforced SE (referred as “NW-SE” hereafter) film; the LiCoO₂ has a clean surface that was prepared by heat-treating in air. Furthermore, by incorporating the bendable NW-SE film, the cell energy density of the ASLB is increased by a factor of three compared to that of the conventional cell that does not contain NW.

4.1.1.1. Properties of Solid Electrolyte Films

The fabrication process of the NW- SE films is illustrated in Figure 5. The sulfide SE used was either glass-ceramic Li_3PS_4 (LPS, pristine: $1.0 \times 10^{-3} \text{ S cm}^{-1}$ at 30°C , after exposure to anhydrous toluene: $7.3 \times 10^{-4} \text{ S cm}^{-1}$) or tetragonal $\text{Li}_{10}\text{GeP}_2\text{S}_{12}$ (LGPS, pristine: $6.0 \times 10^{-3} \text{ S cm}^{-1}$ at 30°C , after exposure to anhydrous toluene: $4.0 \times 10^{-3} \text{ S cm}^{-1}$).⁵⁵ Fabrication of the films begins with using the doctor-blade method to coat the sulfide SE slurry (using anhydrous toluene as a solvent) on a Ni foil and the subsequent drying. The as-prepared SE-coated Ni foil is then cold-pressed onto the NW substrate. This pressing results in the transfer of the SE layer from the Ni foil to the NW substrate owing to the better adhesion of the SE layer toward the NW substrate than the Ni foil. Two different configurations (“SE-NW-SE” and “NW-SE-NW”) of the NW-SE films were prepared *via* this ‘transfer’ method. Even though a “SE-NW” film also can be fabricated, in this work only the films of symmetric configuration were used for reasonable evaluation on further electrochemical tests. The as-prepared SE-NW-SE and NW-SE-NW films are both free-standing, have a mass loading of $\sim 5.7 \text{ mg cm}^{-2}$ and are $\sim 70 \mu\text{m}$ -thick. In addition, the PPTA NW is very light (0.8 mg cm^{-2}) and constitutes only 14% of the mass of the NW-SE film (SE-NW-SE). This PPTA NW, which is known as a high-performance polymer with good thermal, chemical, and electrochemical stability,¹²⁷ serves as a mechanically compliant scaffold that provides flexibility and toughness to the NW-SE film. Especially, the PPTA NW is stable up to $\sim 400^\circ\text{C}$ (Figure 6), which demonstrates that the inclusion of organic component, PPTA NW, does not significantly degrade the intrinsic advantage of excellent thermal stability of sulfide SEs. With a thickness of only $16 \mu\text{m}$, the PPTA NW is also thin, and has a high porosity (70%) as well as large opening sizes ($\sim 40 \mu\text{m}$) (Figure 7). These features allow easy penetration of the sulfide SE particles into the pores of the PPTA NW, as evidenced by the merged SE materials observed at the openings of the NW of the NW-SE-NW film in Figure 1. Moreover, the marginal decreases in conductivity values (Table 1) of the NW-SE films (0.20 mS cm^{-1} for LPS-NW-LPS and 0.16 mS cm^{-1} for NW-LPS-NW) compared to those of conventional SE films (0.73 mS cm^{-1}) confirm that good ionic conduction pathways formed in the SE materials that were impregnated inside the NW scaffold. Note, however, that the conductance values of the NW-SE films (37 mS for LPS-NW-LPS and 29 mS for NW-LPS-NW) are higher than that of the conventional SE film (14 mS). The comparison of the conductivity and conductance values shown in Table 1 will be further discussed in a later section. In a previous report,⁵⁵ our group demonstrated that, by using a LGPS-LPS SE bilayer in which LPS faces the Li-In anode (operating voltage: $\sim 0.62 \text{ V}$ vs. Li/Li^+ for $\text{In} + \text{Li}^+ + \text{e}^- \leftrightarrow \text{LiIn}$), it is possible to overcome the poor stability problem of $\text{Li}_{10}\text{GeP}_2\text{S}_{12}$ (LGPS) in contact with Li-In with exploiting the high conductivity of $\text{Li}_{10}\text{GeP}_2\text{S}_{12}$ (LGPS) in the $\text{TiS}_2/\text{Li-In}$ all-solid-state cell. A thin and free-standing bi-layer NW-SE film, which consists two different SE layers and NW, and thereby allows wide electrochemical window with retaining high ionic conductivity, can also be fabricated by using the ‘transfer’ method. For example, a free-standing LGPS-

LPS bilayer SE film can be fabricated as combinations of LPS-NW-LGPS or NW-LGPS-LPS-NW (Table 1).

Figure 8a compares photo images of the SE films, with and without the NW scaffold, immediately after cold-pressing. As evidenced by the cracks (indicated by the arrow) formed, cold-pressing resulted in severe mechanical failure of the 470 μm -thick conventional Li_3PS_4 SE film. Considering that the diameter of pellet is only 1.3 cm, it should be emphasized that this mechanical failure must be critically severer when the SE films with larger dimension are fabricated for scalable production. In sharp contrast, the SE-NW-SE and NW-SE-NW SE films remained intact during cold-pressing. Although sulfide materials are ductile, cold-pressing is insufficient for the formation of pore-free SE monoliths. In fact, field emission scanning electron microscopy (FESEM) images (Figure 9) revealed the presence of voids between the merged particles of the cold-pressed LPS SE pellets. The pellets were found to have a porosity of 14-17% as determined by calculations based on the comparison of the apparent, i.e., from the crystallographic data,^{24, 128} and the measured densities. The mechanical failure of conventional SE films without the NW scaffold in Figure 8a originates from the aforementioned mechanical imperfection. It is thought that breakage of the pellet, which is initiated at the microstructural defects or voids by the strain caused by cold-pressing, is accelerated in insufficiently thick SE films. In contrast, owing to the highly flexible NW scaffold, the as-prepared NW-SE-NW film is both free-standing and bendable and, as such, can be easily wound around a 3 cm diameter rod (Figure 8b). Mechanical integrity of NW-SE-NW films on repeated bending was assessed by bending the $1.5 \times 2.0 \text{ cm}^2$ films ten times around rods with three different diameters of 1, 2, and 3 cm, and the results are shown in Figure 8c. While the contacts among SE particles and between SE particles and NW frameworks are seen to be slightly loosened and some SE particles are detached for the case of bending around the 1 cm rod, the structural integrity was remained for the cases of bending around the 2 and 3 cm rods, manifesting the excellent mechanical flexibility of composite film. To the best of my knowledge, this work is the first report on flexible inorganic SE films with significant bendability. It should be emphasized that the free-standing feature or bendability of the NW-SE films could provide a viable option to allow roll-to-roll processes. In addition, the technology used to fabricate the NW-SE films has the potential to ultimately realize bendable bulk-type all-solid-state batteries based on inorganic SEs.¹²⁹

As Table 1 shows, the bendable NW-SE films have lower conductivity values than those of their conventional SE counterparts, which is not surprising because the NW scaffold is not Li^+ -ion conductive. As demonstrated, however, the use of NW allows the fabrication of very thin ($\sim 70 \mu\text{m}$) bendable composite films (Figures 5 and 8), which appear to have higher conductance values than those of the conventional thick SE film (Tables 1 and 2). All-solid-state cells incorporating LiTiS_2 (LTS) and $\text{Li}_4\text{Ti}_5\text{O}_{12}$ (LTO) as the cathode and anode, respectively were fabricated in order to make a fair

assessment of the benefit of the high conductance of the bendable NW-SE films. LTS and LTO operate at mild voltages (~ 2.1 V *vs.* Li/Li⁺ for LTS and ~ 1.6 V *vs.* Li/Li⁺ for LTO) (Figure 10) and thus their use of nano-sized particles is not problematic. As such, the charge transfer resistance at the electrode-electrolyte interfaces and Li⁺-ion diffusion in the bulk are expected to have inappreciable effect on the overall rate performance.¹²

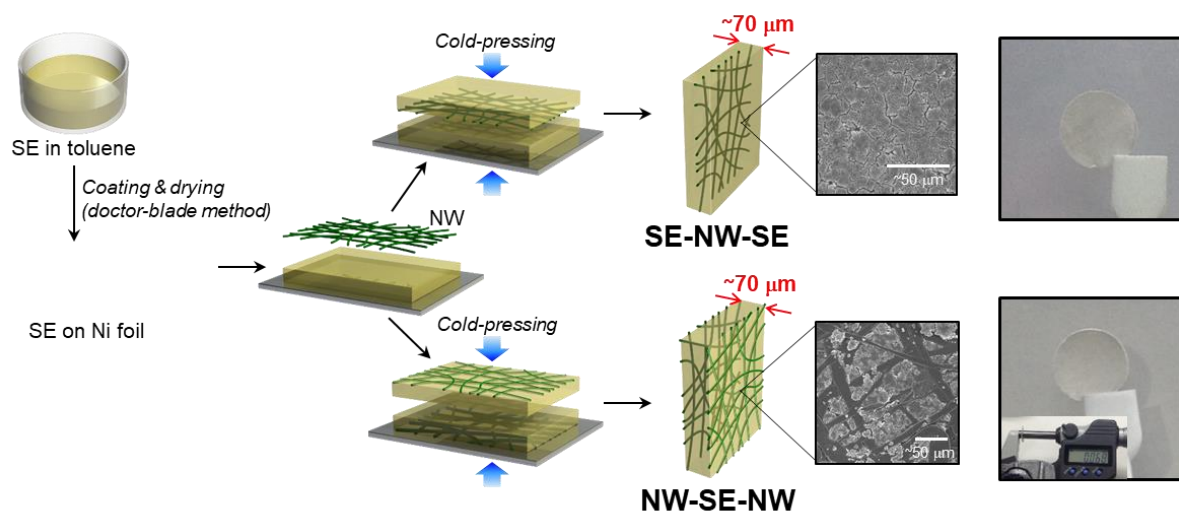


Figure 5. Schematic diagram showing the fabrication of bendable sulfide NW-SE films with two different structures (SE-NW-SE and NW-SE-NW). FESEM and photo images are also provided.

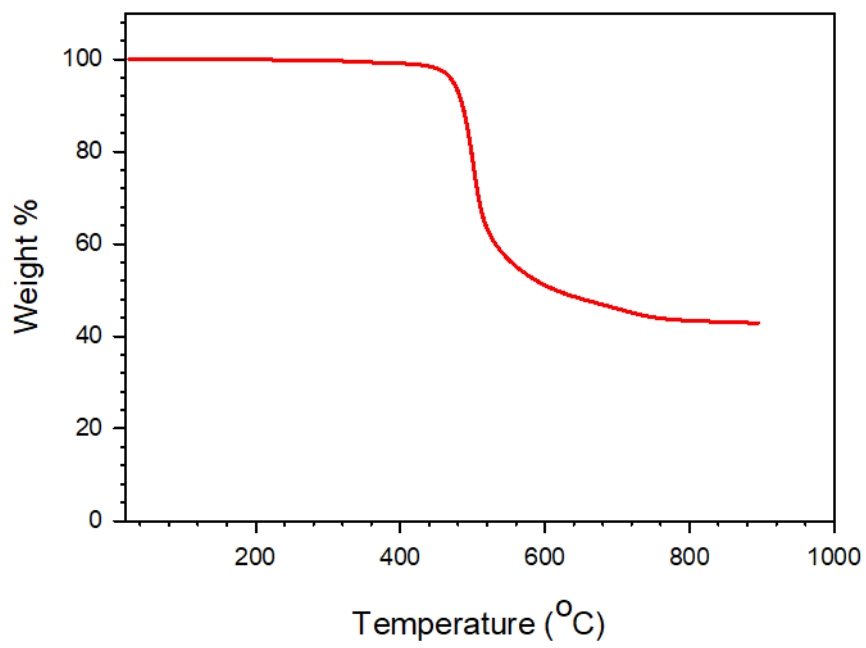


Figure 6. TGA curve of PTTA NW under Ar.

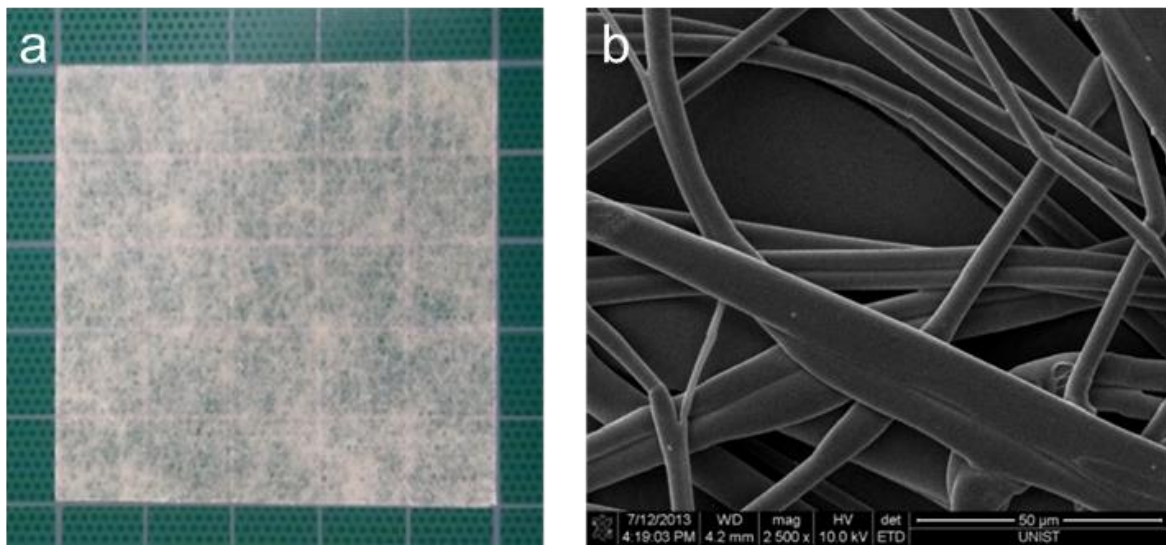


Figure 7. Photo and FESEM images of the poly(paraphenylene terephthalamide) (PPTA) NW scaffold.

Table 1. Major characteristics of the NW-SE films.

Name of SE films	Conductivity (mS cm ⁻¹)	E _a (kJ mol ⁻¹)	Thickness (μm)	Mass loading (mg cm ⁻²)	Conductance (mS)
LPS ^a	0.73	26.0	700	110	14
LPS-NW-LPS	0.20	31.0	70	5.7	37
NW-LPS-NW	0.16	49.2	70	5.7	29
LGPS-NW-LPS	0.34	24.8	90	11 ^b	50
NW-LGPS-LPS-NW	0.20	44.0	90	11 ^b	20

^aFor fair comparison with the NW-SE films, the LPS SE powders were exposed to anhydrous toluene.

^bWeight ratio of LGPS/LPS is 1.4.

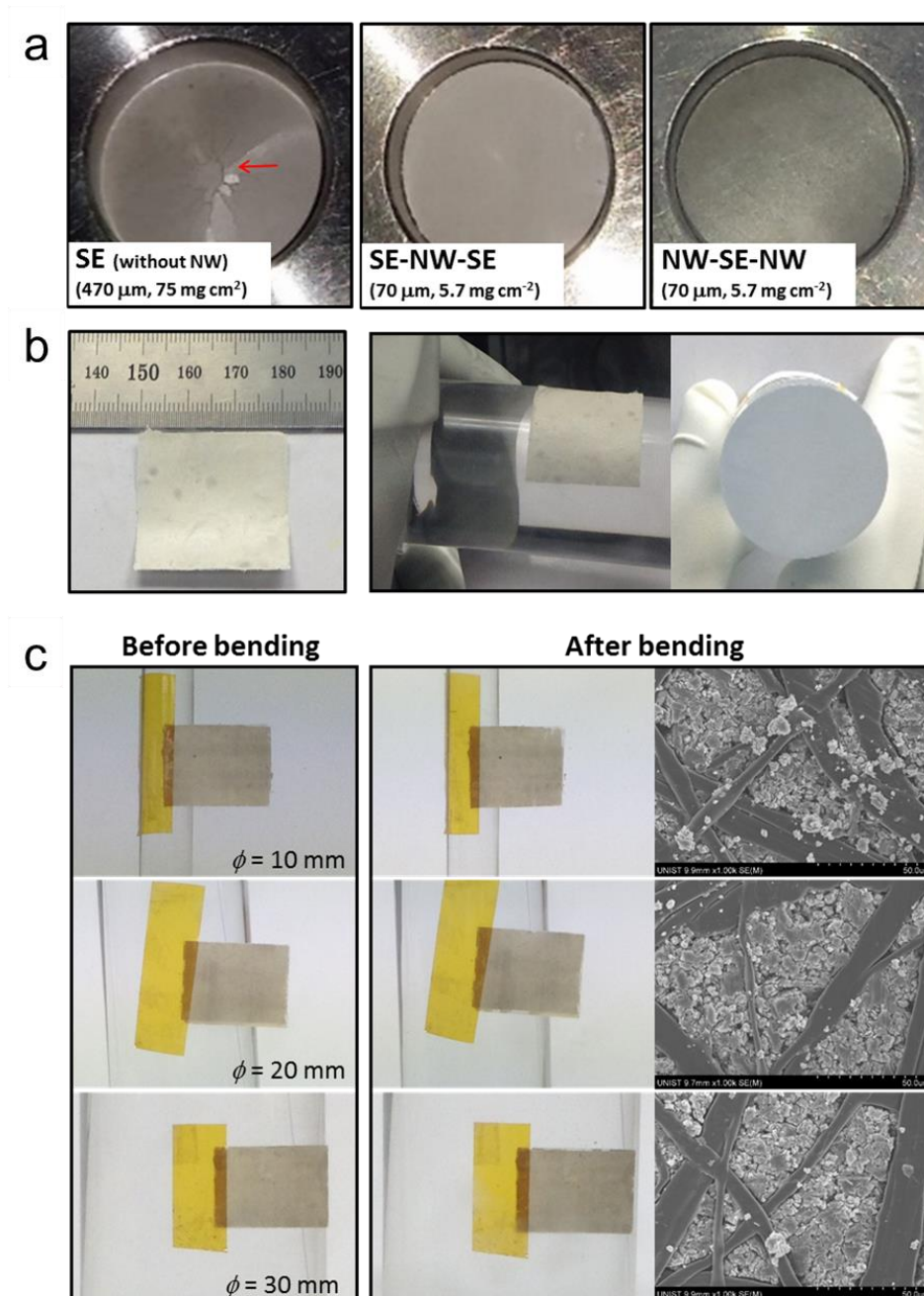


Figure 8. a) Photo images of the conventional SE pellet and bendable NW-SE films. The pellets have a diameter of 1.3 cm. Note the cracks in the conventional SE pellet, as indicated by the arrow. b) Photo images of $3 \times 3 \text{ cm}^2$ bendable NW-SE films (NW-SE-NW). c) Photo and FESEM images of $1.5 \times 2.0 \text{ cm}^2$ bendable NW-SE films (NW-SE-NW) before and after bending tests. The diameter of rods is provided. Li_3PS_4 (LPS) was used as the SE.

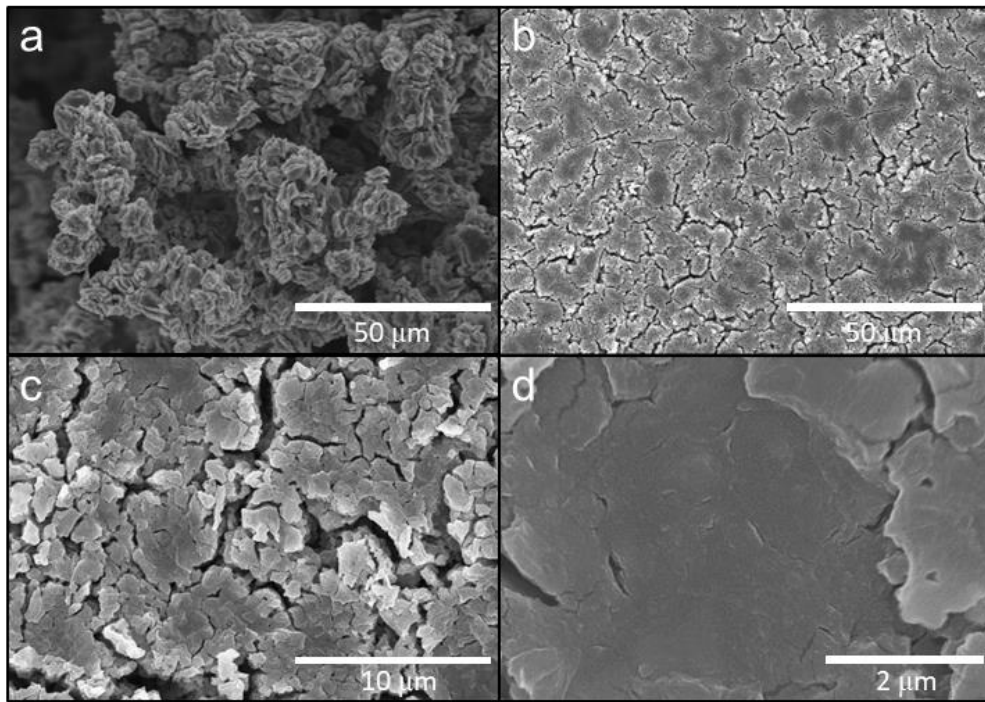


Figure 9. FESEM images of the a) LPS powders and b-d) cold-pressed pellets.

Table 2. Major characteristics of the LGPS-based SE films.

Name of SE films	Conductivity [mS cm ⁻¹]	E _a (kJ mol ⁻¹)	Thickness [μm]	Mass loading [mg cm ⁻²]	Conductance [mS]
LGPS ^a	4.0	24.3	700	110	76
LGPS-NW-LGPS	0.68	21.4	90	7.2	100
NW-LGPS-NW	0.34	43.7	90	7.2	50

^{a)} For fair comparison with the NW-SE films, the LGPS SE powders were exposed to anhydrous toluene

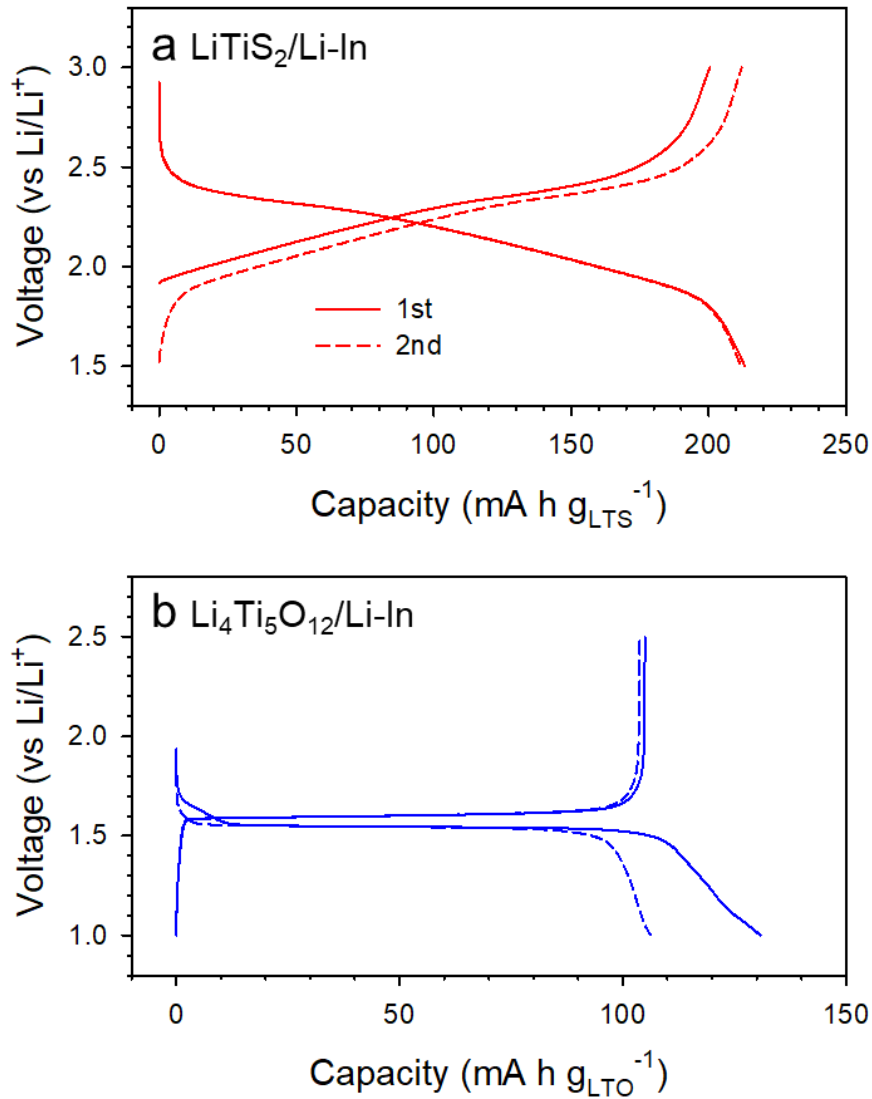


Figure 10. First two charge-discharge voltage profiles of the a) $\text{LiTiS}_2/\text{Li-In}$ (LTS/Li-In) and b) $\text{Li}_4\text{Ti}_5\text{O}_{12}/\text{Li-In}$ (LTO/Li-In) all-solid-state cells at 30 °C. The current densities of the LTS/Li-In and LTO/Li-In cells were $50 \text{ mA g}_{\text{LTS}}^{-1}$ ($55 \mu\text{A cm}^{-2}$) and $22 \text{ mA g}_{\text{LTO}}^{-1}$ ($55 \mu\text{A cm}^{-2}$), respectively.

4.1.1.2. Sheet-Type All-Solid-State Lithium-Ion Batteries using Solid Electrolyte Films

The electrochemical performances of the LTS/LTO all-solid-state cells containing the conventional SE film ('SE') to that of the bendable NW-SE films (SE-NW-SE and NW-SE-NW) are compared in Figures 11-13. In contrast to the cell with conventional SE film that has negligible capacity at high C-rates, i.e., $\sim 32 \text{ mA h g}_{\text{LTS}}^{-1}$ at 29C (4.4 mA cm^{-2}), the cell with SE-NW-SE film exhibits lower polarization and thus higher capacities. This enhanced rate performance is attributed to the higher ionic conductance of the latter (37 mS) compared to that of the former (14 mS) (Table 1). Electrochemical impedance spectroscopy (EIS) results of the LTS/LTO cell also show that the intercept values at the Z' axis in the Nyquist plots (Figure 12a), which are interpreted as resistance of the SE layers,^{23,26-27,55} of the SE-NW-SE and NW-SE-NW cells are lower than that of the cell with the conventional SE. However, the rate capability of the cell with the NW-SE-NW film is slightly inferior to that of the conventional cell. The Nyquist plots in Figure 12a show that the data in mid-frequency ranges for the cell containing NW-SE-NW exhibit more depressed shape than others (SE and SE-NW-SE). This indicates that the cell containing NW-SE-NW has a higher charge transfer resistance compared to that of the other two cells. Fitting of the EIS data using Voigt-type equivalent circuit model (Figures 12b and 12c) results in the overall charge transfer resistances of 5.4 Ω , 7.2 Ω , and 143 Ω for the SE, SE-NW-SE, and NW-SE-NW cells, respectively. The suppressed charge transfer kinetics may have resulted from blocking of the ionic conduction between the active materials and the SE by the non-conductive NW scaffold at the composite electrode-SE interface, which explains the inferior rate capability of NW-SE-NW cell to the conventional SE cell (Figure 11) in spite of the higher conductance of NW-SE-NW (29 mS) than that of SE (14 mS) (Table 1). Future work will include development of a Li-ion conducting NW scaffold in order to further enhance the rate performance of NW-SE-containing cells. A prototype $1.5 \times 1.5 \text{ cm}^2$ free-standing LTS/(SE-NW-SE)/LTO sheet battery was fabricated and its reversible electrochemical behavior is also demonstrated in Figure 13.

In addition, LCO and LTO were selected as cathode and anode, respectively, in order to examine the performance of high-energy all-solid-state cells which incorporate the bendable SE films. High mass-loading of LCO (LCO:LGPS = 70:30 wt.%) was performed in order to maximize the cell energy density. The pristine LCO in LCO/Li-In cell exhibits a first discharge capacity of only 8 mA h $\text{g}_{\text{LCO}}^{-1}$ at 0.1C ($14 \text{ mA g}_{\text{LCO}}^{-1} = 0.11 \text{ mA cm}^{-2}$) (Figure 14). Surprisingly, the use of heat-treated (at 800°C in air) LCO significantly improves the electrochemical performance, resulting in a first discharge capacity of 121 mA h $\text{g}_{\text{LCO}}^{-1}$ (Figure 14). In previous literatures related to LE-based LIBs, it was argued that, improvements of performance in LCO by metal-oxides coatings is due to elimination of impurities such as LiOH and Li_2CO_3 during the heat-treatment used for the wet-coating procedures rather than the protective role of metal-oxide coatings.¹³⁰⁻¹³² In ASLBs, the surface impurities may block the transport of Li ions between the SE and the LCO particles with whom they contact. This blocking results in a

huge impedance and thus negligible capacity, which is verified by the significantly higher amount of Li_2CO_3 in the pristine LCO (4400 ppm) than in the heat-treated LCO (1000 ppm). Even if the electrochemical performance of LCO depending on the surface chemistry is important, it is beyond the scope of current work.

By combination of the heat-treated LCO with the SE-NW-SE (or NW-SE-NW) film and Ni-coated NW (acting as a flexible current collectors), a free-standing LCO/LTO all-solid-state cell was fabricated. The cell structure is depicted in Figure 15a. Figure 15b shows that the cell has an overall thickness $\sim 185 \mu\text{m}$ and the photo images in Figure 15c demonstrate the corresponding free-standing characteristics. Figure 16 represents the voltage profiles of the free-standing LCO/LTO all-solid-state cells. The corresponding cycle performances are also represented in Figure 17. The composite cathode (15 mg cm^{-2}) and anode (24 mg cm^{-2}) include 70.0 wt.% of LCO and 49.8 wt.% of LTO, respectively. The SE-NW-SE and NW-SE-NW cells had respective first discharge capacities of $85 \text{ mA h g}_{\text{LCO}}^{-1}$ and $75 \text{ mA h g}_{\text{LCO}}^{-1}$. The lower capacity of the latter, compared to the former, is considered to arise from poor ionic contacts at the LCO cathode/(NW-SE-NW) interface. In order to improve the capacity, a polymer electrolyte consisting of LiTFSI (lithium bis(trifluoromethanesulfonyl)imide) with PEO (poly(ethylene oxide)) was coated on the NW scaffold, yielding a PEO/LiTFSI-coated NW scaffold denoted as “*p*NW”. The presence of coating layer was confirmed not only by the elemental maps of the as-prepared *p*NW by FESEM analysis (Figure 18a) but also by the HRTEM results of cross-sectioned *p*NW by using focused ion beam (FIB) etching (Figure 18b). Especially, from the HRTEM results in Figure 18b, it is seen that the coating layer is uniform and has an estimated thickness of $\sim 20\text{-}40 \text{ nm}$. As seen in Figure 16, the first discharge capacity of the LCO/LTO cell incorporating the *p*NW, *p*NW-SE-*p*NW, is significantly higher ($89 \text{ mA h g}_{\text{LCO}}^{-1}$ vs. $75 \text{ mA h g}_{\text{LCO}}^{-1}$) than that of the NW-SE-NW. The respective first discharge capacities of the SE-NW-SE and *p*NW-SE-*p*NW LCO/LTO cells, $85 \text{ mA h g}_{\text{LCO}}^{-1}$ and $89 \text{ mA h g}_{\text{LCO}}^{-1}$, translate to energy density values of $42 \text{ Wh kg}_{\text{cell}}^{-1}$ and $44 \text{ Wh kg}_{\text{cell}}^{-1}$. Figure 19 shows the cell energy density of all-solid-state cells as a function of the overall weight fraction of SE. The energy density obtained in this work ($44 \text{ Wh kg}_{\text{cell}}^{-1}$) is still much lower than that ($100\text{-}200 \text{ Wh kg}_{\text{cell}}^{-1}$) of commercialized LIBs and also some conventional ASLB adopting high-capacity electrode materials such as sulfur (e.g. $\sim 150 \text{ Wh kg}_{\text{cell}}^{-1}$ assuming that Li metal can be used.). It should be noted, however, that by applying the bendable and thin NW-SE film, the energy density of the LCO/LTO ASLB was almost three times higher than that of the conventional ASLB ($15 \text{ Wh kg}_{\text{cell}}^{-1}$) that does not contain NW. If novel electrode chemistry such as sulfur¹²² and/or an SE-coated electrode materials²⁴ is combined with the NW-SE film, further improvement in the energy density is highly expected. For example, consider the case of an NW-SE film sandwiched between LCO and graphite composite electrodes, in which the electrode powders are coated by 10 wt.% of SE *via* a pulsed laser deposition method. The overall weight fraction of SE would be reduced to as low as $\sim 25 \text{ wt.}\%$ and the cell energy

density would be increased to $\sim 190 \text{ Wh kg}_{\text{cell}}^{-1}$, i.e., 4.3 times that of the original NW-SE film. This value ($\sim 190 \text{ Wh kg}_{\text{cell}}^{-1}$) is comparable to the values for conventional LIBs that use LEs. In addition, an energy density of over $860 \text{ Wh kg}_{\text{cell}}^{-1}$ is expected if an ASLB were to be composed of the state-of-the-art sulfur cathode and a Li anode that contains the NW-SE film. This value ($860 \text{ Wh kg}_{\text{cell}}^{-1}$) would represent a 5.7-fold increase compared to that of the non-NW-containing cell, and far exceeds that of the conventional LIBs.

The free-standing feature of the (NW-SE)-incorporated ASLB also facilitates stacking of mono-cells. Voltages can be easily doubled or tripled *via* simple stacking of pre-charged $\text{Li}_{1-x}\text{CoO}_2/\text{Li}_{4+x}\text{Ti}_5\text{O}_{12}$ mono-cells. In addition, capacities of the free-standing bipolar cell constructed by stacking two free-standing mono-cells (LCO/(SE-NW-SE)/LTO) are comparable to those of the mono-cell, as demonstrated in the first charge-discharge voltage profiles (Figure 15c). For the conventional LIBs using LEs, in contrast, achieving targeted high voltages of battery packs (e.g. tens of V) is possible only through serial connections of each fully-packaged mono-cell. Considering weight of cell-packaging, the overall cell energy density increases with increasing number of mono-cells stacked in the ASLBs.

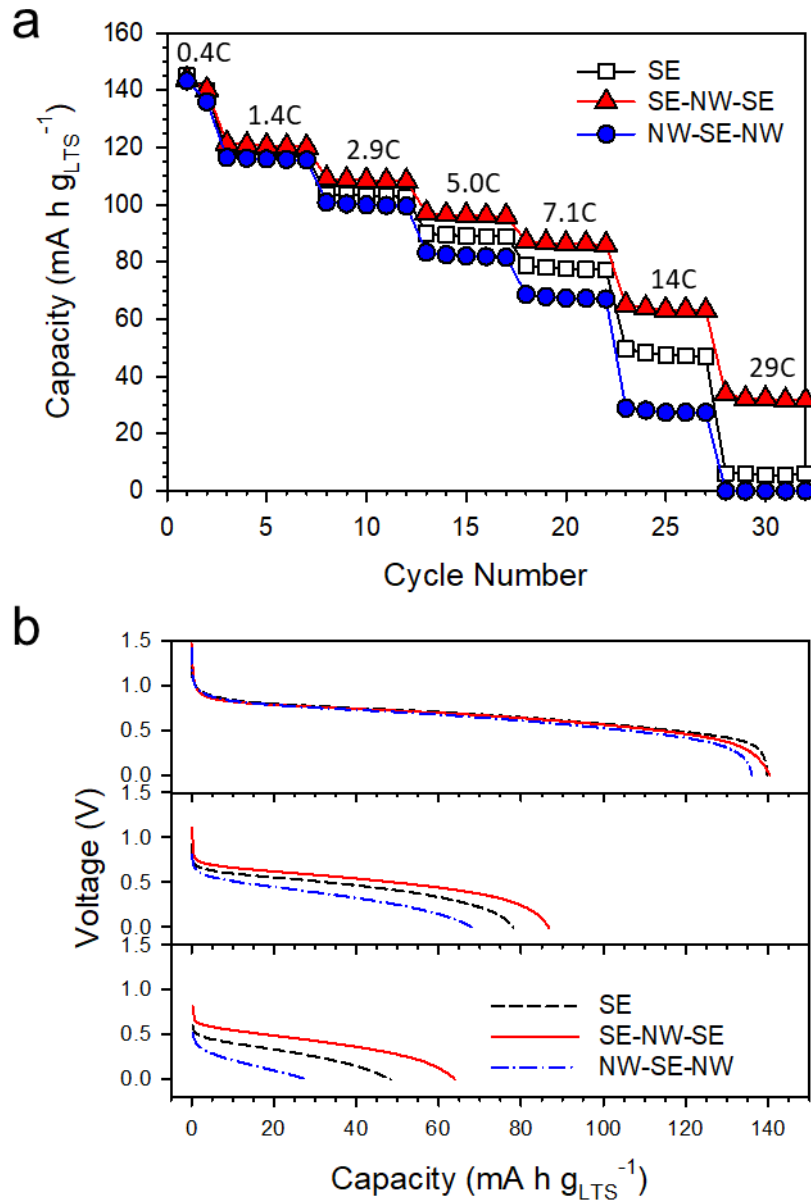


Figure 11. a) Variations in discharge capacities versus cycle number, and b) discharge voltage profiles at different C-rates of LiTiS₂/Li₄Ti₅O₁₂ (LTS/LTO) all-solid-state cells using the conventional SE pellet and bendable NW-SE films as the SE layer at 30 °C.

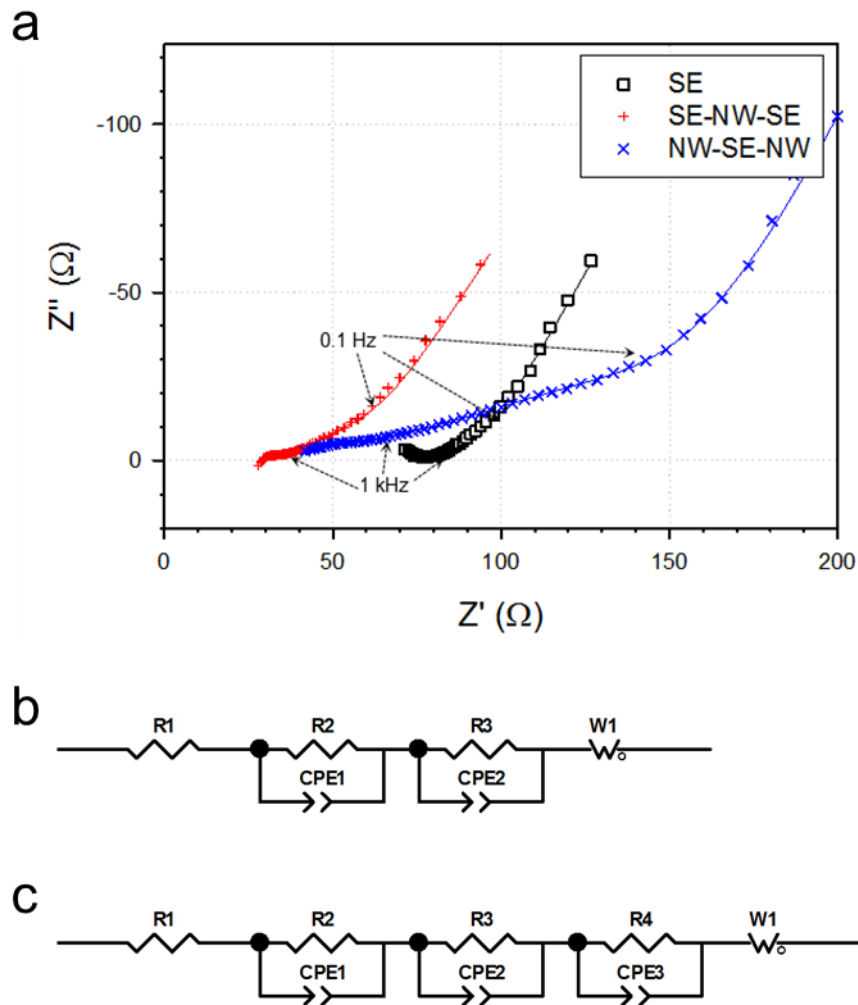


Figure 12. a) Nyquist plots of $\text{LiTiS}_2/\text{Li}_4\text{Ti}_5\text{O}_{12}$ (LTS/LTO) all-solid-state cells using the conventional SE pellet and bendable NW-SE films as the SE layer at 30°C . Voigt-type equivalent circuit models used for fitting the EIS results for b) the SE and the SE-NW-SE cells and c) the NW-SE-NW cell in Figure 12a. The solid lines indicate the fitting results using Voigt-type equivalent circuit model.

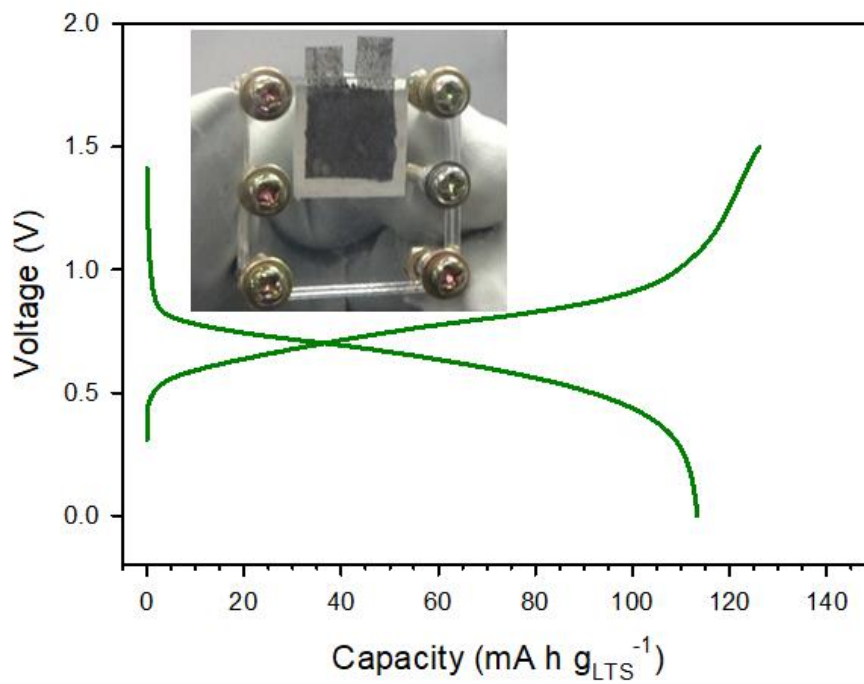


Figure 13. First charge-discharge voltage profiles of the prototype free-standing LTS/LTO sheet battery at $89 \mu\text{A cm}^{-2}$ at $30 \text{ }^\circ\text{C}$. A photo image of the LTS/LTO sheet battery is shown in the inset.

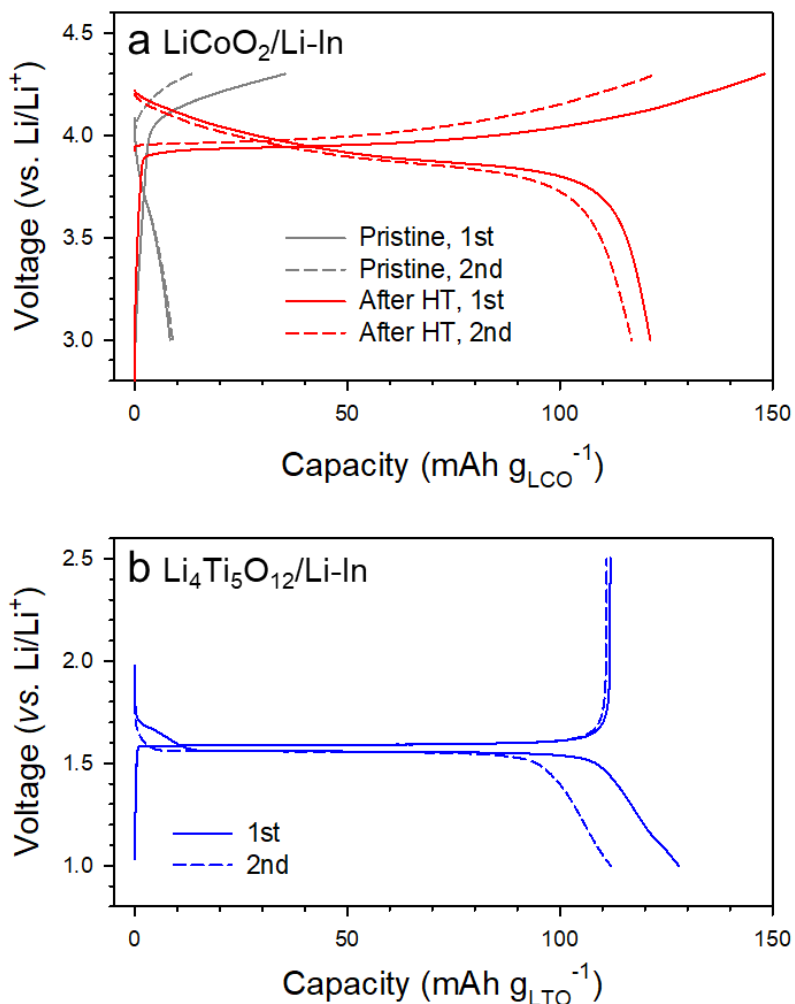


Figure 14. First two charge-discharge voltage profiles of the a) LiCoO₂/Li-In (LCO/Li-In) and b) Li₄Ti₅O₁₂/Li-In (LTO/Li-In) all-solid-state cells at 30 °C. The results of the pristine and heat-treated LCO are compared. The current densities of the LCO/Li-In and LTO/Li-In cells were 14 mA g_{LCO}⁻¹ (0.11 mA cm⁻²) and 12 mA g_{LTO}⁻¹ (0.11 mA cm⁻²), respectively.

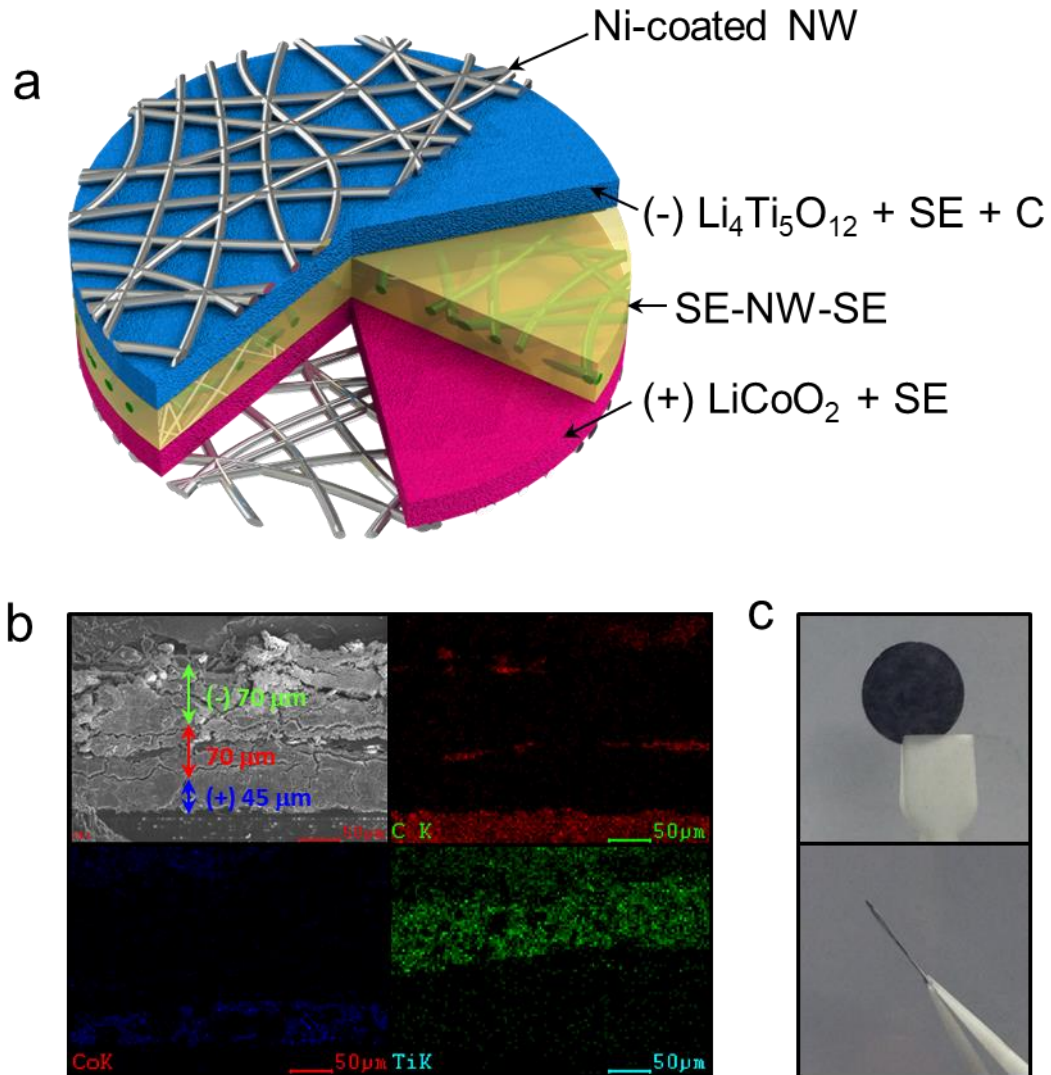


Figure 15. a) Schematic diagram, b) cross-sectional FESEM image and EDS elemental maps, and c) photo images of the free-standing $\text{LiCoO}_2/(\text{SE-NW-SE})/\text{Li}_4\text{Ti}_5\text{O}_{12}$ (LCO/(SE-NW-SE)/LTO) all-solid-state cell.

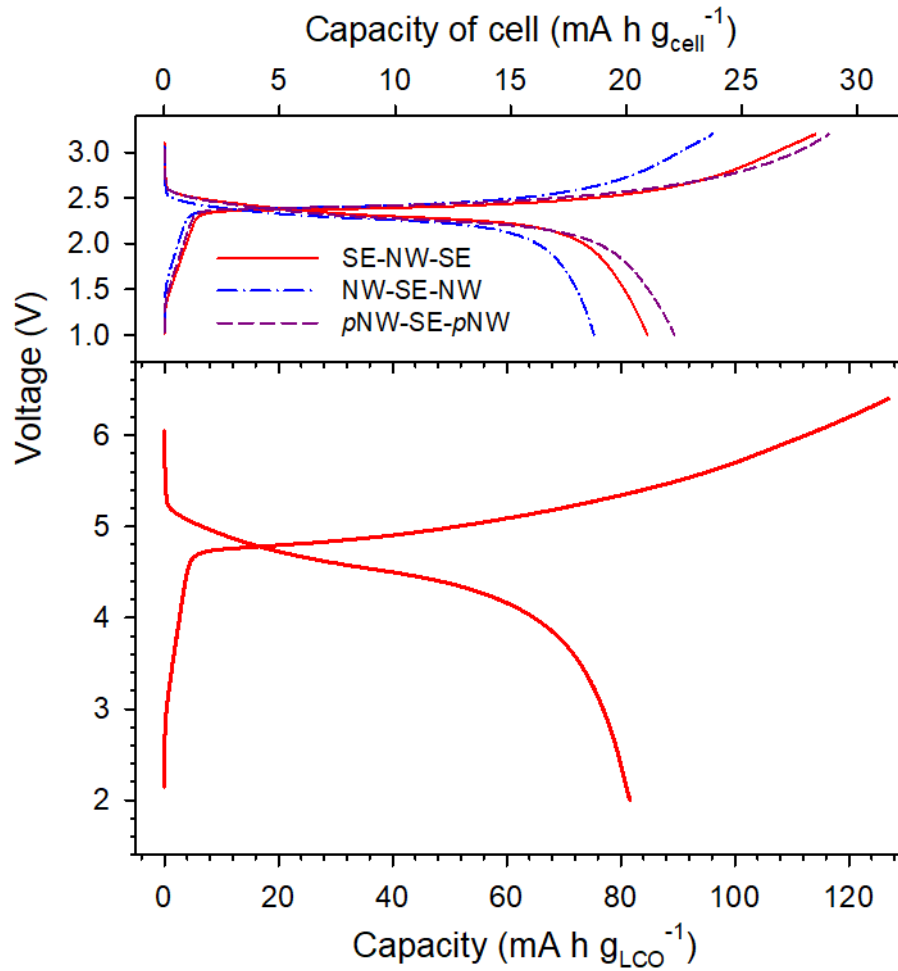


Figure 16. First charge-discharge voltage profiles of the free-standing LCO/LTO all-solid-state mono-cells with different-structured SE films (SE-NW-SE, NW-SE-NW, pNW-SE-pNW) and the free-standing bipolar cell constructed by stacking two free-standing mono-cells (LCO/(SE-NW-SE)/LTO) at $14 \text{ mA g}_{\text{LCO}}^{-1}$ ($= 0.11 \text{ mA cm}^{-2}$) at $30 \text{ }^\circ\text{C}$.

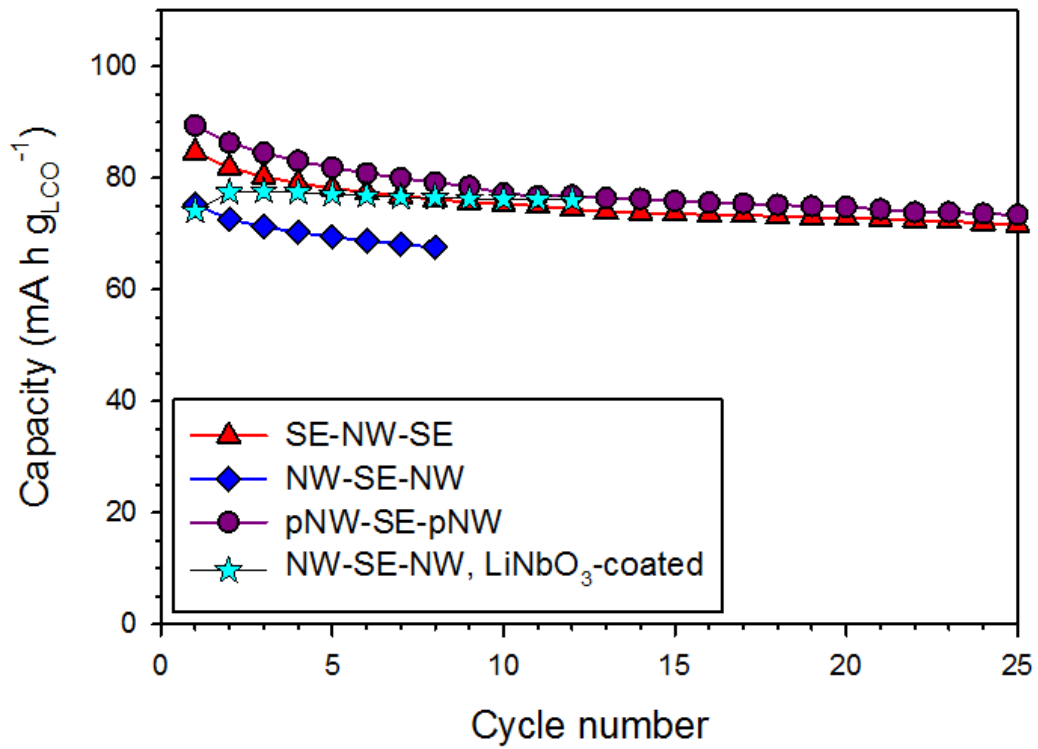


Figure 17. Cycle performances of the free-standing LCO/LTO all-solid-state cells. The data using 0.35 wt.% of LiNbO₃-coated LCO with the bendable NW-LPS-NW film is also represented for comparison.

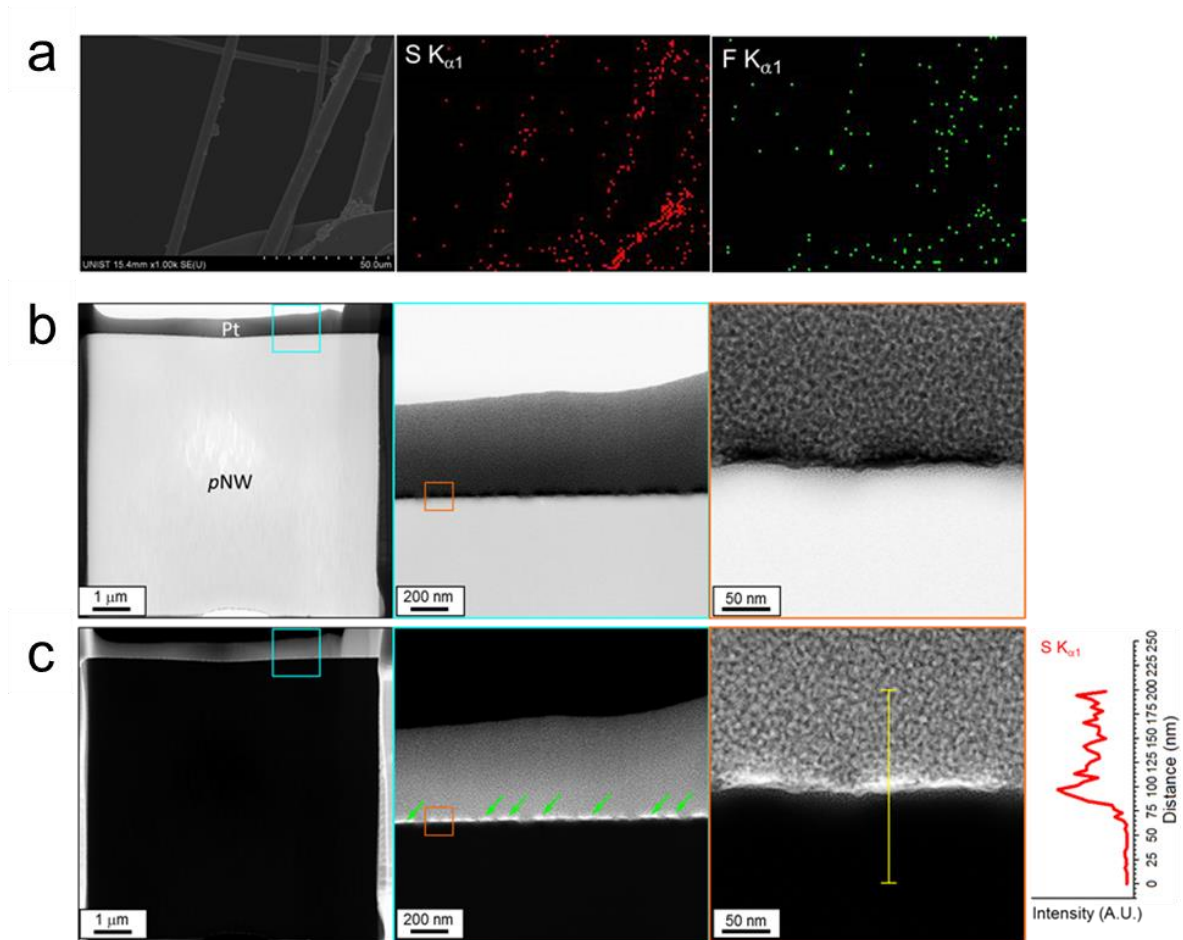


Figure 18. a) FESEM image and elemental maps of the PEO/LiTFSI-coated NW (*p*NW). b) Bright-field and c) dark-field images of the FIB-cross-sectioned *p*NW. The line scanning energy dispersive spectroscopy (EDS) result for S $K_{\alpha 1}$ signal is also provided. The arrows indicate the coating layers.

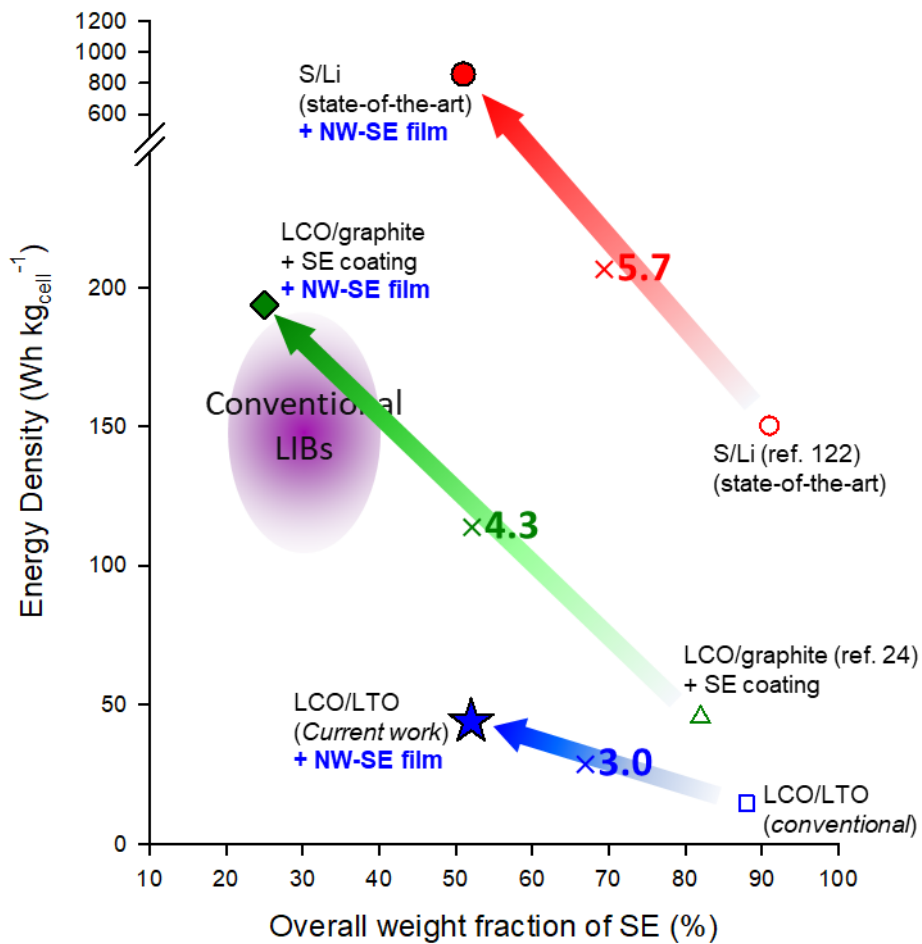


Figure 19. Comparison of the energy densities of the all-solid-state battery as a function of the overall weight fraction of SEs varied by electrode chemistry,¹²² the presence of SE coating,²⁴ and the bendable NW-SE film.

4.1.2. Sheet-Type Electrodes

In most previous reports, composite electrodes for bulk-type ASLBs using sulfide SEs were fabricated by mixing particulate active materials, SEs, and carbon additives in dry condition, followed by cold-pressing. However, the resulting pelletized electrodes were too mechanically unstable to be scaled up. Thus, addition of small amounts of polymeric binders is necessary to provide mechanical flexibility and good adhesion between particles and current collectors.^{29, 64-65} In turn, a scalable wet-slurry process using solvent to dissolve polymeric binders should be employed, which allows fabrication of large sheet-type electrodes.^{29, 64-65} The available solvents are restricted to nonpolar or less polar ones such as xylene and toluene, due to severe reactivity of sulfide materials with common polar solvents.^{23, 29} Moreover, the more complicated homogenization of three components in the polymer-binder-dissolved wet-slurry for ASLB electrodes (active materials, SEs, and carbon additives) is contrasted by the need for only two components for LIB electrodes (active materials and carbon additives).^{25, 27, 29, 64} Overall, the fabrication of sheet-type electrodes for ASLBs by the slurry method is much more complicated than that for well-optimized LIB electrodes.

Herein, the electrochemical performances of conventional dry-mixed electrodes without polymeric binders, and sheet-type electrodes fabricated using a wet-slurry process with polymeric binders, in various combinations of electrode composition and mass loading, were systematically investigated. A controlled premixing process for active materials and SEs is introduced as a scalable method to enhance utilization of the active materials in all-solid-state cells. Finally, high cell-based energy density (184 W h kg⁻¹ and 432 W h L⁻¹), and excellent safety for 80 × 60 mm² pouch-type LiNi_{0.6}Co_{0.2}Mn_{0.2} (NCM622)/graphite all-solid-state full-cells are highlighted.

4.1.2.1. Comparison of Electrodes Fabricated by Dry-mixing and Wet-slurry processes

Two types of composite electrodes for all-solid-state cells were fabricated: i) by dry-mixing active materials with SEs and super C65 in an agate mortar without polymeric binders (Figure 20a), and ii) by wet-mixing a slurry comprising active materials, SEs, super C65, and nitrile-butadiene rubber (NBR) in anhydrous xylene (Figure 20b). The Raman and Fourier-transform infrared (FTIR) spectra are provided in Figure 21, where the characteristic peaks match well with the functional groups for NBR. The as-prepared slurry was coated on current-collectors of Al or Ni foils for positive and negative electrodes, respectively, followed by drying under vacuum at 120 °C. The resulting sheet-type electrodes exhibited good adhesion to the current collectors (Figure 20c). Hereafter, the electrodes fabricated by dry-mixing and wet-slurry process are referred to as “dry-mixed” and “slurry-mixed” electrodes, respectively. An argyrodite $\text{Li}_6\text{PS}_5\text{Cl}$ with a Li-ionic conductivity of $3.2 \times 10^{-3} \text{ S cm}^{-1}$ (after exposure to anhydrous xylene, $2.8 \times 10^{-3} \text{ S cm}^{-1}$) at 30 °C (Figure 22), synthesized by solid-state reaction at 550 °C, was used for the electrodes.³⁷ Microstructures of the dry- and slurry-mixed electrodes are illustrated in Figure 20d and e, respectively. For both dry- and slurry-mixed electrodes, SEs make 2D contacts with active materials, providing ionic conduction pathways, while super C65 electronically connects the active materials. However, for slurry-mixed electrodes (Figure 20e), the added polymeric binders would impede ionic conduction by blocking favorable contacts between active materials and SEs.

Figure 23 shows the first-cycle charge/discharge voltage profiles for LiNbO_3 -coated NCM622/Li-In half-cells at 0.1C ($0.17 \text{ mA g}_{\text{NCM622}}^{-1}$) and at 30 °C, varied by weight fraction of SEs and mass loading. The uniform LiNbO_3 coating was confirmed by the field-emission scanning electron microscopy (FESEM) image and the corresponding energy dispersive X-ray spectroscopy (EDXS) elemental maps (Figure 24). The dry- and slurry-mixed electrodes with a given weight fraction of NCM622 (x) with a lower mass loading are referred to as “DxL” and “WxL”, respectively. Detailed specifications for the electrodes are provided in Table 3. The first-cycle discharge capacity values are summarized in Figure 25 and Table 3. Three features should be pointed out in the trends of variation in discharge capacity. First, decreasing the weight fraction of active materials caused increased capacity. For example, the discharge capacity of 130 mA h g^{-1} for the D85L electrode was increased to 152 and 155 mA h g^{-1} for the D80L and D70L electrodes, respectively. The higher fraction of active materials (or the lower fraction of SEs) would lead to poorer contacts between active materials and SEs,^{15, 27, 52, 55} and longer percolation pathways of Li^+ ions in the SE regions.⁵⁵ Both of these imply poor kinetics, which results in low utilization of active materials and poor rate capability. The increased capacities with the higher weight fraction of SEs should be offset by an increased amount of inactive components. In terms of capacity based on the total weight of the electrodes, 80 wt% of active materials showed the highest capacity (Table 3). Second, the electrodes with higher mass loading (28 mg cm^{-2}) showed lower

capacity than those with lower mass loading (20 mg cm^{-2}), which is most critical in the case of the lowest weight fraction of SEs (e.g., 130 mA h g^{-1} for D85L vs. 85 mA h g^{-1} for D85H). In conventional LIB electrodes soaked in LEs, the ionic transport in pores (LE regions) acts as the rate determining step when the electrodes become thicker.¹³³ In this context, the lower capacities of the ASLB electrodes with higher mass loading (or thicker electrodes) could be attributed mostly to Li^+ ion conduction through the SE regions.^{55, 133} This strongly emphasizes the critical need for SEs with high ionic conductivity. Third and most importantly, the slurry-mixed electrodes significantly underperformed the dry-mixed electrodes. Except for the electrodes of D85H and W85H, which exhibited poor capacities, the gap between the discharge capacities of dry- and slurry-mixed electrodes was $18\text{--}35 \text{ mA h g}^{-1}$. The degradation of SE during the wet-slurry process is unlikely because the decrease in conductivity of SE under exposure to anhydrous xylene appeared marginal (Figure 22b). The presence of insulating polymeric binders that partially block contacts between active materials and SEs (illustrated in Figure 20e), could be responsible for the poorer performances of the slurry-mixed electrodes than the dry-mixed electrodes.²⁷ In the cross-sectional FESEM images of the dry-mixed (D85) and slurry-mixed (W85) electrodes and their corresponding elemental maps of Ni, sulfur, and nitrogen (Figure 26), the regions for Ni match with that for nitrogen. This observation would indicate that the surface of NCM622 be covered with the NBR binders, which agrees with the illustration of disruption in ionic pathways by binders in Figure 20e. The rate capabilities of dry- and slurry-mixed electrodes, varied by the weight fraction of active materials and mass loadings, are also shown in Figure 27 and 28. The trends of rate capabilities are well in line with the results of discharge capacities (Figure 23 and 25). It is also noted that the gap between the rate capability of the lower and higher mass-loaded electrodes became larger at higher C-rates.

In an attempt to understand the variations in discharge capacities and rate performances observed, complementary analysis was carried out using field emission scanning electron microscopy (FESEM), electrochemical impedance spectroscopy (EIS), and galvanostatic intermittent titration technique (GITT) measurements. FESEM images of top views of the dry- and slurry-mixed electrodes and their corresponding energy dispersive X-ray spectroscopy (EDXS) elemental maps for sulfur are shown in Figure 29. The elemental maps show more segregated SEs for the electrodes with higher weight fraction of active materials (D85 and W85) and for the slurry-mixed electrodes (W70 and W85), than for the dry-mixed electrodes (D70 and D85). The more segregated SEs indicate poorer ionic percolation, which could explain the capacity of the slurry-mixed electrodes being lower than that of the dry-mixed electrodes and of the electrodes with lower weight fractions of SEs (Figures 23, 25, 27, 28).

Nyquist plots of the dry-mixed and slurry-mixed electrodes in Figure 30 show one depressed semicircle followed by Warburg tail. The numbers were normalized in $\Omega \text{ g}$ because the resistance is

inversely proportional to the surface area of active materials, and thus the mass loading. The intercept values at the x-axis indicate the resistance assigned to the SE layer.²⁶⁻²⁷ The semicircles at high- and mid-frequency range are interpreted as contributions by charge transfer resistance at electrode-SE interfaces and/or electronic contributions of the composite electrodes.²⁶⁻²⁷ The Warburg tail at low frequency stems from Li-ion diffusion in active materials.²⁶⁻²⁷ The EIS spectra were fitted using an equivalent circuit (Figure 31a), and the R2 values, which could result from multiple contributions such as charge transfer resistance and electronic resistance, are plotted in Figure 31b. In line with the results of discharge capacities and rate performances, the resistance was increased by increasing the weight fraction of active materials, by increasing the mass loading, and by adding polymeric binders (for the slurry-mixed electrodes). In particular, it should be noted that the resistance value extracted from the amplitude of the semicircle in the Nyquist plot is an extensive property dependent on the interfacial contact area. Thus, the higher resistance of slurry-mixed electrodes than for dry-mixed electrodes could be explained by unfavorable wetting of SEs onto active materials due to the presence of insulating NBR binders.

The transient discharge voltage profiles from GITT experiments are presented in Figure 32. The corresponding polarization data obtained by subtracting closed-circuit voltage (CCV) from quasi-open-circuit voltage (QOCV) are also plotted, and perfectly agree with the discharge capacities (Figure 23), the rate performances (Figure 27), and the EIS spectra (Figure 30). Importantly, interfacial surface coverage of SEs onto active materials were deduced by analysis using GITT.²⁶⁻²⁷ The dry-mixed electrodes with the highest weight fraction of SEs (D70L or D70H) exhibited the highest surface coverage (25.2%). The low value indicates incompleteness of solid-solid contacts between active materials and SEs. This also might be attributed to micro voids in the inner regions of NCM622 particles, which could not be accessed by the SEs outside¹³⁴⁻¹³⁵ and/or to inaccurate factors used for the governing equation (see Experimental for the details). The electrodes with lower weight fraction of SEs showed much lower surface coverage values than did the electrodes with higher weight fraction of SEs (Table 3). Importantly, the surface coverage values turned out to be far less for the slurry-mixed electrodes than for the dry-mixed electrodes (Table 3). For instance, the surface coverage of 25.2% for the D70 electrode was decreased to 17.5% by adding NBR (for the W70 electrode). This result corroborates that the insulating polymeric binders interrupt direct ionic contacts between SEs and active materials; thereby degrading the electrochemical performance, as illustrated in Figure 20e.

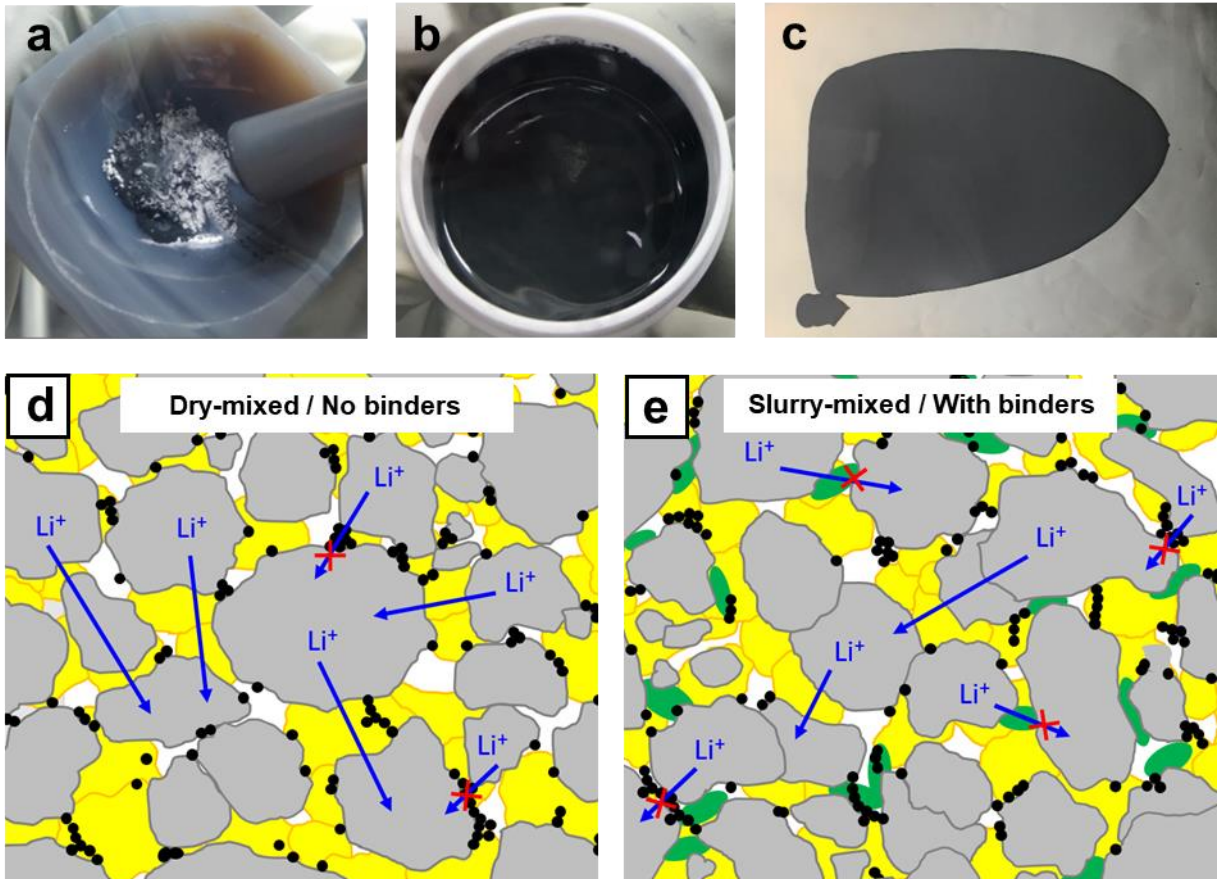


Figure 20. Comparison of all-solid-state lithium-ion battery (ASLB) electrodes fabricated by dry-mixing and wet-slurry processes. Photographs of a) a dry-mixture of active materials, SEs, and super C65 without polymeric binders and b) a slurry comprised of active materials, SEs, super C65, and polymeric binders in xylene. c) Sheet-type NCM622 electrode fabricated by the wet-slurry process. Schematic diagrams representing the microstructures of ASLB electrodes a) by dry-mixing process without binders and b) by wet-slurry process using binders. Active materials, SEs, super P, and polymeric binders (NBR) are shown in gray, yellow, black, and green, respectively.

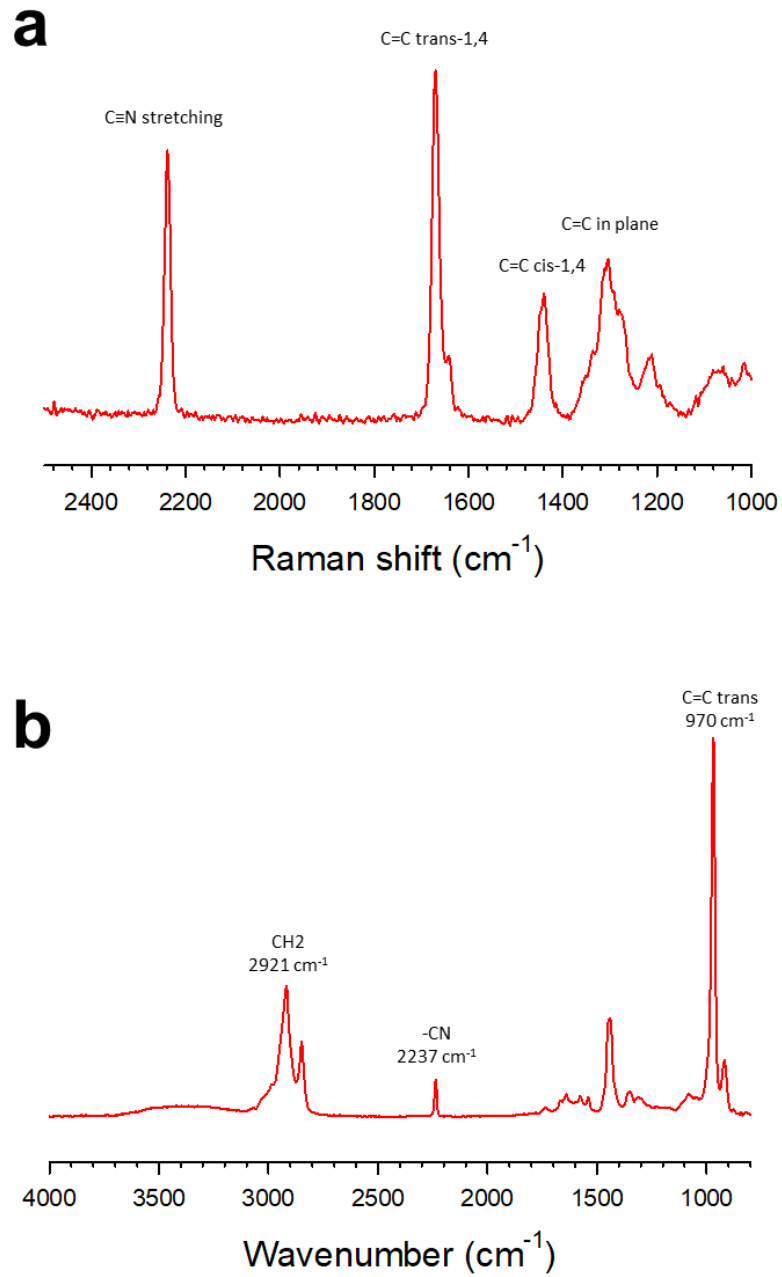


Figure 21. a) Raman and b) FTIR spectra for NBR.

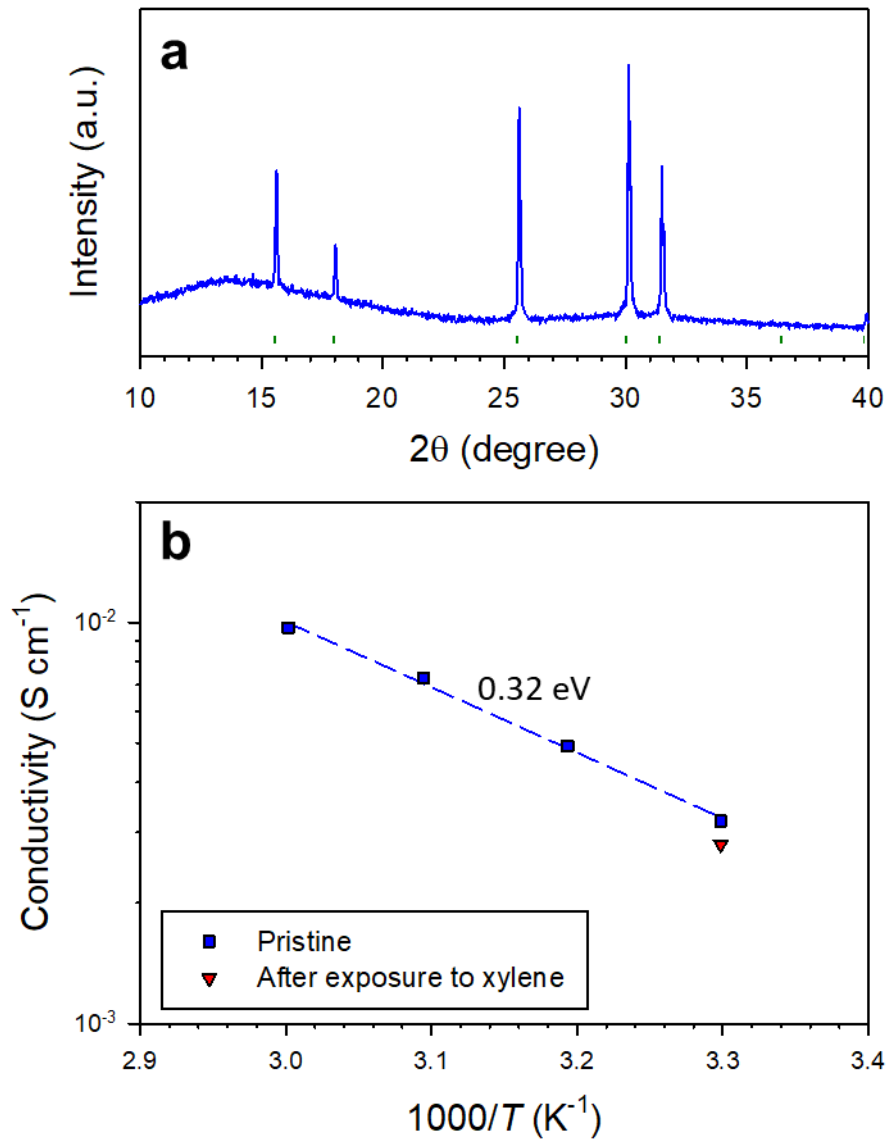


Figure 22. a) XRD pattern and b) Arrhenius plot of Li-ion conductivity for as-prepared $\text{Li}_6\text{PS}_5\text{Cl}$. The Bragg position for argyrodite $\text{Li}_6\text{PS}_5\text{Cl}$ (CIF no. 418490) is shown in a panel a. Conductivity after exposure to anhydrous xylene is also provided in a panel b.

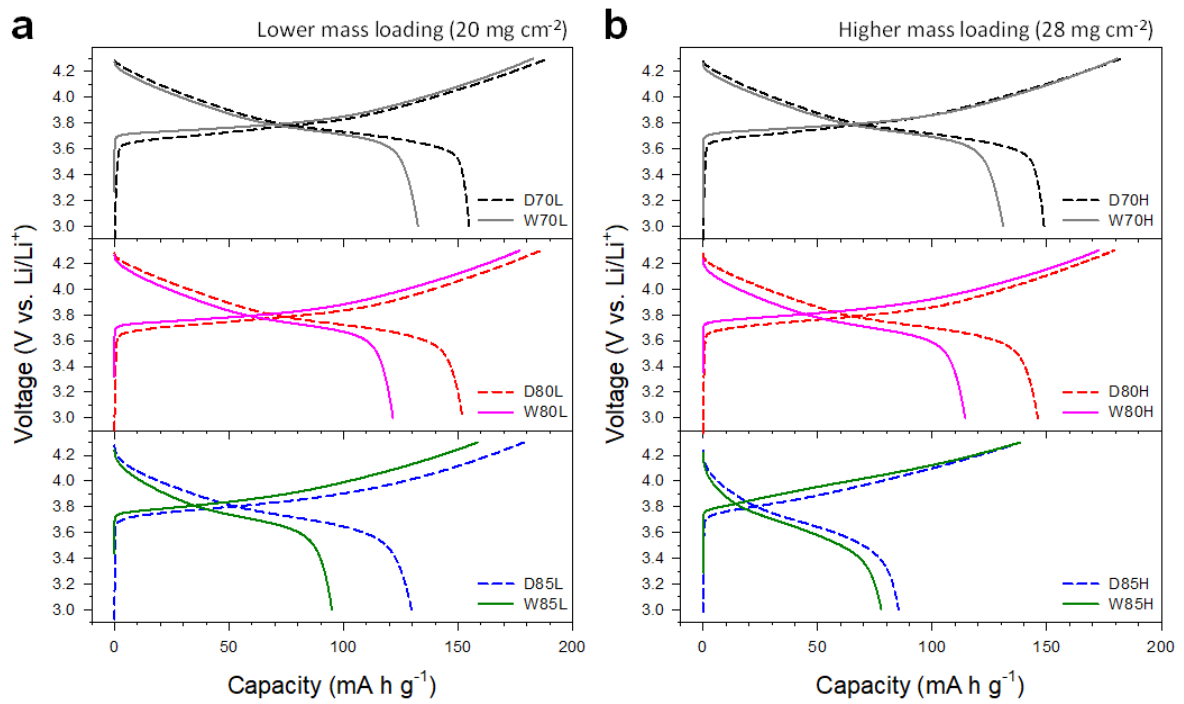


Figure 23. First-cycle charge-discharge voltage profiles at 0.1C and 30 °C for all-solid-state NCM622/Li-In half-cells employing dry- and slurry-mixed electrodes with a) the lower mass loading and b) the higher mass loading of NCM622.

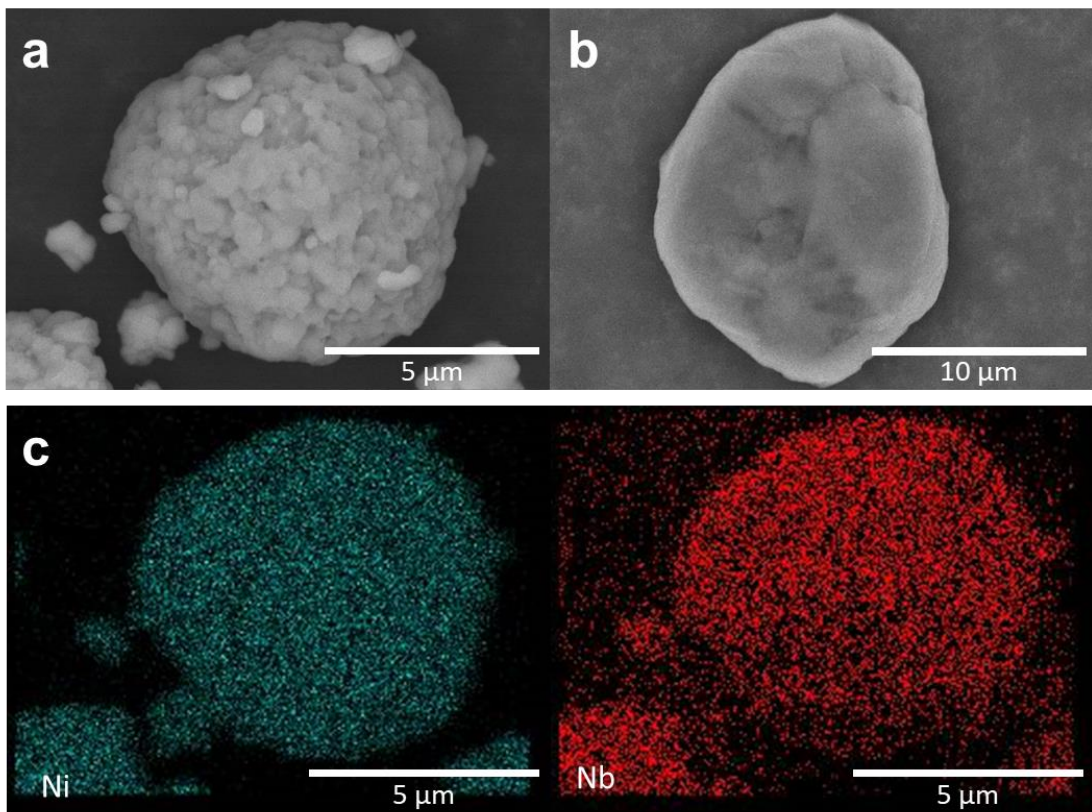


Figure 24. FESEM images of a) NCM622 and b) graphite. c) The EDXS elemental maps of Ni and Nb for NCM622, which correspond with (a).

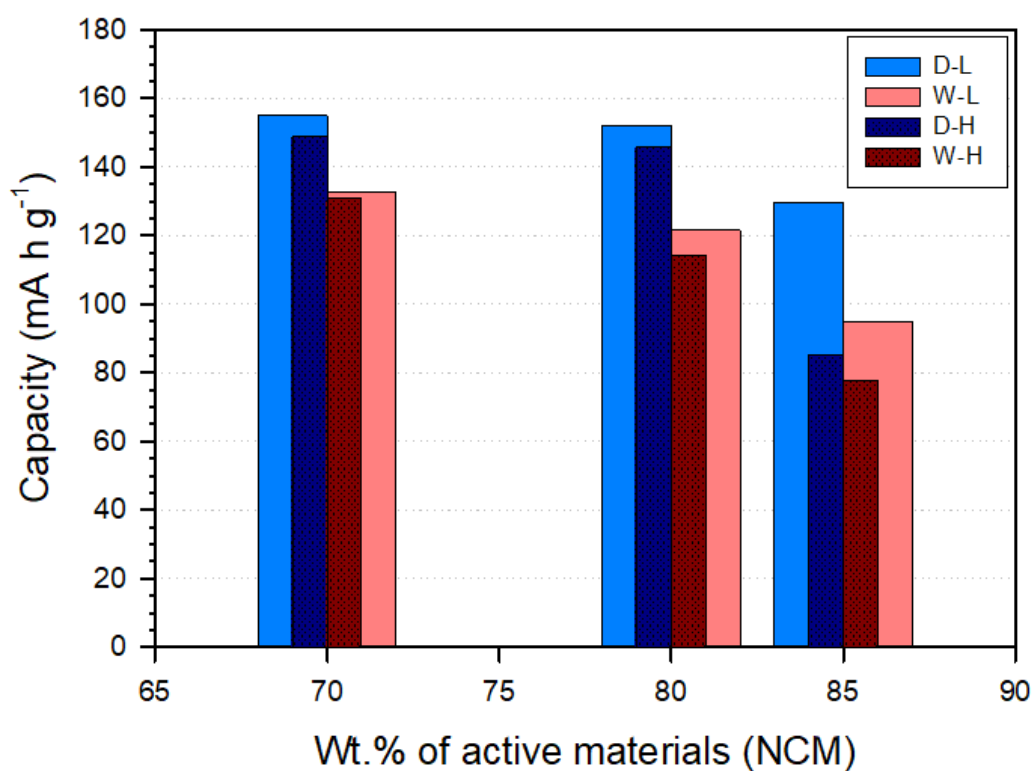


Figure 25. First-cycle discharge capacity for the dry- and slurry-mixed NCM622 electrodes as a function of weight fraction of active materials. The NCM622/Li-In all-solid-state half-cells were cycled between 3.0-4.3 V (vs. Li/Li⁺) at 0.1C and 30 °C. The data were plotted from those in Figure 23.

Table 3. Characteristics of dry- and slurry-mixed NCM622 electrodes for ASLBs.

Process	Sample name	Composition ^{a)}	Q _{0.1C} ^{b)}		R [Ω g]	Surface coverage of SEs onto active materials [%]
			[mA h g _{NCM} ⁻¹]	[mA h g _{electrode} ⁻¹]		
Dry- mixing	D70L	69.1 / 29.6 / 1.3 / 0	155	107	0.18	25.2
	D70H		149	103	0.23	
	D80L	79.2 / 19.5 / 1.3 / 0	152	120	0.19	15.4
	D80H		146	116	0.28	
	D85L	84.3 / 14.4 / 1.3 / 0	130	109	0.26	12.9
	D85H		85	72	0.41	
Wet- slurry	W70L	68.1 / 29.2 / 1.3 / 1.4	133	90	0.29	17.5
	W70H		131	89	0.50	
	W80L	78.1 / 19.2 / 1.3 / 1.4	122	95	0.81	14.0
	W80H		114	89	1.22	
	W85L	83.1 / 14.2 / 1.3 / 1.4	95	79	0.92	5.8
	W85H		78	65	1.37	
	Premixed W85L		127	106	0.44	

^{a)} weight ratio of active material to SE to Super P to NBR; ^{b)} The first-cycle discharge capacity at 0.1C

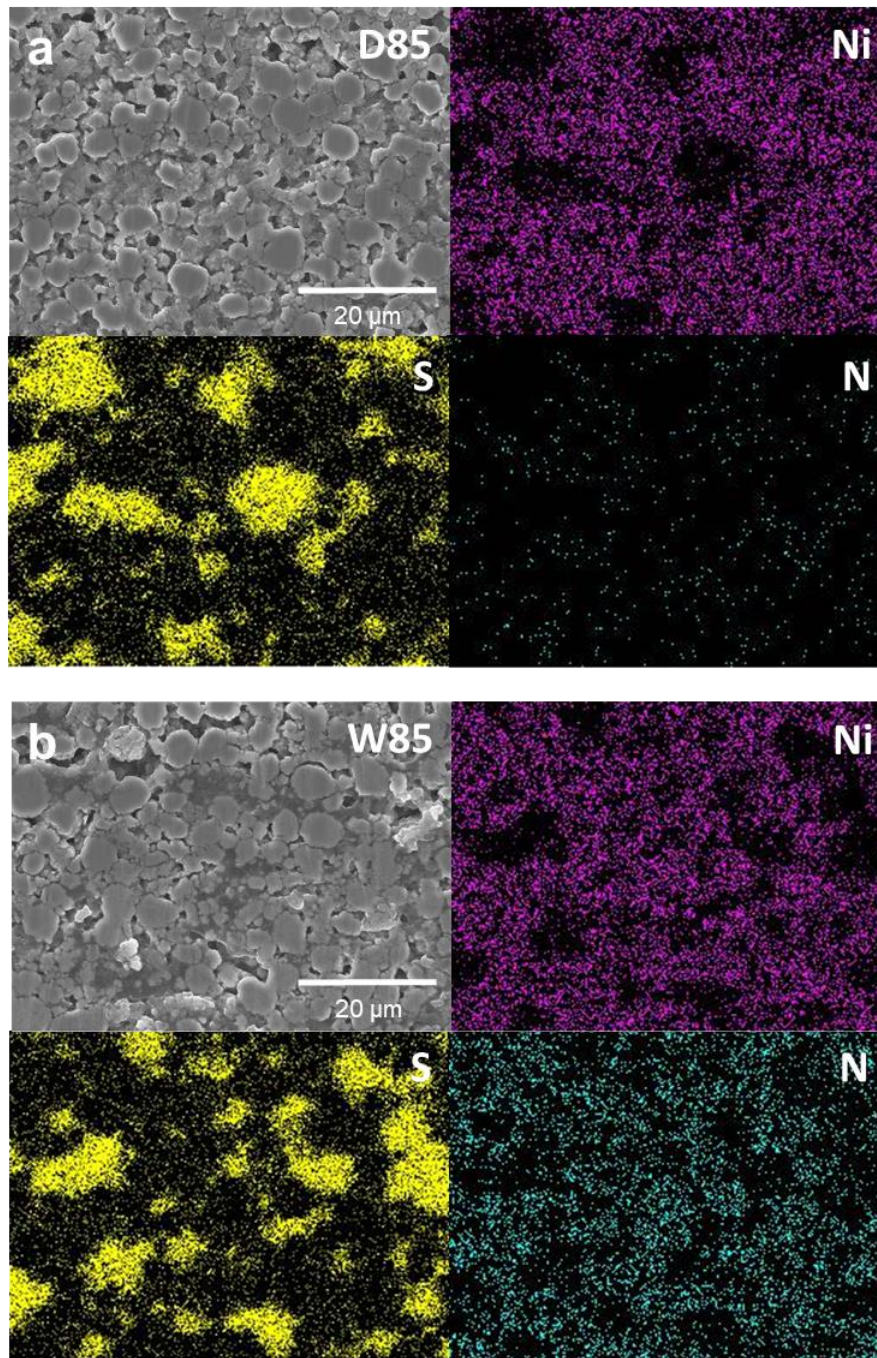


Figure 26. Cross-section FESEM images of a) dry- and b) slurry-mixed electrode with 85 wt.% of active materials and their corresponding EDXS elemental maps for Ni, sulfur, and nitrogen.

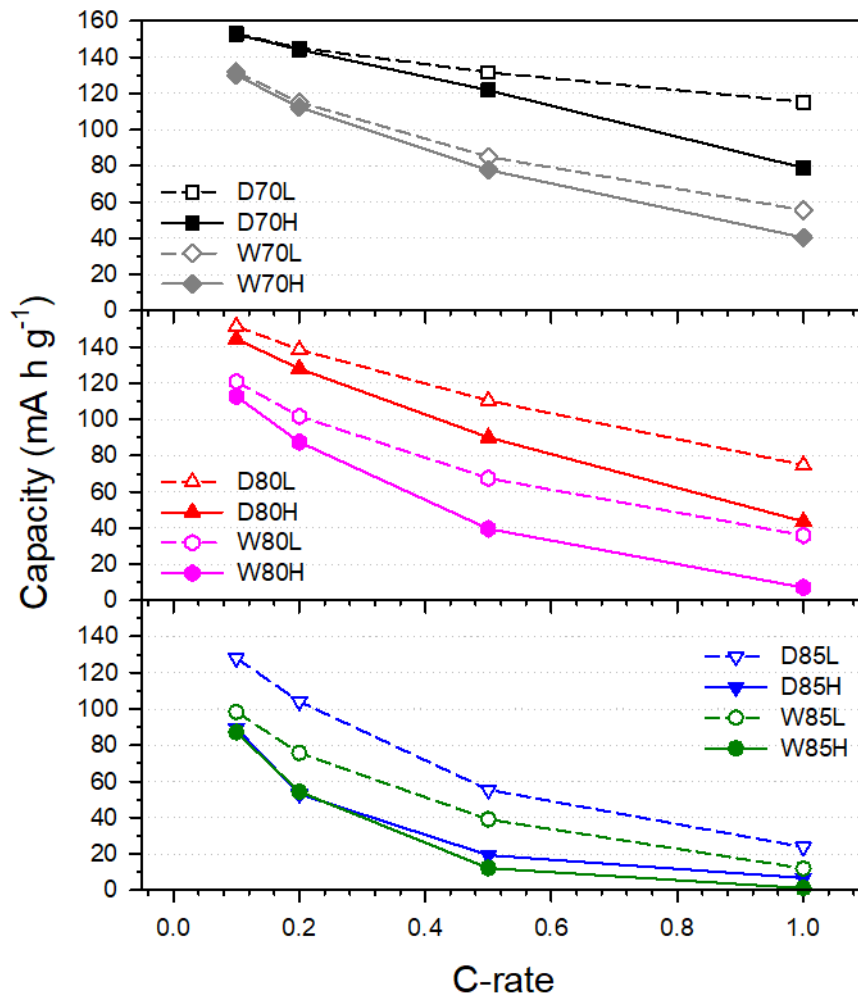


Figure 27. Discharge capacities for all-solid-state NCM622/Li-In half-cells cycled between 3.0-4.3 V (vs. Li/Li⁺) varied by C-rates at 30 °C. The C-rates for charge and discharge were the same.

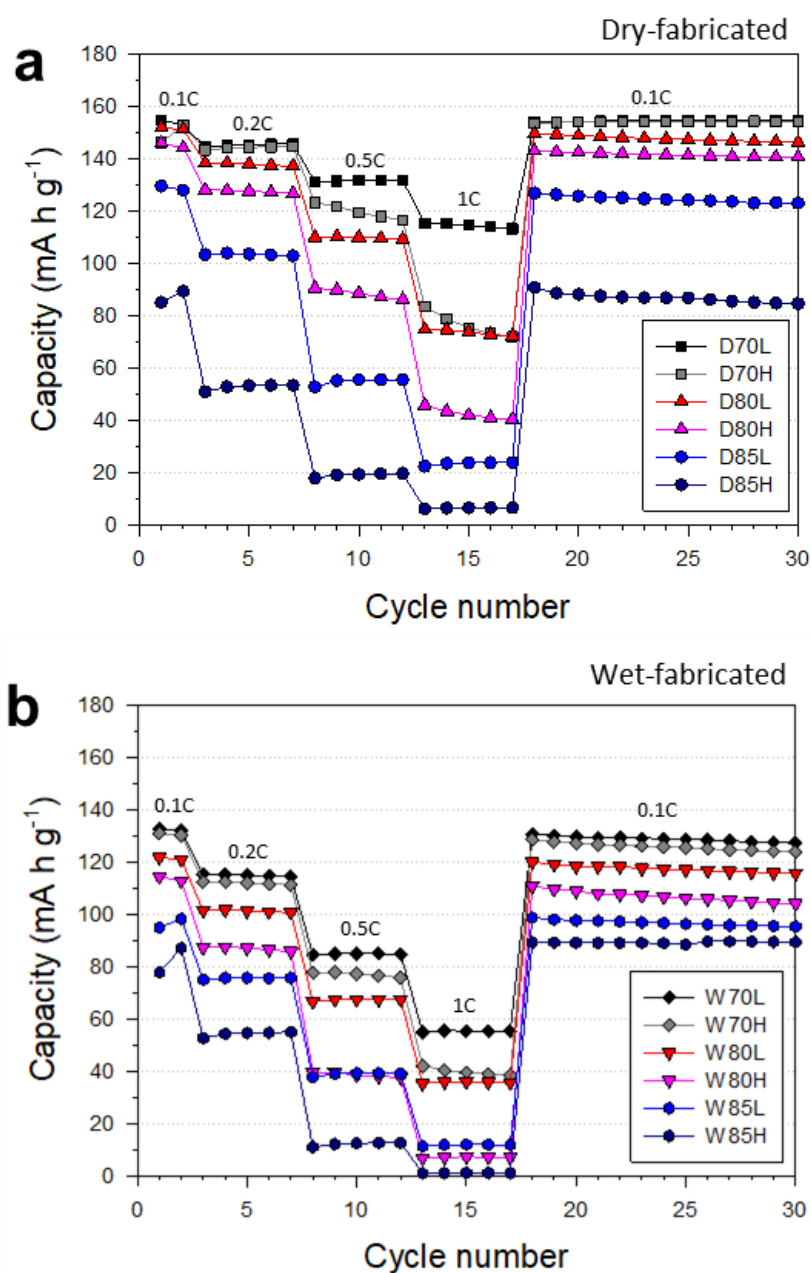


Figure 28. Discharge capacities as a function of cycle number varied by different C-rates for the NCM622 electrodes fabricated by a) dry-mixing and b) wet-slurry processes. The NCM622/Li-In all-solid-state half-cells were cycled between 3.0-4.3 V (vs. Li/Li⁺) at 30 °C.

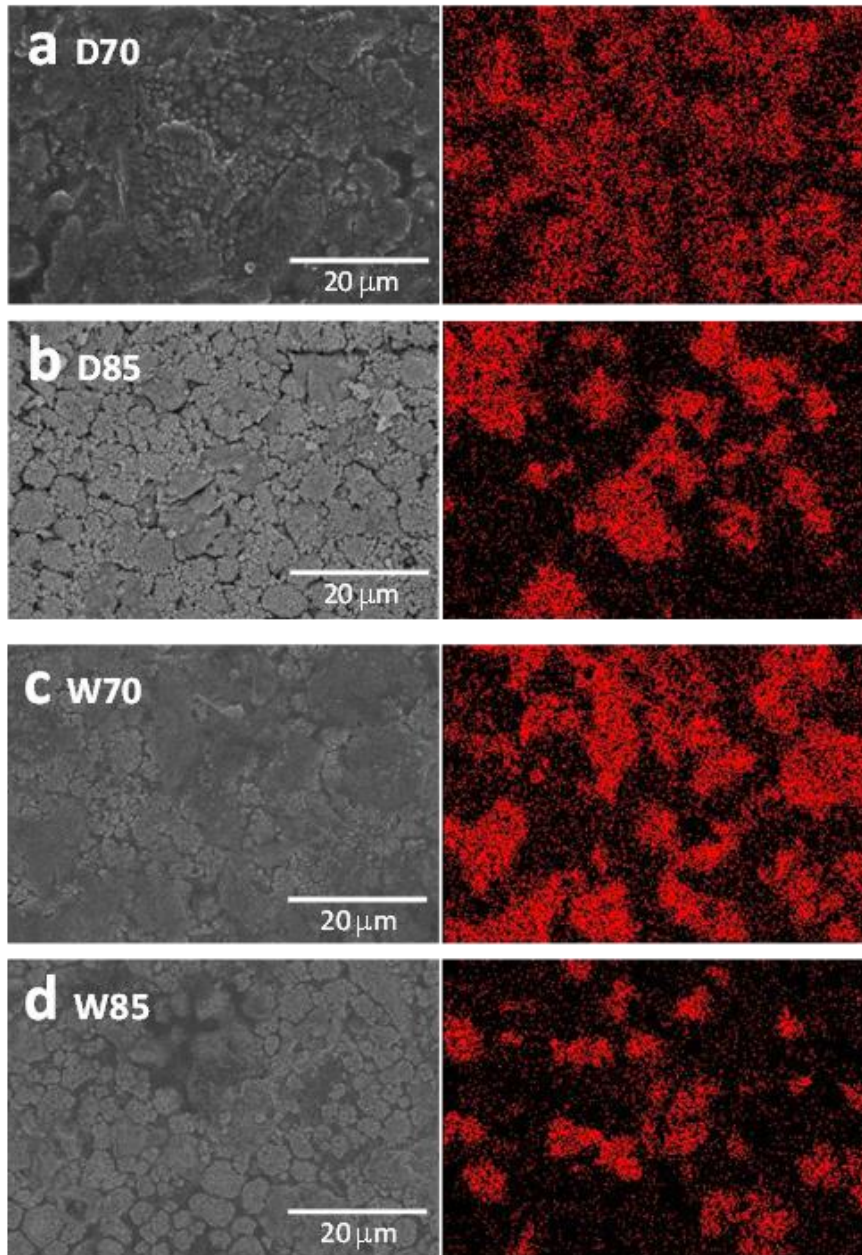


Figure 29. FESEM surface images of NCM622 electrodes fabricated by dry-mixing process with a) ~70 wt.% (D70) and b) ~85 wt% of NCM622 (D85) and wet-slurry process using NBR with c) ~70 wt.% (W70) and d) ~85 wt.% (W85) of NCM622. Their corresponding EDXS elemental maps for sulfur are also shown.

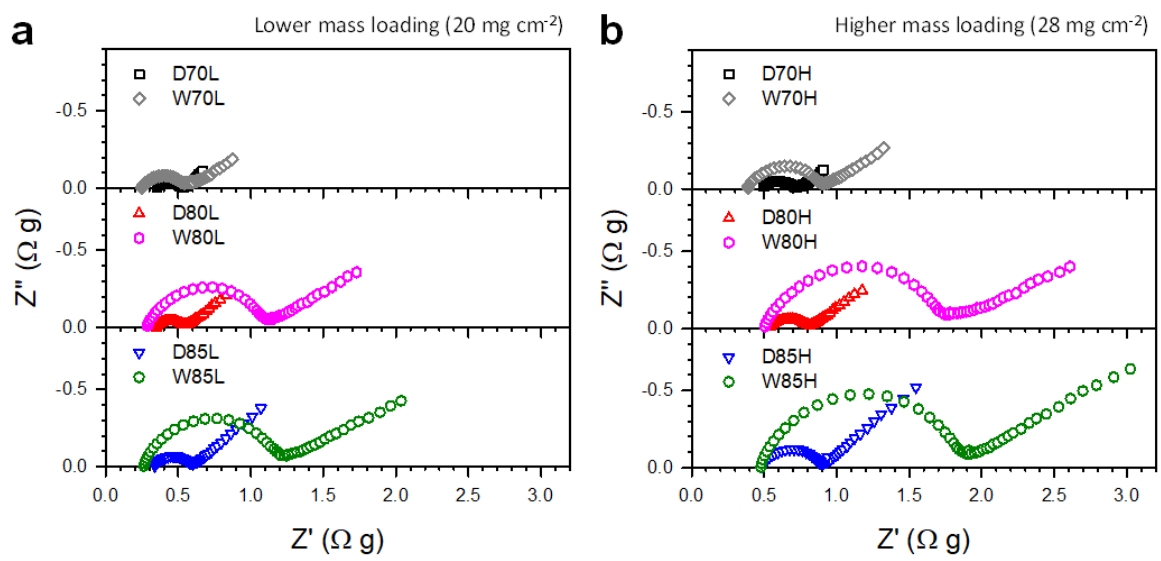


Figure 30. Nyquist plots at 30 °C for all-solid-state NCM622/Li-In half-cells employing dry- and slurry-mixed electrodes with a) the lower mass loading and b) the higher mass loading.

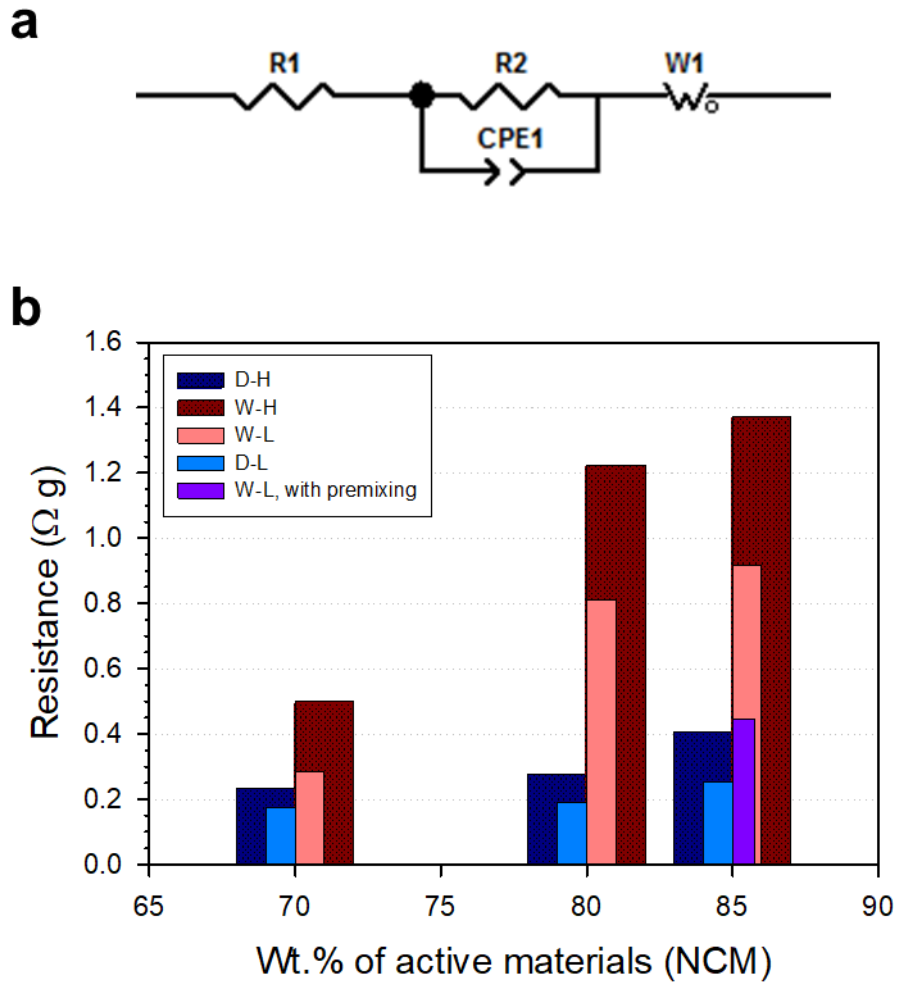


Figure 31. a) Equivalent circuit model for NCM622/Li-In all-solid-state half-cells. b) Resistance values (R_2 in a panel a) as a function of weight fraction of active materials for the dry- and slurry-mixed NCM622 electrodes. The data were obtained from Nyquist plots in Figure 30.

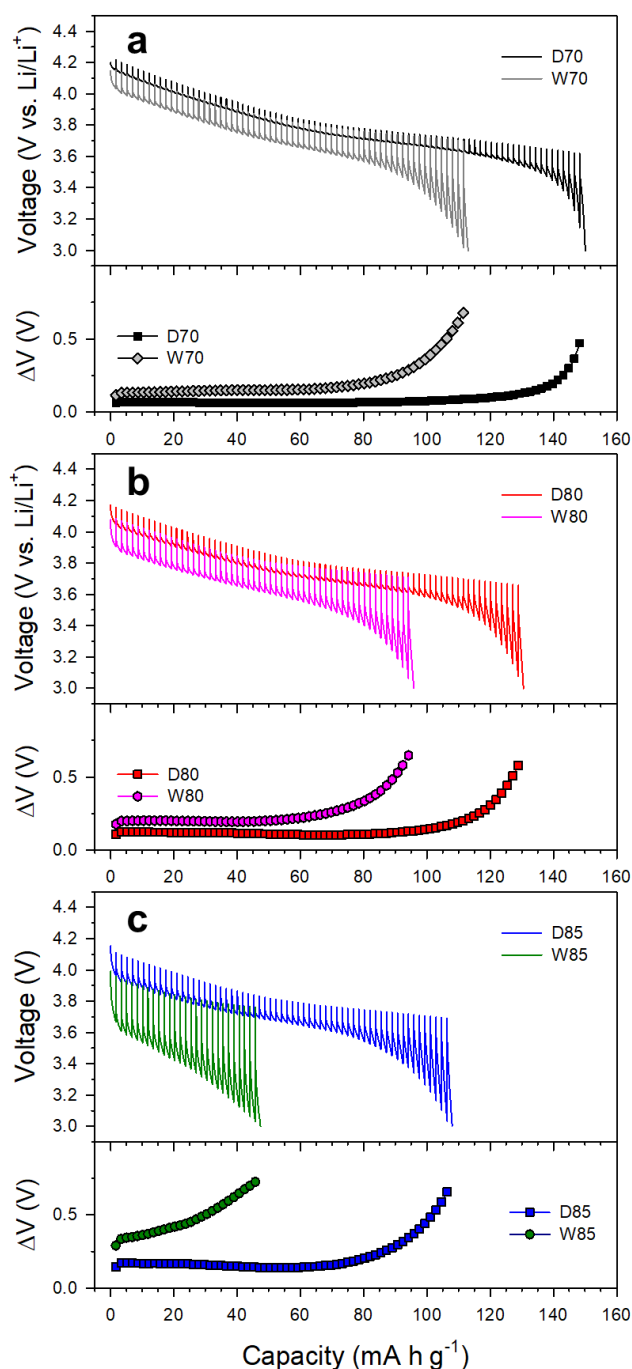


Figure 32. Transient discharge voltage profiles at 30 °C and their corresponding polarization (ΔV) curves for all-solid-state NCM622/Li-In half-cells employing dry- and slurry-mixed electrodes with a) ~70 wt.%, b) ~80 wt.%, and c) ~85 wt.% NCM622, obtained by GITT. The enlarged view where QOCV and CCV are indicated is shown in the inset in a. The polarization data were plotted by subtracting CCV from QOCV in the transient voltage profiles in transient discharge voltage profiles.

4.1.2.2. Electrodes Fabricated by Premixing Process

From the systematic and complementary analysis results in the previous section, it is evident that solid-solid ionic contacts between active materials and SEs become poorer when lower amount of SEs are used and/or when polymeric binders are included in the ASLB composite electrodes, which is necessary for practical ASLB with high energy density. In this regard, premixing of active materials (NCM622) and SEs by ball-milling in a dry condition prior to wet-slurry fabrication was attempted to ensure favorable ionic contacts without hindrance by polymeric binders, as illustrated in Figure 33a. After premixing, the characteristic XRD peaks for NCM622 and argyrodite $\text{Li}_6\text{PS}_5\text{Cl}$ remained intact, indicating negligible chemical interaction between active materials and SEs (Figure 33b).

The slurry-mixed electrode with the lowest amount of SE (W85L) was chosen to examine the effect of premixing on electrochemical performances. FESEM images of cross-sectioned views of the W85L electrode fabricated with and without premixing, and their corresponding EDXS elemental maps for sulfur (green) and Ni (red) are compared in Figure 33c. The signals of sulfur are more homogeneous and overlapped more with the regions for Ni signals for a premixed electrode than for a conventional one, implying closer contacts between active materials and SEs in the former.

The electrochemical performance of the W85L electrodes with and without premixing, are compared in Figure 34. The first-cycle discharge capacity was significantly increased by premixing: from 92 to 129 mA h g^{-1} . This improvement of the electrochemical performance by premixing is in line with the decreased amplitude of the semicircle by approximately half in the Nyquist plot (Figure 34b, Table 3) and the significantly decreased polarization for the premixed electrodes in the GITT result (Figure 34c). Importantly, the dramatic increase of surface coverage of SEs onto NCM622 by premixing (from 5.8% to 9.4%) was also confirmed. These results emphasize the beneficial effect of premixing on utilization of active materials in terms of favorable ionic contacts. Unfortunately, at higher C-rates of 0.5C or 1C, the improvement from premixing appeared marginal (Figure 35). It is speculated that the ionic conductivity of SEs must be considerably more improved to achieve better high-rate performance. Damage to SEs by mechanical impacts during the premixing process also cannot be ruled out to explain the unsatisfactory high-rate capability of a premixed electrode.

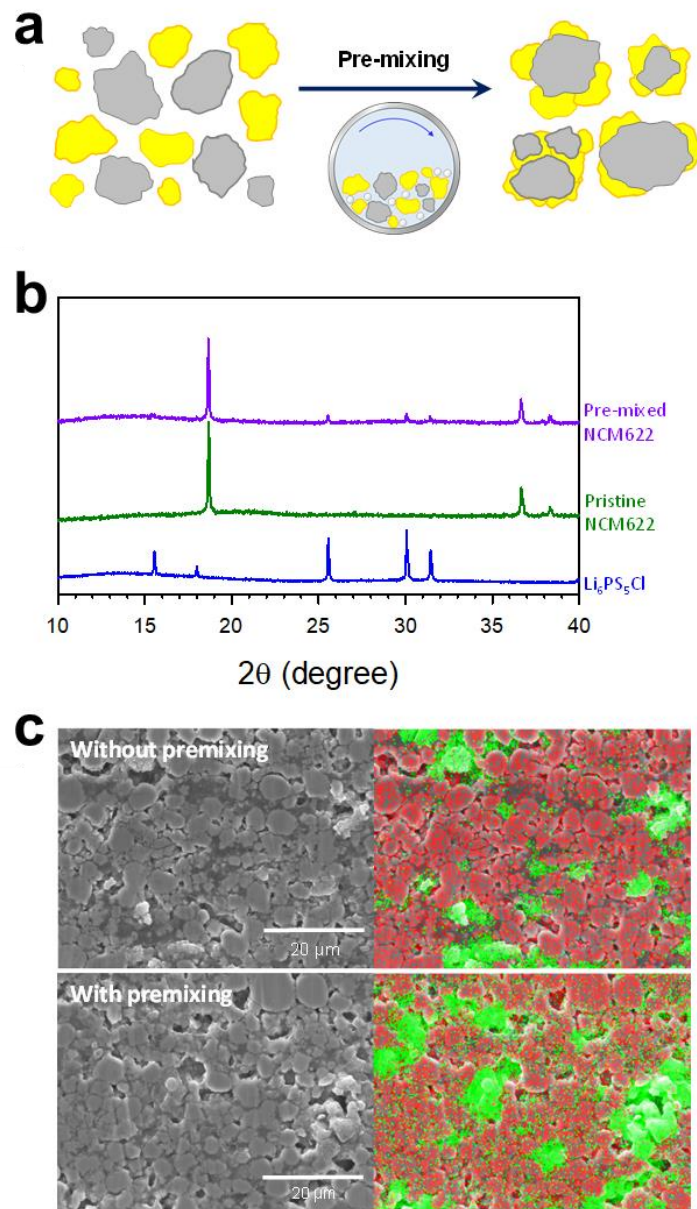


Figure 33. Results of NCM622 electrodes fabricated by wet-slurry process using a premixed powder of NCM622 and SEs. a) Schematic diagram of premixing process for NCM622 and SE powders by mechanical milling. b) XRD patterns of $\text{Li}_6\text{PS}_5\text{Cl}$, pristine NCM622, and NCM622 premixed with $\text{Li}_6\text{PS}_5\text{Cl}$. c) Cross-sectional FESEM images of wet-mixed NCM622 electrodes without and with premixing process and their corresponding EDXS elemental maps for Ni (red) and sulfur (green).

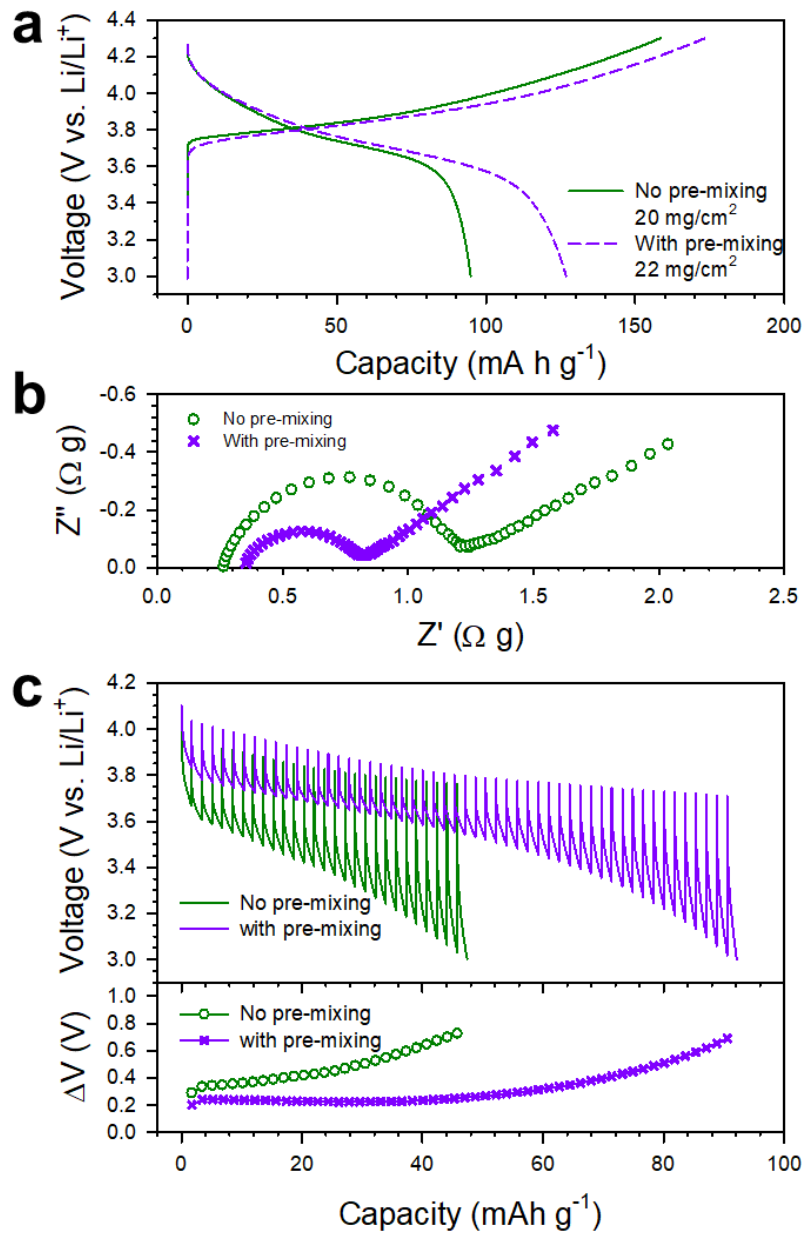


Figure 34. Electrochemical performances of NCM622 electrodes fabricated by wet-slurry process using a premixed powder of NCM622 and SEs. a) First-cycle charge-discharge voltage profiles at 0.1C, b) Nyquist plots, and c) transient discharge voltage profiles and their corresponding polarization (ΔV) curves for slurry-mixed NCM622 electrodes without and with premixing process, and their corresponding polarization curves.

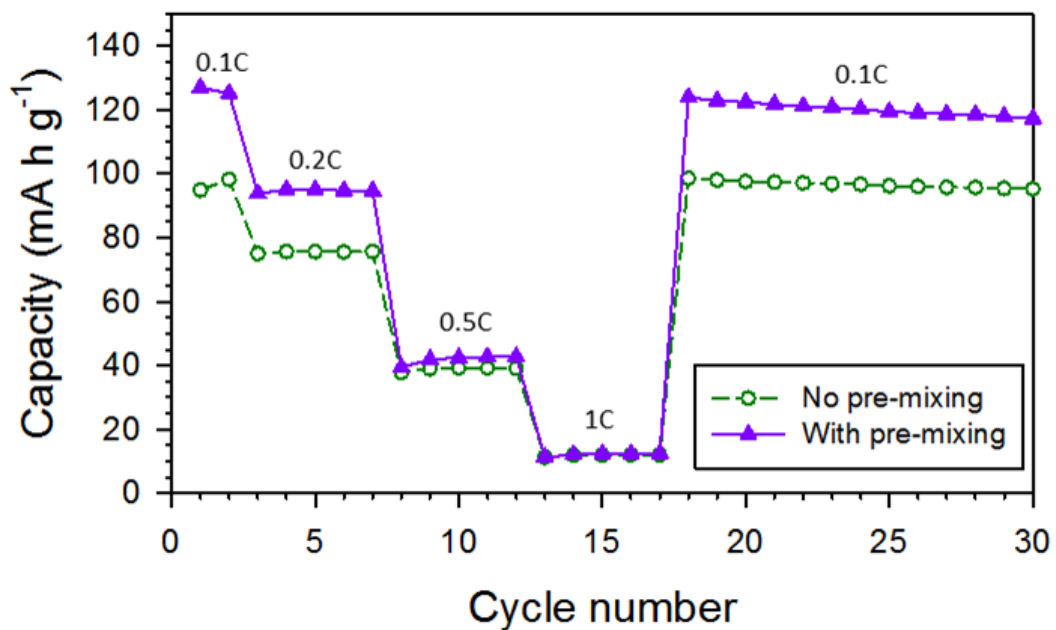


Figure 35. Discharge capacities as a function of cycle number varied by different C-rates for the NCM622 electrodes fabricated by wet-slurry process without and with pre-mixing. The NCM622/Li-In all-solid-state half-cells were cycled between 3.0-4.3 V (vs. Li/Li⁺) at 30 °C.

4.1.2.3. Practical All-Solid-State NCM622/Gr Full-Cells

NCM622/graphite ASLBs were fabricated using the slurry-mixed electrodes. For the full-cell, the slurry-mixed graphite electrode showing the first-cycle discharge capacity of 330 mA h g^{-1} at 0.025C and $30 \text{ }^\circ\text{C}$ was used (Figure 36). SE layers were coated on the graphite electrodes by wet-slurry process before combining with the NCM622 electrodes. Two types of full-cells were fabricated: a conventional pelletized cell and an $80 \times 60 \text{ mm}^2$ pouch-type cell (Figure 37a). The detailed specifications for the NCM622/graphite full-cells are presented in Table 2. Figure 37b shows their first-cycle charge-discharge profiles for the pelletized and pouch-type NCM622/graphite full-cells at 0.025C at $25 \text{ }^\circ\text{C}$ and $30 \text{ }^\circ\text{C}$, respectively. The first-cycle discharge capacities for the pelletized and pouch-type NCM622/graphite full-cells were 121 and $112 \text{ mA h g}_{\text{NCM622 electrode}}^{-1}$, respectively, which translates into 190 and 184 W h kg^{-1} based on total weight of the electrodes (active materials, SEs, carbon additives, polymeric binders, and current collectors). In turn, the volumetric energy density of the pouch-type full-cell is calculated to be 432 W h L^{-1} . The NCM622/graphite full-cell also showed a stable cycling performance at 0.025C (the inset in Figure 37b).

The safety performance of the pouch-type NCM622/graphite full-cell was assessed by simple tests. First, a pouch-cell that was fully charged to 4.3 V at 0.025C was cut with scissors. As shown in Figure 8c, the cut pouch-cell remained working and illuminated a white light emitting diode (LED) without any noticeable events indicating a need for safety concerns. This result indicates that the SE layers are mechanically robust, and able to avoid short-circuits between positive and negative electrodes after cutting. It also shows that they are thermally stable against the Joule-heat generated by the instant short current while being cut.¹³⁶ In the second test, a fully charged pouch-cell was subjected to heating at $111 \text{ }^\circ\text{C}$ on a hot plate for $> 1 \text{ h}$. It also remained intact and illuminated the white LED (Figure 8d). This is in contrast to swelling and irreversible damage for the conventional LIBs based on LEs.^{12, 136} The temperature of $111 \text{ }^\circ\text{C}$ for the experiment was set based on the limited thermal stability of the pouch materials. Even higher temperature than $111 \text{ }^\circ\text{C}$ might not cause serious effects on the electrochemical and safety performance of the ASLB.^{15, 27} Although more sophisticated and elaborate experiments are required to make a fairer evaluation of safety performance in terms of quantitative analysis, to our knowledge, our results are the first demonstration of the excellent safety of pouch- and bulk-type ASLBs based on sulfide SEs.

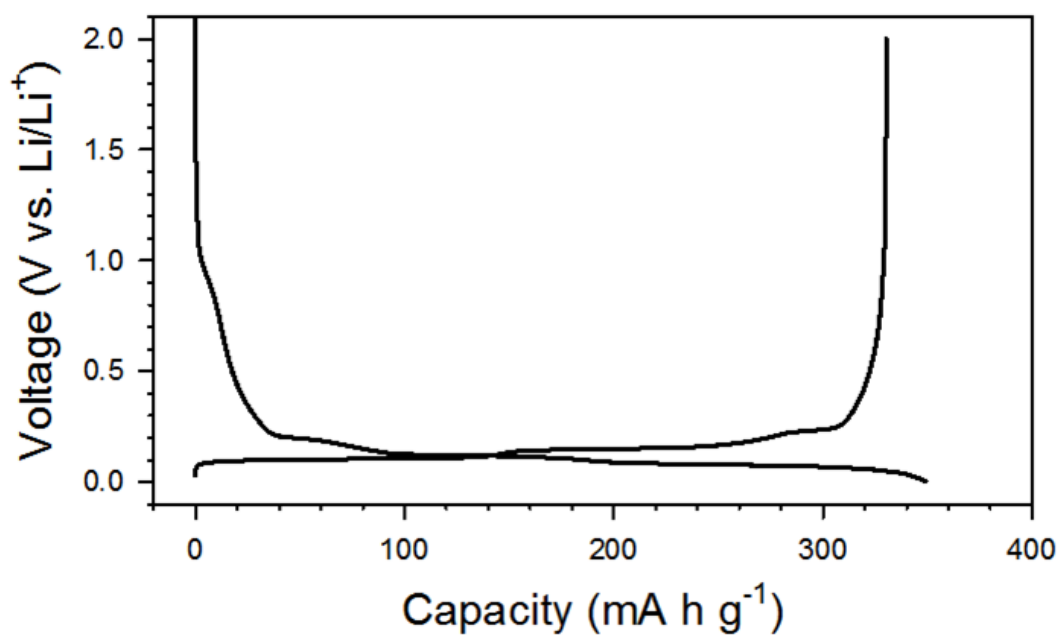


Figure 36. First-cycle charge-discharge voltage profiles for the wet-slurry fabricated graphite electrode at 0.025C and 30 °C. The composition of graphite, SE, and NBR was 58.6:39.1:2.3 weight ratio. The mass loading of the graphite electrode was 18 mg cm⁻².

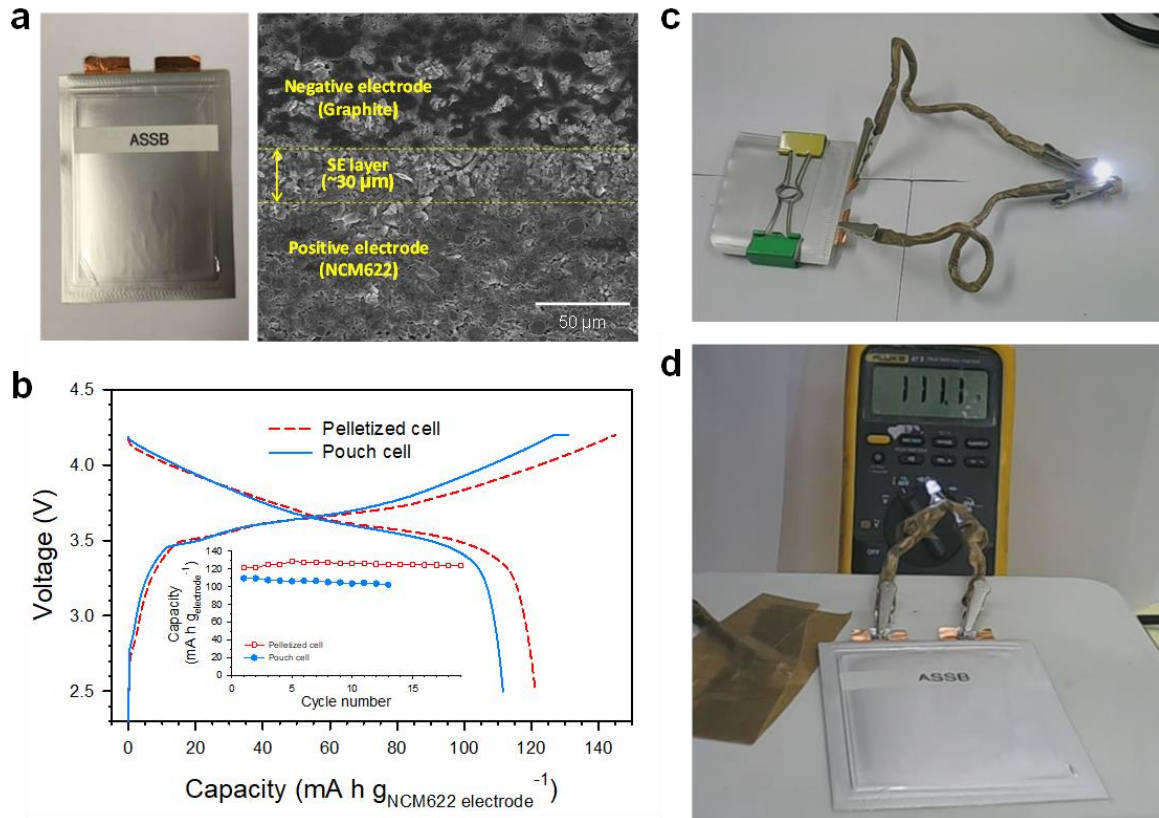


Figure 37. Results of NCM622/graphite all-solid-state full-cells. a) Photograph of $80 \times 60 \text{ mm}^2$ pouch-type NCM622/graphite full-cell and its cross-sectional FESEM image. b) First-cycle charge-discharge voltage profiles of pelletized and pouch-type full-cells of NCM622/graphite at 0.025C . The pelletized cell and pouch-cell were tested at $30 \text{ }^\circ\text{C}$ and $25 \text{ }^\circ\text{C}$, respectively. The detailed specifications are provided in Table 4. Photographs of $80 \times 60 \text{ mm}^2$ pouch-type NCM622/graphite all-solid-state full-cells c) after cutting with scissors and d) being placed on the hot plate at $111 \text{ }^\circ\text{C}$ for $> 1 \text{ h}$.

Table 4. Characteristics of NCM622/graphite all-solid-state full-cells.

Cell type		Composition ^{a)}	Mass loading [mg cm ⁻²]	Thickness [μm]	Energy density ^{b)}
Pelletized cell	Positive electrode	79.2 / 19.5 / 1.3 / 0	37	155	190 W h kg ⁻¹ [c] 202 W h kg ⁻¹ [d]
	SE layer	0 / 98.5 / 0 / 1.5	7.5	45	
	Negative electrode	58.6 / 39.1 / 0 / 2.3	27	138	
Pouch-cell (80 × 60 mm ²)	Positive electrode	68.1 / 29.2 / 1.3 / 1.4	21	88	184 W h kg ⁻¹ 432 W h L ⁻¹ (405 mA h)
	SE layer	0 / 98.5 / 0 / 1.5	4.9	30	
	Negative electrode	58.6 / 39.1 / 0 / 2.3	13	65	
Pouch-cell (88 × 53 mm ²) in previous work ^{e)}	Positive electrode	59 / 34 / 5 / 2	35	250	89 W h kg ⁻¹ [f] 139 W h L ⁻¹ [f] (125 mA h)
	SE layer	0 / 98 / 0 / 2	32.6 ^[f]	200	
	Negative electrode	95 / 0 / 0 / 5	14	100	

^{a)} weight ratio of active material to SE to Super P to NBR; ^{b)} based on total weights of the electrodes, SE layers, and current collectors; ^{c)} for upper cut-off voltage of 4.2 V; ^{d)} for upper cut-off voltage of 4.3 V; ^{e)} from previous result; ^{f)} Estimated values based on the data in the previous result

4.2. Diagnostic study for Sheet-Type All-Solid-State Lithium-Ion Batteries

4.2.1. All-Solid-State Three-Electrode Cell

Reliable electrochemical test protocols are a prerequisite in R&D for advanced materials and devices for batteries. Li metal is routinely used as a counter electrode (CE) and simultaneously as a reference electrode (RE) in the half-cells for conventional LIBs because of its constant voltage even at high current densities. However, interpretation of the performances of working electrodes (WEs) is hindered by Li metal electrodes in some cases, such as where the usage of Li metal is heavy in terms of number of cycles or apparent capacity,⁹⁵⁻⁹⁶ and/or where complicated chemistry results in too thick passivation layers on Li metal.⁹⁴⁻⁹⁵ Contrary to the anticipated compatibility of SEs with Li metal, recent reports on this matter unveiled serious challenges: not only a deteriorating chemical reaction of SEs with Li metal, dependent on the composition of the SEs,⁵⁵ but also the penetrating growth of Li metal into the defects of SE structures.^{97-99, 137} This must be the reason why In or Li-In, not Li metal, has been mostly used as the counter and reference electrode in the half-cells for ASLBs. Since the reaction of In with Li⁺ ions proceeds via a two-phase reaction ($\text{In} + \text{Li}^+ + e^- \rightarrow \text{LiIn}$) with a flat voltage plateau at 0.62 V (vs. Li/Li⁺),¹¹⁴ it serves as a good RE. However, its significant contribution to the kinetic behavior of all-solid-state half-cells has not been evaluated yet, deterring reliable interpretation of WEs. In a previous study regarding the impedance analysis of LiCoO₂/In all-solid-state cells, it was observed that interfacial resistance at the low-frequency region, which was assigned to the In-SE interfacial one, became huge at the end of discharge.¹³⁸ In particular, the reliability of In or Li-In as counter and reference electrodes in all-solid-state half-cells must be carefully evaluated when alternative electrode materials (e.g., Sn, Si, S) are tested because their capacities far exceed the usage ranges of the CEs for the cases using conventional electrode materials (e.g., LiCoO₂, graphite (Gr)).

In this regard, development of reliable all-solid-state three-electrode cells that allow deconvolution of the signals for positive and negative electrodes is imperative. Three-electrode cells using LEs are fabricated by placing REs in between positive and negative electrodes¹³⁹ or close to the side edge of sandwiched positive and negative electrodes (Swagelok cell).¹⁴⁰ For thin-film-type ASLBs fabricated by vacuum deposition, few reports about three-electrode cells using Li metal as RE are found.¹⁴¹ Unfortunately, the unique fabrication protocol for bulk-type all-solid-state cells, which is based on cold-pressing under high pressures (hundreds of MPa) and the use of pelletizing mold, makes the design of bulk-type all-solid-state three-electrode cells extremely challenging. Moreover, while $\geq 500\text{-}\mu\text{m}$ -thick SE separating layers have been frequently used for conventional tests of bulk-type ASLBs, from a practical perspective, the thickness must be reduced to tens of micrometer. This strictly restricts application of the conventional design for LE-based three-electrode cells to all-solid-state three-electrode cells.

In this part, a novel bulk-type all-solid-state three-electrode cell with a configuration of

RE/SE/WE/SE/CE, which allows precise separation of voltages for positive and negative electrodes despite using thin (tens of micrometers) SE layers, was demonstrated. The first instance of Sn/Li-In half-cells shows that the overall capacity is limited by the Li-In CEs, not by the Sn WEs, which is solved by the use of Li-In-SE CEs. The second instance involves $\text{LiNi}_{0.6}\text{Co}_{0.2}\text{Mn}_{0.2}\text{O}_2$ (NCM)/Gr full-cells assembled using sheet-type electrodes and thin (50–60 μm) SE layers by the scalable wet-slurry method. Soft ISCs by penetrating growth of Li metal into the SE layers during charge at high C-rates are evidenced. The unique durability of the all-solid-state full-cells upon discharge to 0 V is also analyzed.

4.2.1.1. Reliable Electrochemical Test Protocols for All-Solid-State Half-Cells (Sn/Li-In)

Sn could be a suitable negative electrode material to achieve high energy density for ASLBs because of its high theoretical capacity (992 mA h g^{-1}), metallic properties, and ductility, which allows intimate contact with SEs by simple cold-pressing.¹¹⁵⁻¹¹⁸ However, we found that the capacity of Sn in Sn/Li-In half-cells is unexpectedly low and strongly dependent on the loading amount (Figure 38); the first-cycle lithiation (or discharge) capacity of $534 \text{ mA h g}_{\text{Sn}}^{-1}$ for $4 \text{ mg}_{\text{electrode}} \text{ cm}^{-2}$ decreases to only $307 \text{ mA h g}_{\text{Sn}}^{-1}$ for $10 \text{ mg}_{\text{electrode}} \text{ cm}^{-2}$. These values are far smaller than that for the conventional Sn/Li half-cells using LEs ($958 \text{ mA h g}_{\text{Sn}}^{-1}$, Figure 39). Note that an excessive amount of Li-In (nominal composition of $\text{Li}_{0.5}\text{In}$) was employed for CEs to accommodate the full lithiation-delithiation of Sn WEs (see Experimental Section for details). Interestingly, the overall capacity difference in all-solid-state Sn/Li-In cells for discharge originates mainly from the capacities in the voltage region below 0.5 V (vs. Li/Li^+) while the capacities in the two-plateau regions above 0.5 V (vs. Li/Li^+) ($180\text{-}220 \text{ mA h g}_{\text{Sn}}^{-1}$) are similar to that for the Sn/Li half-cell using LEs (at the second cycle). This observation led us to suspect that the overall capacity may be more affected by Li-In CEs than by Sn WEs.

The first design of an all-solid-state three-electrode cell (referred to as ‘cell-1’) is illustrated in Figure 3a, in which the RE is in contact with the side of SE layer. Unfortunately, this design requires too thick (at least 1 mm thick) SE layers. This problem was solved by contacting the RE on the backside of the WE through an additional SE layer as illustrated in Figure 3b (referred to as ‘cell-2’). The discharge-charge voltage profiles of Sn ($4 \text{ mg}_{\text{electrode}} \text{ cm}^{-2}$)/Li-In half-cells for cell-1 and cell-2 at different current densities are shown in Figure 40c. Cell-1 shows lower capacity and poorer rate capability than cell-2. This is attributed to the higher resistance of the thicker SE layer in cell-1 (2.2 mm) as compared with cell-2 ($730 \mu\text{m}$). Figure 40d presents the separated discharge-charge voltage profiles at 0.045 mA cm^{-2} for Sn WEs and Li-In CEs vs. Li/Li^+ (WE/RE and CE/RE, respectively) as well as the ones for Sn WEs with respect to Li-In CEs (WE/CE). As suspected, the overall discharge is ended by termination of Li-In CEs, not Sn WEs. Although the discharge cut-off voltage for Sn/Li-In cells was set to be 0 V vs. Li/Li^+ (or -0.62 V for WE with respect to CE), in reality the terminal voltages for Sn electrodes are much higher than 0 V vs. Li/Li^+ (0.43 and 0.36 V vs. Li/Li^+ for cell-1 and cell-2, respectively) because of early termination of discharge by Li-In CEs. This result clearly indicates that the unexpectedly low capacities of all-solid-state Sn/Li-In half-cells (Figure 38) come from poor capacity or kinetics of Li-In CEs, not Sn WEs. It is confirmed that, when using Li-In RE, calibration of voltages for WE and CE in the scale of vs. Li/Li^+ by adding 0.62 V shows a marginal difference, compared with the case when using Li metal RE (Figure 41).

Following the afore-learned lesson, we attempted to enhance the usage of Li-In CEs by percolating with SE powders. All-solid-state half-cells for Sn ($10 \text{ mg}_{\text{electrode}} \text{ cm}^{-2}$), using three different CEs by varying the weight fraction of SE ($0, 10, \text{ and } 20 \text{ wt.}\%$ which corresponds with approximately

0, 26, 44 vol.%, respectively), were fabricated. Their discharge-charge voltage profiles at different current densities are compared in Figure 42a. The discharge capacity at 0.11 mA cm^{-2} is dramatically increased to $652 \text{ mA h g}_{\text{Sn}}^{-1}$ with 10 wt.% SE in the CE, and reaches $689 \text{ mA h g}_{\text{Sn}}^{-1}$ with 20 wt.% SE, which approaches the value for the LE-cell ($958 \text{ mA h g}_{\text{Sn}}^{-1}$, Figure S39). The enhancement in capacity at higher current densities is more dramatic with 20 wt.% SEs than with 10 wt.% SEs. The separated discharge-charge voltage profiles at 0.11 mA cm^{-2} for Sn WEs and Li-In(-SE) CEs vs. Li/Li⁺ in Figure 42b undoubtedly reveal that lithiation (or discharge) of Sn WEs close to 0 V (vs. Li/Li⁺) is enabled by the use of Li-In-SE CEs. Also, the dramatic decrease in termination voltage from 1.07 V (vs. Li/Li⁺) for the SE-free Li-In CE to 0.72 and 0.71 V (vs. Li/Li⁺) for the Li-In-SE CEs with 10 and 20 wt.% SE, respectively, reflects the extended usage of Li-In by the percolated SEs. The terminal voltages of Li-In or Li-In-SE CEs, varied by current densities, are plotted in Figure 42c (the full voltage profiles at various current densities are provided in Figure 43). Consistently, increasing amounts of SE in CEs (20 wt.% SE) result in lower terminal voltages, especially at higher current densities.

After the all-solid-state Sn/Li-In and Sn/Li-In-SE (20 wt.% SE) half-cells were fully discharged down to -0.62 V (corresponding to the targeting cut-off voltage of 0 V vs. Li/Li⁺ for Sn WE), the disassembled CEs were subjected to analysis using time-of-flight secondary ion mass spectrometry (TOF-SIMS). Cross-sectional field emission scanning electron microscopy (FESEM) images and their corresponding energy dispersive X-ray spectroscopy (EDXS) elemental maps for the CEs are provided. (Figure 44) The concentration distribution of Li⁺ ions in the cross-sectioned SE-free Li-In and Li-In-SE CEs are shown in Figure 45a, b, respectively. The thickness of the Li-depleted layer is estimated to be $\sim 50 \mu\text{m}$ for the Li-In CE (Figure 45a). In stark contrast, for the Li-In-SE CE, the Li-depleted or deficient signals are distributed in much deeper regions. From this observation, schematic diagrams for cross-sectional views of Li-In and Li-In-SE CEs are illustrated in Figure 45c, d, respectively. For the Li-In CE, upon discharge of Sn/Li-In half-cells, the Li-depleted indium layer is formed at the top of the CE, impeding further movement of Li⁺ ions from the inner regions of Li-In to the SE layer, which results in early termination of the cells. In contrast, for Li-In-SE CEs, utilization of Li⁺ ions from much deeper regions of CEs could be facilitated by the aid of percolated SEs. In short, apart from our success in developing the first reliable bulk-type all-solid-state three-electrode cells, the development of Li-In-SE CEs provides a reliable test protocol for all-solid-state half-cells that is much less affected by high-capacity WEs and high current density.

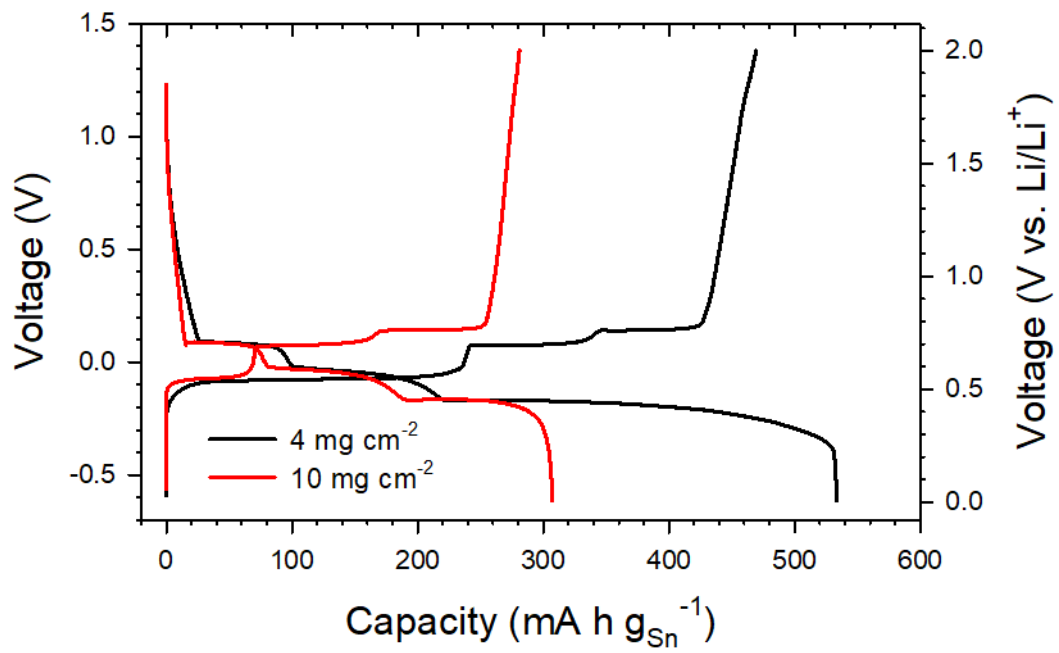


Figure 38. First-cycle discharge-charge voltage profiles for Sn/Li-In all-solid-state cells with two different electrode mass loadings.

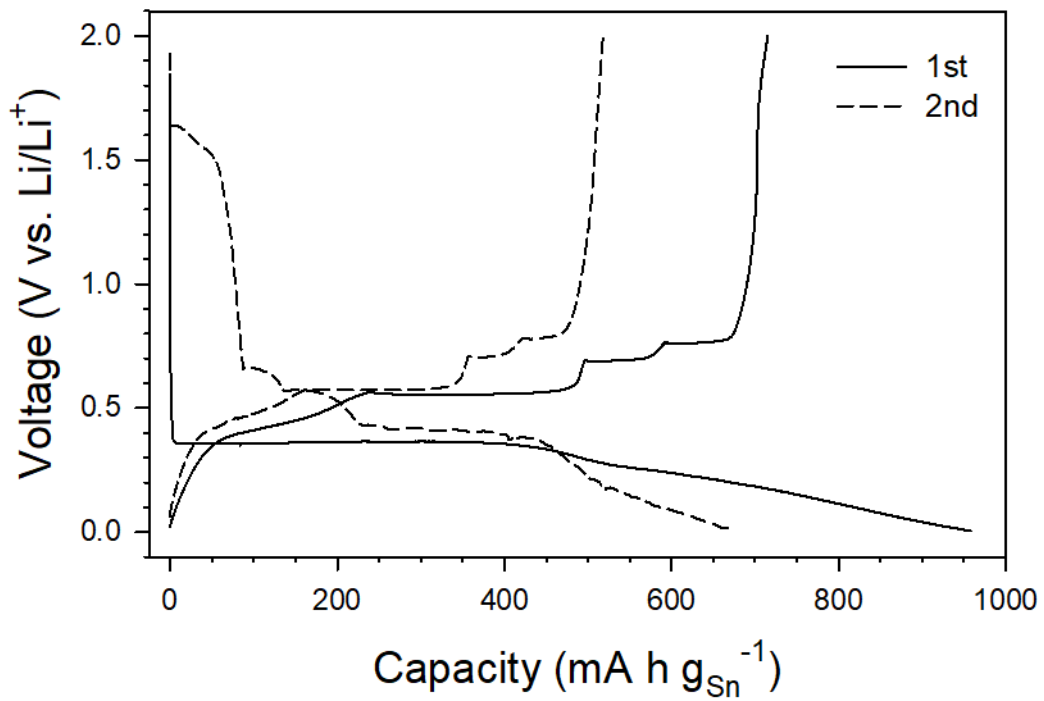


Figure 39. First two-cycle discharge-charge voltage profiles Sn/Li cells using liquid electrolytes at 0.054 and 0.27 mA cm⁻² at the first and second cycle, respectively.

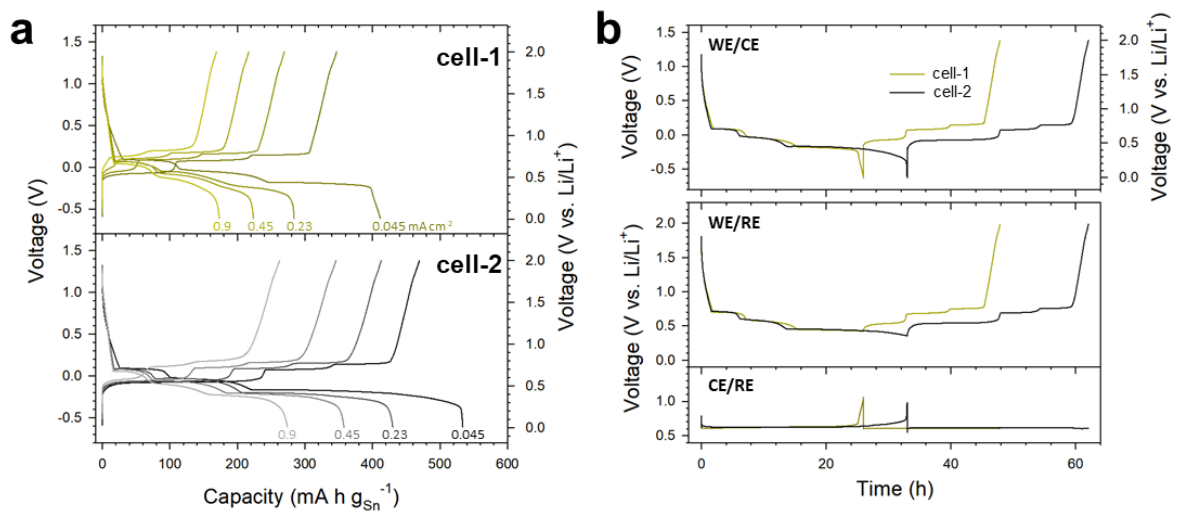


Figure 40. Results for two different types of all-solid-state three-electrode cells. Schematics of all-solid-state three-electrode cells are shown in Figure 3a) type 1 (referred to as “cell-1”) and b) type 2 (referred to as “cell-2”). a) Discharge-charge voltage profiles for Sn/Li-In all-solid-state three-electrode cells at different current densities. b) Discharge-charge voltage profiles of each electrode for Sn/Li-In all-solid-state three-electrode cells at 0.045 mA cm^{-2} .

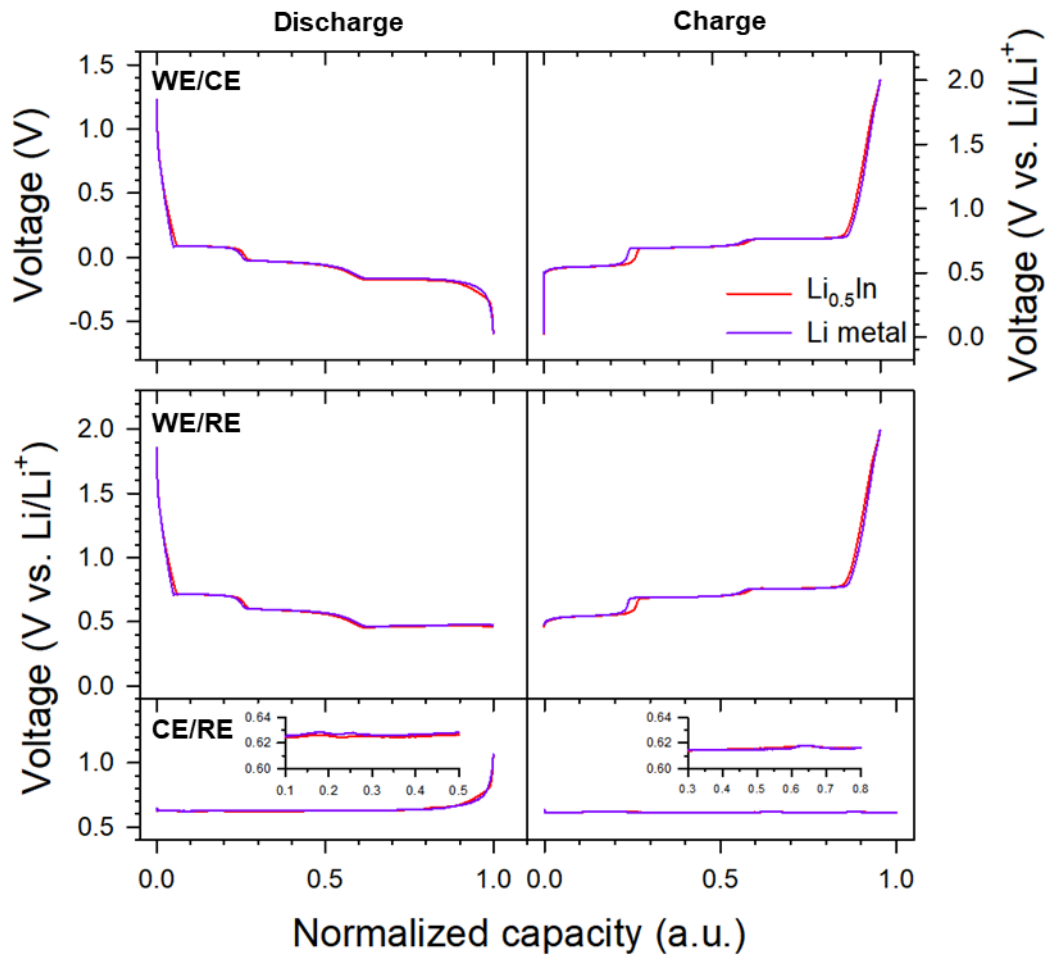


Figure 41. Comparison of the discharge-charge voltage profiles of each electrode for Sn/Li-In all-solid-state three-electrode cells using $\text{Li}_{0.5}\text{In}$ or Li metal as REs.

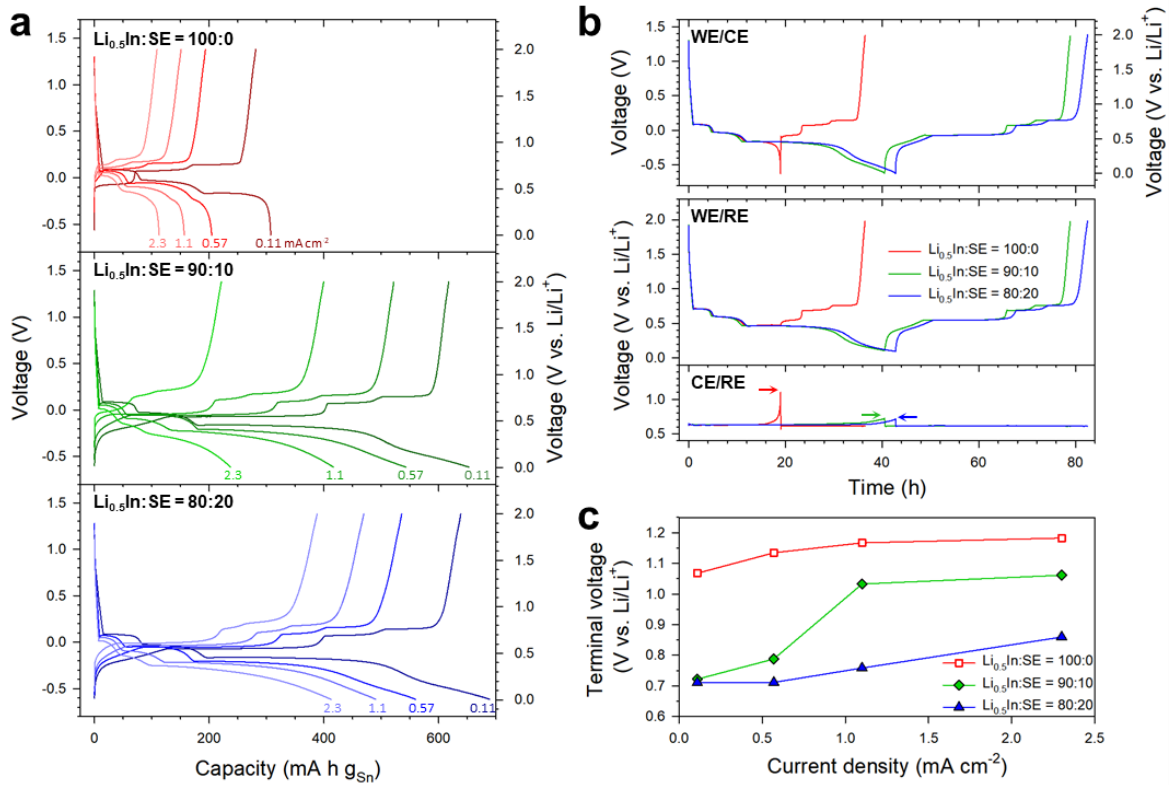


Figure 42. Electrochemical results for Sn/Li-In(-SE) all-solid-state three-electrode cells with different CEs (counter electrodes). a) Discharge-charge voltage profiles (WE vs. CE) for the cells with different CEs where three different weight ratios of $\text{Li}_{0.5}\text{In}/\text{SE}$ were used. The numbers indicate the current density in mA cm^{-2} . b) Discharge-charge voltage profiles for each electrode at 0.11 mA cm^{-2} . The arrows indicate the terminal voltage of CEs ($\text{Li}_{0.5}\text{In}$ or $\text{Li}_{0.5}\text{In-SE}$) upon discharge (delithiation for CEs). c) Terminal voltage for CEs ($\text{Li}_{0.5}\text{In}$ or $\text{Li}_{0.5}\text{In-SE}$) upon discharge (delithiation for CEs) as a function of current density, which is plotted from the data in (b) and Figure 43.

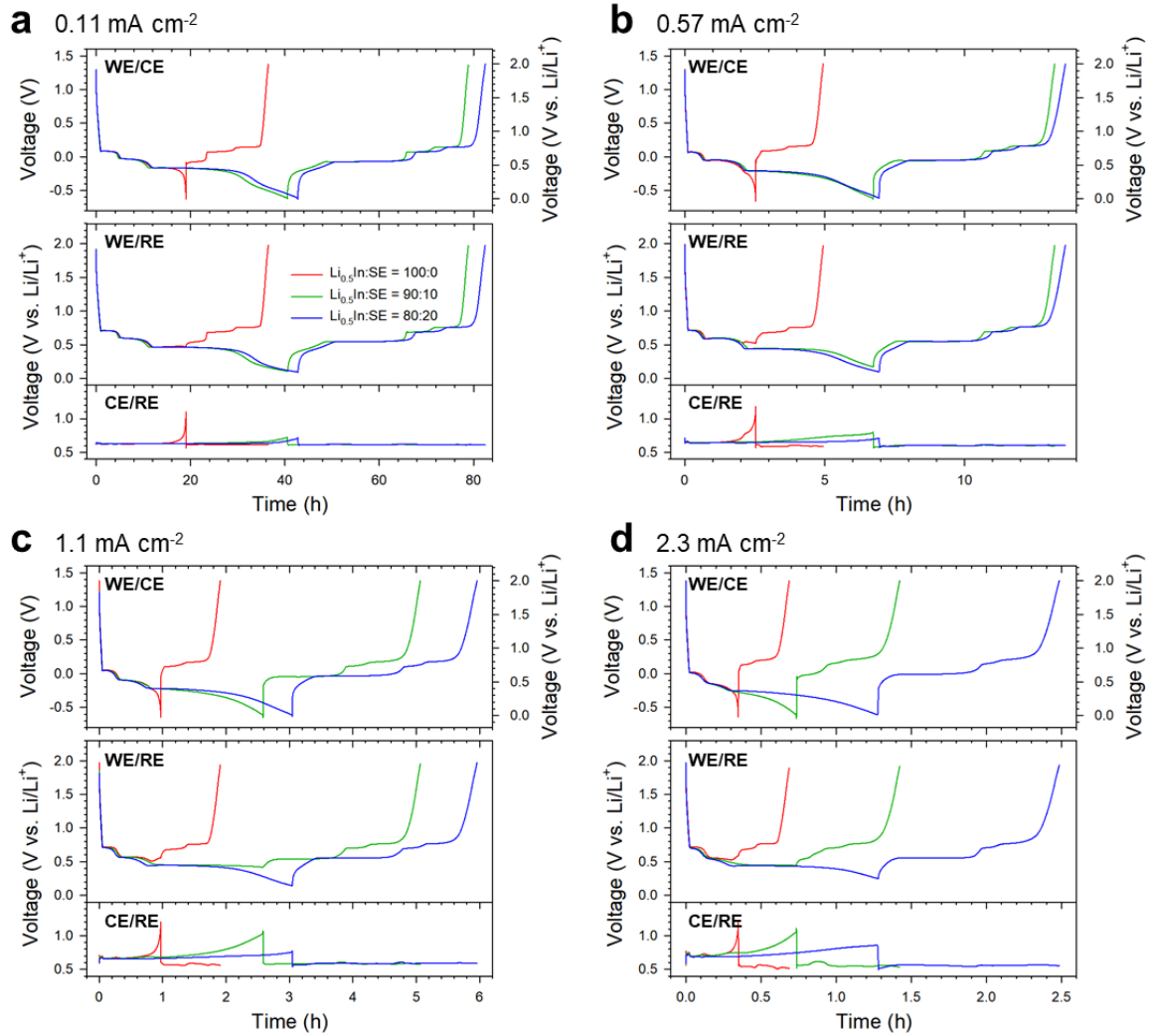


Figure 43. Discharge-charge voltage profiles of each electrode for Sn/Li-In all-solid-state three-electrodes with different CEs using three different weight ratios of $\text{Li}_{0.5}\text{In}/\text{SE}$. The results of cycling at four different current densities are shown. Figure 42b corresponds with (a).

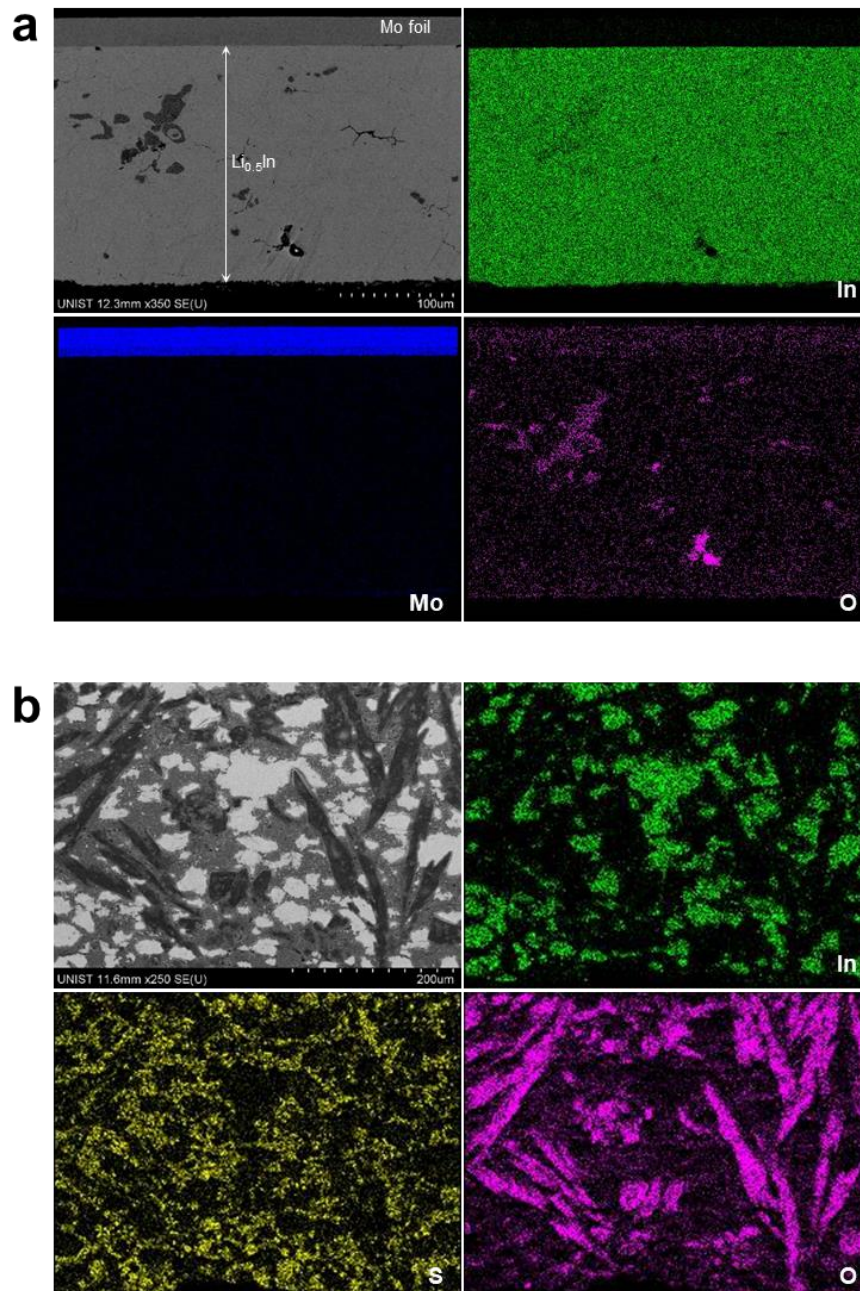


Figure 44. Cross-sectional FESEM images for a) $\text{Li}_{0.5}\text{In}$ and b) $\text{Li}_{0.5}\text{In}$ -SE (20 wt% of SE) CEs and their corresponding EDXS elemental maps.

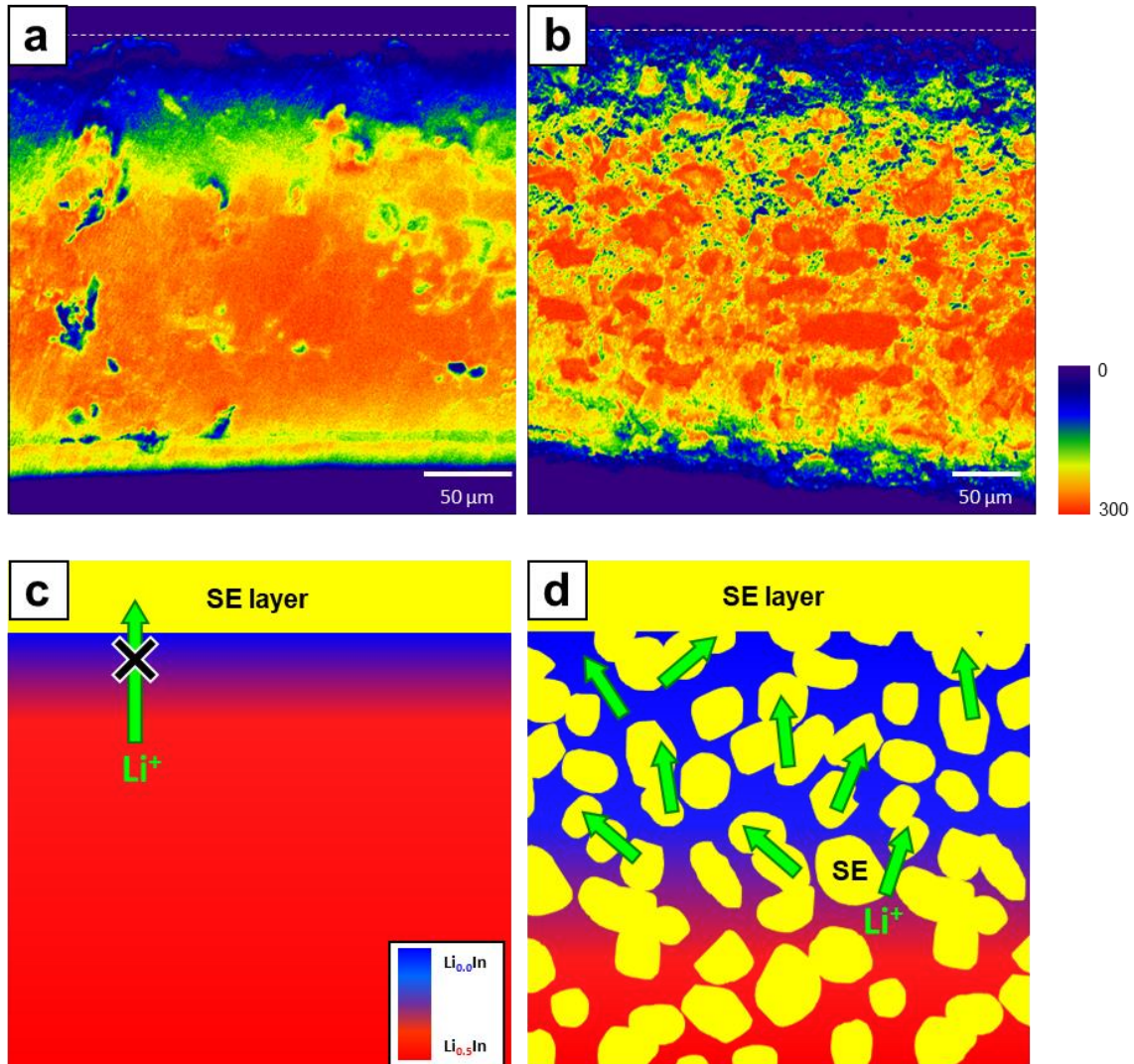


Figure 45. Results for concentration of Li^+ ions in cross-sectioned CEs ($\text{Li}_{0.5}\text{In}$ or $\text{Li}_{0.5}\text{In-SE}$ with 80:20 weight ratio) for Sn/Li-In(-SE) all-solid-state cells. Cross-sectional TOF-SIMS maps of Li^+ ions for a) $\text{Li}_{0.5}\text{In}$ and b) $\text{Li}_{0.5}\text{In-SE}$ CEs. The dashed lines indicate the outer surface of CEs. A scale bar with the maximum ion counts in a.u. is displayed in the right of (b). Schematics showing concentration of Li^+ ions in cross-sectioned a) $\text{Li}_{0.5}\text{In}$ and b) $\text{Li}_{0.5}\text{In-SE}$ CEs.

4.2.1.2. Internal Short-Circuit Behavior for All-Solid-State Full-Cells (NCM/Gr)

The second test vehicle for all-solid-state three-electrode cells is wet-slurry-fabricated NCM/Gr full-cells having thin SE layers. A cross-sectional FESEM image of the full-cell and its corresponding EDXS elemental maps clearly shows the 50-60 μm thick SE layer in between NCM and Gr electrodes without any noticeable mechanical failures (Figure 46). In NCM/Gr three-electrode cells, the upper SE layer in between the RE and the WE is in contact with the NCM electrode layer through a tiny hole ($\sim 1 \text{ mm}^2$) where the Al current collector is removed, as illustrated in Figure 3b. Note that the experimental conditions for the full-cells are realistic for practical applications in terms of the mass loadings (23 and 14 $\text{mg}_{\text{electrode}} \text{ cm}^{-2}$ for NCM and Gr electrodes, respectively) and the thickness of SE layer (50-60 μm). The NCM/Li-In and Gr/Li-In-SE (20 wt.% SE) half-cells showed first-cycle reversible capacities of 149 and 310 mA h g^{-1} , respectively, at 0.1C (Figure 47).

Figure 48a shows charge-discharge voltage profiles for NCM/Gr full-cell at different C-rates and their corresponding differential capacity curves. The discharge capacity of the full-cell is 137 $\text{mA h g}_{\text{NCM}}^{-1}$ at 0.1C. As the C-rate is increased, the data show increased polarization and consequently decreased capacities (e.g., 82 $\text{mA h g}_{\text{NCM}}^{-1}$ at 1C), which is not surprising. However, abnormal behaviors are observed for the charge voltage curves starting at 0.5C; the plateaus in the high voltage regions beginning at $\sim 4.1 \text{ V}$ (indicated by the lines in red), which corresponds with the sharp peaks in the differential capacity plots. The separated voltage profiles for NCM and Gr electrodes vs. Li/Li^+ at 0.1C and 1C, measured from three-electrode cells, are plotted in Figure 48b (the full voltage profiles at various C-rates are also provided in Figure 49). Starting at 1C, charging of the Gr electrode proceeds below 0 V (vs. Li/Li^+). This would inevitably lead to deposition of Li metal on the surface of Gr.¹⁴²⁻¹⁴⁴ One more interesting abnormal feature is much lower Coulombic efficiency values at high C-rates ($\geq 0.5\text{C}$) than those at low C-rates (Table 5). 99.0% Coulombic efficiency at 0.2C is drastically decreased to 88.7, 80.3, and 82.5% at 0.5C, 1C, and 2C, respectively. Consistently, NCM/Li all-solid-state cells show the abnormal behaviors similar to the NCM/Gr full-cells; the plateau at later stage of charge (delithiation for NCM electrode and Li plating for Li metal electrode) at high C-rates and the corresponding excessive charge capacity (Figure 50). These observations suggest soft ISCs caused by penetrating growth of Li metals through the SE layers.^{6, 137, 142-144} In order to verify the deposition of Li metals in the Gr electrodes for all-solid-state cells, ex-situ ^7Li magic angle spinning nuclear magnetic resonance (MAS-NMR) measurements were carried out for the mixture samples of Gr electrodes and SE layers in contact with the Gr electrodes from the Gr/Li-In all-solid-state cells after lithiating the Gr electrodes at two different C-rates of 0.1C (for 8 h) or 2C (20 min) (Figure 51a). The spectrum for the sample collected from the cell run at 2C shows a clear evidence of formation of metallic Li at 264 ppm (denoted ‘ \blacklozenge ’, Figure 51b).¹⁴⁵ In sharp contrast, the spectrum for the case of the lower C-rate (0.1C) is free from any signals of metallic Li. Further, unique all-solid-state three-electrode cells of Gr/Ni-coated

nonwoven (Ni-NW)/Li-In were prepared as an attempt to directly detect penetrating growth of Li metal through the SE layers (Figure 51c). The SEs could be impregnated into the porous structures of the Ni-NW electrode, being interconnected to provide the good ionic conduction pathways through the Ni-NW electrode. The lithiation current of 2C for the Gr electrode was applied between Gr and Li-In electrodes while the voltage of Ni-NW electrode with respect to Li-In electrode was measured. Again, the C-rate of 2C is high enough to cause the charging voltage of Gr electrodes below 0 V (vs. Li/Li⁺) in the NCM/Gr full-cells and the corresponding abnormal behaviors of high voltage plateaus (Figure 48a) and the low Coulombic efficiencies (Table 5). The voltage of Ni-NW electrode remains constant at ~1.8 V (vs. Li/Li⁺) up to 0.17 h (Figure 52d). However, it abruptly falls to the voltage close to the one for the Gr electrodes. This result clarifies the electrical connection (or ISC) between Ni-NW and Gr electrodes, which must be attributed to the penetrating growth of Li metal through the SE layers. In short, the deposition of metallic Li in Gr electrodes at high C-rate and the ISC caused by penetrating growth of Li metal through the SE layers were unprecedentedly evidenced from the results of ⁷Li MAS-NMR and the unique Gr/Ni-NW/Li-In all-solid-state three-electrode cells.

From the complementary analysis results so far, the penetrating growth of Li metal in the NCM/Gr all-solid-state full-cells and its effect on the abnormal electrochemical behaviors are illustrated in Figure 52. Once any ISCs are made by the penetrating Li metal, NCM being in touch with Li metal will be chemically lithiated by consuming the as-contacted Li metal, which is the opposite direction to charge and causes leakage current. Consequently, significant imbalance in the amount of charge and discharge through the external circuits (or low Coulombic efficiency) is observed. The results for NCM/Gr full-cell having conventional thicker SE layers (730 μm) are also compared (Figure 53). The discharge of Gr electrodes under 0 V (vs. Li/Li⁺) is still observed, indicating the possible deposition of Li metal on Gr. However, the abnormal behaviors of the high-voltage plateaus (Figure 48a) and the low CE values at high C-rates (Table 5) are not seen for the case using thicker SE layers. This could be rationalized by much less possibility of ISC because of approx. ten times longer distances for Li metal to penetrate through.

It is worth noting that no significant changes in mechanical integrity for the composite NCM and Gr electrodes were observed after cycling (Figure 54). It is considered that the applied pressure (74 MPa) during the operation of all-solid-state cells would deform the SEs having low Young's modulus of 20-30 GPa, ⁶⁷ maintaining the integrity of the composite electrodes. However, severer test conditions, such as extended cycling and less applied pressure, may cause mechanical failure of ASLBs.

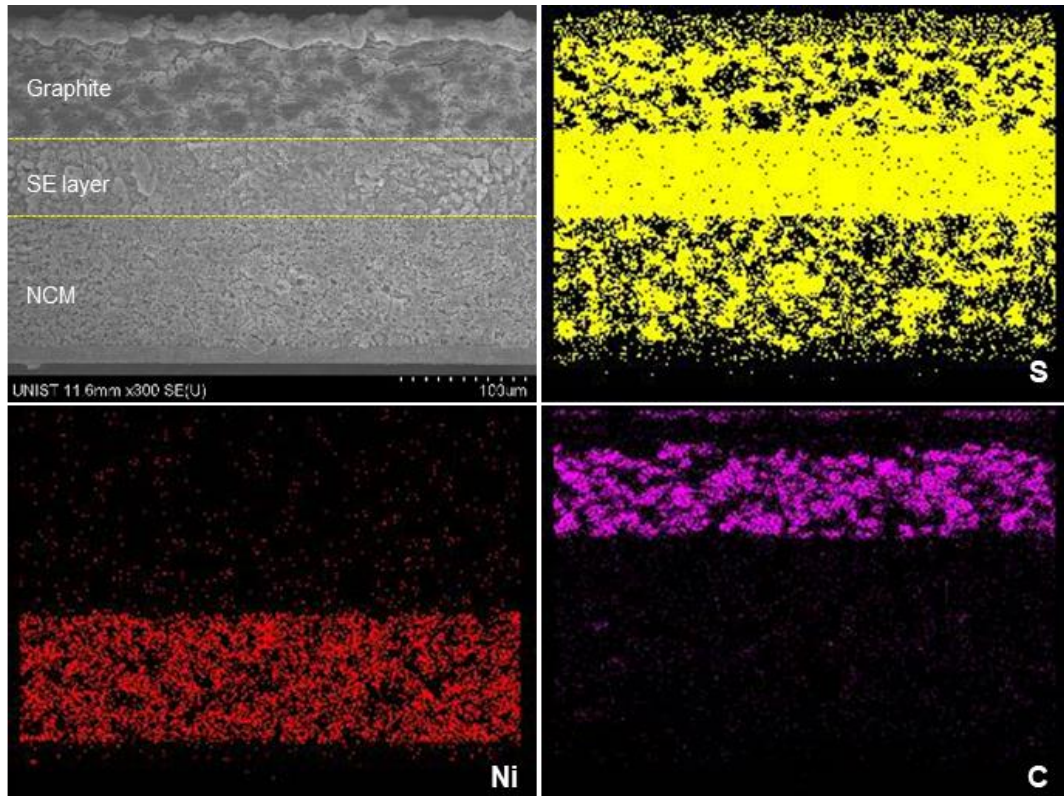


Figure 46. Cross-sectional FESEM images and the corresponding EDXS elemental maps for NCM/Gr all-solid-state full-cells using thin SE layer (50–60 μm).

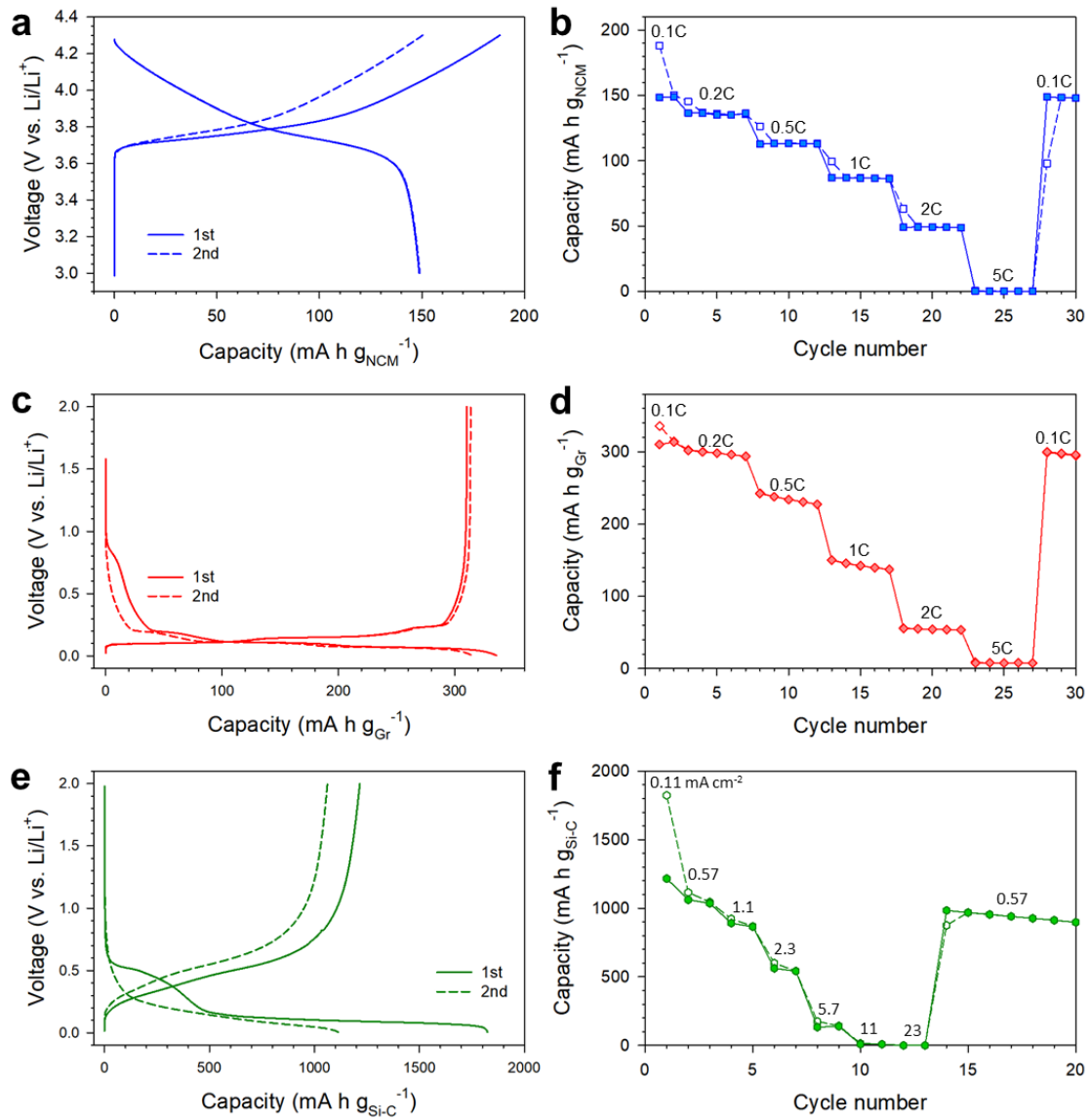


Figure 47. Electrochemical performances of NCM/Li-In, Gr/Li-In-SE, and Si-C/Li-In-SE all-solid-state cells. First two-cycle voltage profiles of a) NCM/Li-In, c) Gr/Li-In-SE, and e) Si-C/Li-In-SE all-solid-state cells at 0.1C, 0.1C, and 0.11 mA cm⁻², respectively. The corresponding rate capabilities for a) NCM/Li-In, c) Gr/Li-In-SE, and e) Si-C/Li-In-SE all-solid-state cells are shown.

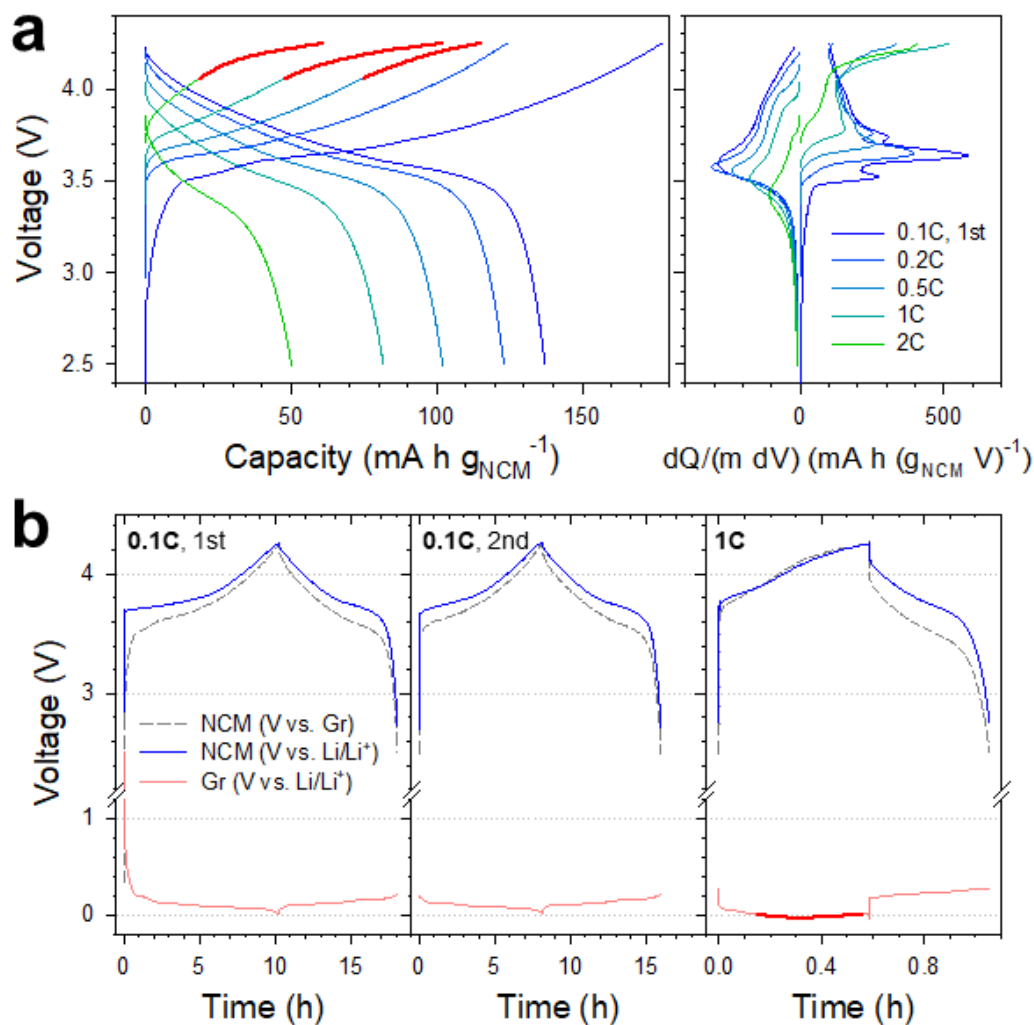


Figure 48. Results for NCM/Gr all-solid-state three-electrode cells employing thin SE layers (50–60 μm), suffering from ISC by penetrating growth of Li metal. a) Charge-discharge voltage profiles and the corresponding differential capacity plots at different C-rates. Note the abnormal plateaus plotted in red during charge at high C-rates. b) Transient charge-discharge voltage profiles for each electrode at different C-rates. Note the voltage region of Gr, which is lower than 0 V (vs. Li/Li⁺) at high C-rate, 1C, shown in thick red line.

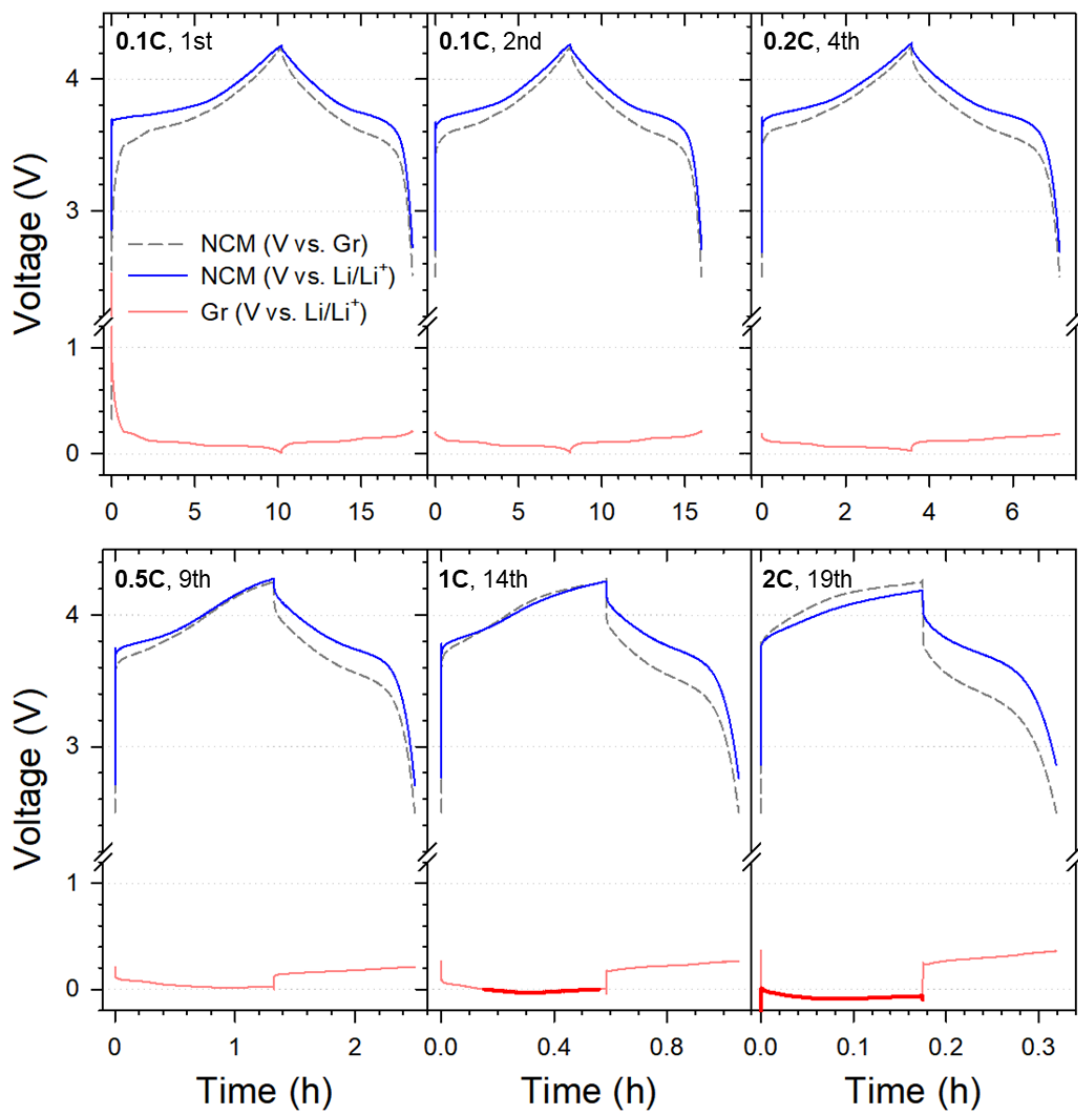


Figure 49. Transient charge-discharge voltage profiles of each electrode for NCM/Gr all-solid-state three-electrode cells at different current densities. Note the voltage region of Gr, which is lower than 0 V (vs. Li/Li⁺) at high C-rate, 1C, shown in bold red line.

Table 5. Coulombic efficiency for NCM/Gr all-solid-state full-cells.

Thickness of SE layer [μm]	Characteristics	0.1C (1st)	0.1C (2nd)	0.2C (4th)	0.5C (9th)	1C (14th)	2C (19th)
50-60	Discharge capacity [mA h g^{-1}]	177	141	124	115	102	61
	Charge capacity [mA h g^{-1}]	137	137	123	102	82	50
	Coulombic efficiency [%]	77.3	97.5	99.0	88.7	80.3	82.5
730	Discharge capacity [mA h g^{-1}]	184	145	130	103	76	42
	Charge capacity [mA h g^{-1}]	146	145	130	103	76	42
	Coulombic efficiency [%]	79.2	99.8	100.0	99.8	99.7	99.5

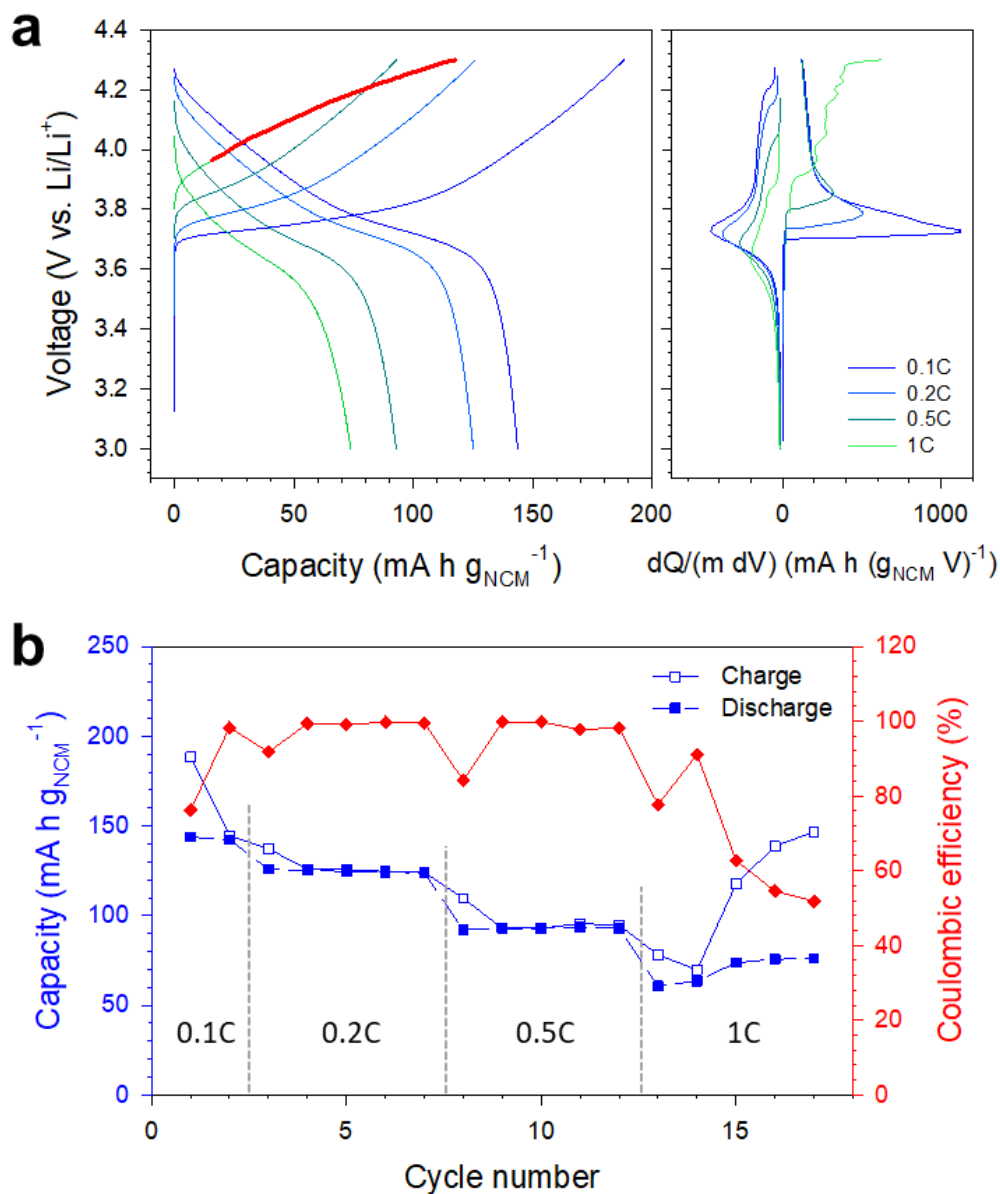


Figure 50. a) Charge-discharge voltage profiles and their corresponding differential capacity plots for NCM/Li all-solid-state cells at 30 °C and various C-rates. b) Charge and discharge capacity varied by C-rates and the corresponding Coulombic efficiency as a function of cycle number. Note the abnormal plateau plotted in red at 1C in (a) and the corresponding low Coulombic efficiencies in (b), indicating the soft ISC by penetrating growth of Li metal.

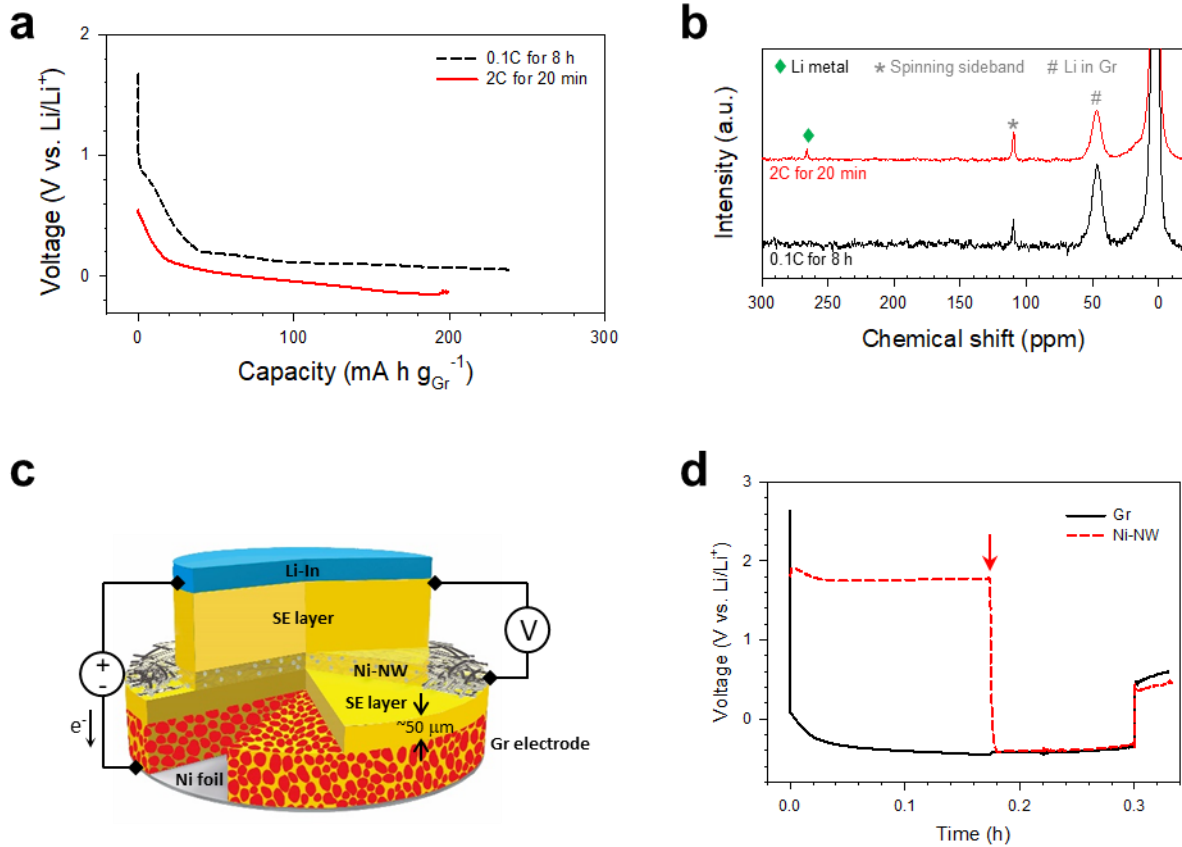


Figure 51. First-cycle discharge (lithiation) voltage profiles for Gr/Li-In all-solid-state cells at different C-rates, which were used for ⁷Li MAS NMR spectroscopy measurements (Figure 51b). After the discharge, the mixtures of SE layers and Gr electrodes, collected from the disassembled cells, were subjected to the ⁷Li MAS NMR spectroscopy measurements. Results for NCM/Gr all-solid-state three-electrode cells employing thin SE layers (50–60 μm), suffering from ISC by penetrating growth of Li metal. a) ⁷Li MAS-NMR spectra for the mixtures of SE layers and Gr electrodes collected from the Gr electrodes after lithiation at 0.1C or 2C. The corresponding voltage profiles are provided in Figure 51a. b) Schematic illustrating Gr/Ni-NW/Li-In all-solid-state three-electrode cells and c) the corresponding transient charge-discharge voltage profiles at 2C for Gr and Ni-NW electrodes. While the current flows between Gr and Li-In electrodes, the voltage of Ni-NW electrodes was measured to detect the ISC.

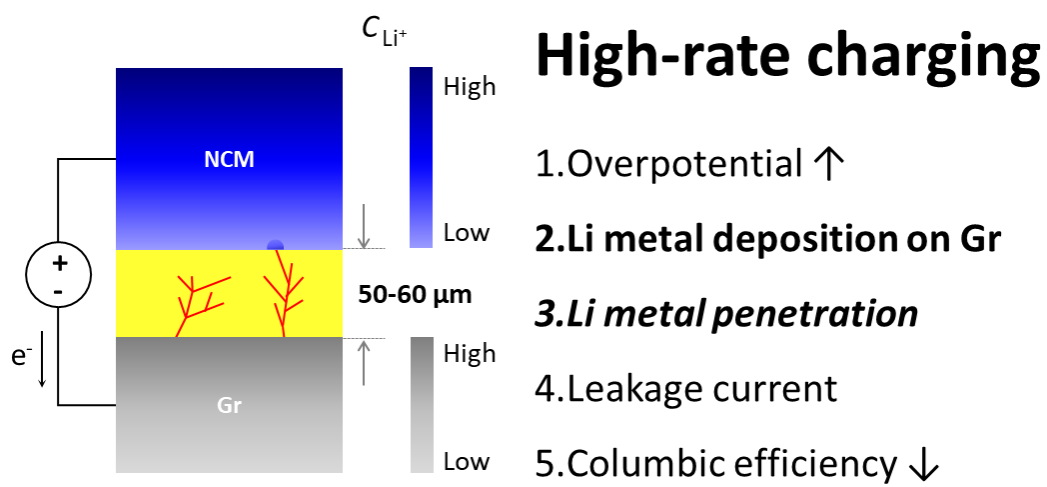


Figure 52. Schematic showing the ISC induced by penetration of Li metal for NCM/Gr all-solid-state cells during charge at high C-rates.

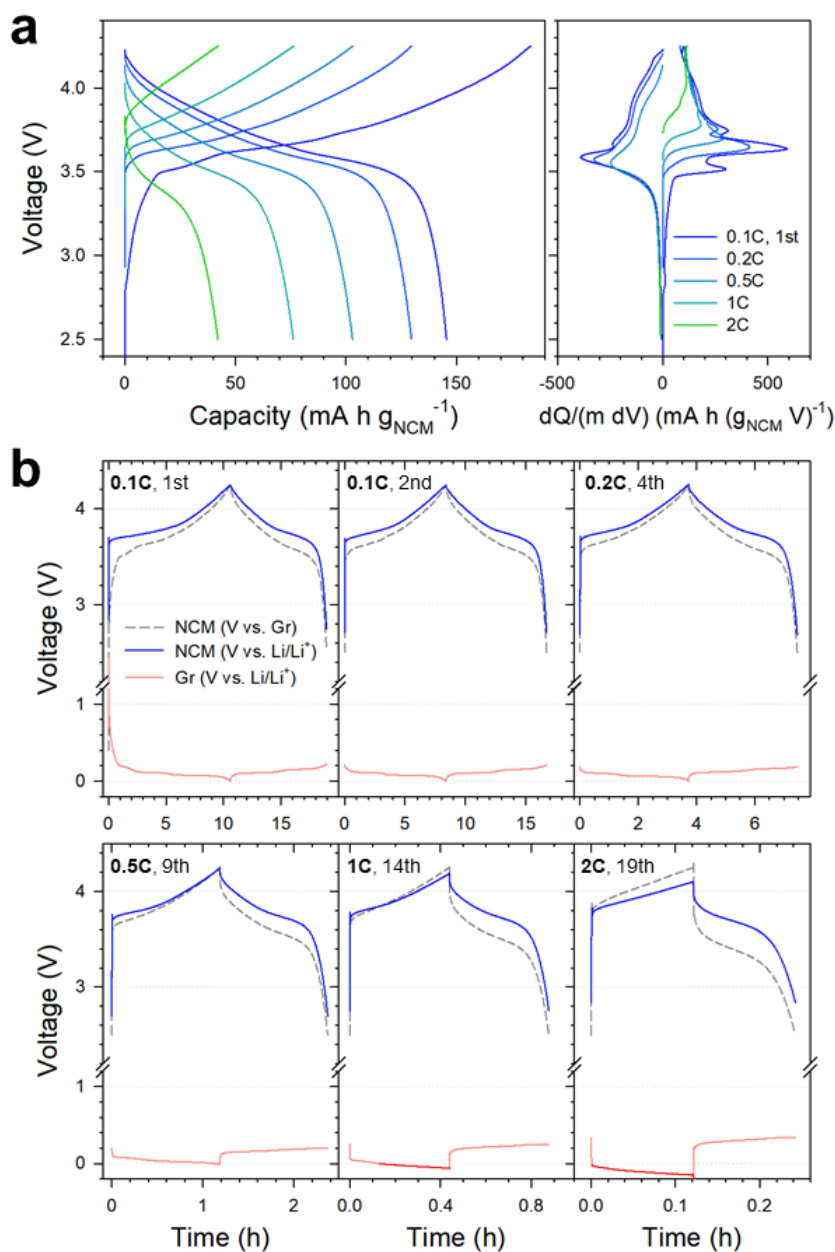


Figure 53. Results for NCM/Gr all-solid-state three-electrode cells employing thick SE layers ($730 \mu\text{m}$), being free from ISC. a) Charge-discharge voltage profiles and the corresponding differential capacity plots at different C-rates. b) Charge-discharge voltage profiles for each electrode at different C-rates. Note the voltage region of Gr which is lower than 0 V (vs. Li/Li^+) at high C-rate, 1C, shown in bold red line.

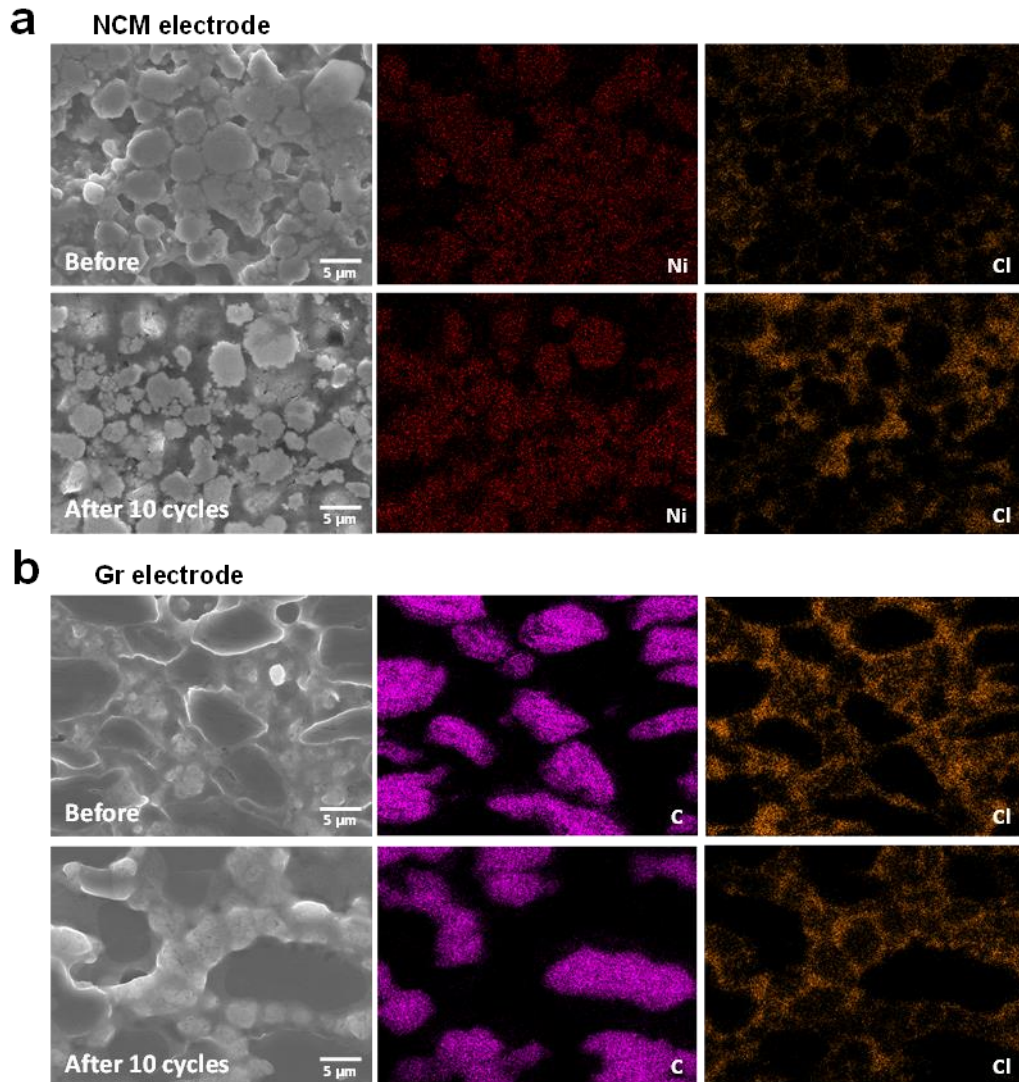


Figure 54. Cross-sectional FESEM images and their corresponding EDXS elemental maps for a) NCM and b) Gr electrodes of NCM/Gr all-solid-state full-cells using thin SE layer (50–60 μm) before cycling and after 10 cycles at 0.2C.

4.2.1.3. 0 V dischargeability for All-Solid-State Full-Cells (NCM/Gr and NCM/Si-C)

Once activated by formation cycles in the manufacturing processes, conventional LIBs using LEs, must not be discharged to 0 V because of permanent failure of the cells by dissolution of Cu current collectors for negative electrodes, which experience high voltages above 3 V (vs. Li/Li⁺). Therefore, careful management in discharge is necessary to guarantee the health and safety of LIBs.¹⁴⁶ For the case of ASLBs, Cu might not be used as the current collectors because of its chemical reactivity with sulfide materials (Ni foils were used for negative electrodes in this work). Even if Cu current collector could be used for ASLBs, there is no dissolution issue. In this regard, durability of ASLBs upon discharge to 0 V needs to be assessed.

Another interesting feature found in the behavior of all-solid-state NCM/Gr full-cell in Figure 48b is the balance in utilization of positive and negative electrodes. The overall first-cycle discharge is ended by full lithiation of NCM, not by full delithiation of Gr, which is opposite to the case for conventional LIBs using LEs.¹³⁹ This unique feature stems from the lower first-cycle Coulombic efficiency of NCM (79.1%) in contact with SEs than that of Gr (92.5%) (Figure 47). For systematic assessment, a NCM/Si-C full-cell, where the Si-C electrode shows much lower first-cycle Coulombic efficiency (66.7%) than Gr or NCM electrodes, is compared. After normal charge-discharge for three cycles (2.50-4.25 V and 1.20-4.25 V for NCM/Gr and NCM/Si-C, respectively), the NCM/Gr and NCM/Si-C full-cells were subjected to discharge to 0 V at constant current and the subsequent constant voltage of 0 V for 24 h. Then, they were cycled in the normal voltage ranges again. The transient voltage profiles during discharge to 0 V are presented in Figure 55 (the overall transient voltage curves are also shown in Figure 56). As designed, the normal discharge is ended by termination (or full utilization) of the NCM electrode for NCM/Gr and the Si-C electrode for NCM/Si-C (note the terminal voltage for Si-C electrode is much higher than that for Gr electrode, indicated by the sign of '*'). Discharge to 0 V at the following cycle for NCM/Gr leads to excessive lithiation reaction for NCM electrode at ~1.8 V (vs. Li/Li⁺), as indicated by the arrow in Figure 55a. In contrast, the voltages of NCM electrodes for NCM/Si-C remain high above 3 V (vs. Li/Li⁺) (Figure 55b). At the subsequent cycles in the normal voltage ranges, unexpectedly, not only NCM/Si-C but also NCM/Gr full-cell shows no noticeable degradation, as shown in Figure 55-57. In a recent study for Ni-rich LiNi_{0.75}Co_{0.25}O₂, a plateau at 1.75 V (vs. Li/Li⁺) upon over-discharge was observed, which was assigned as a reversible two-phase transformation without breakdown of the layered host structure by an in-situ XRD analysis.¹⁴⁷ While clear elucidation on the mechanism for reversible over-discharge of the NCM electrodes for ASLBs upon discharge to 0 V remains, the 0 V dischargeability for ASLBs will offer more flexibility in their management and handling in terms of charge-discharge ranges and less safety concerns (e.g., transportation by airplanes).¹⁴⁶

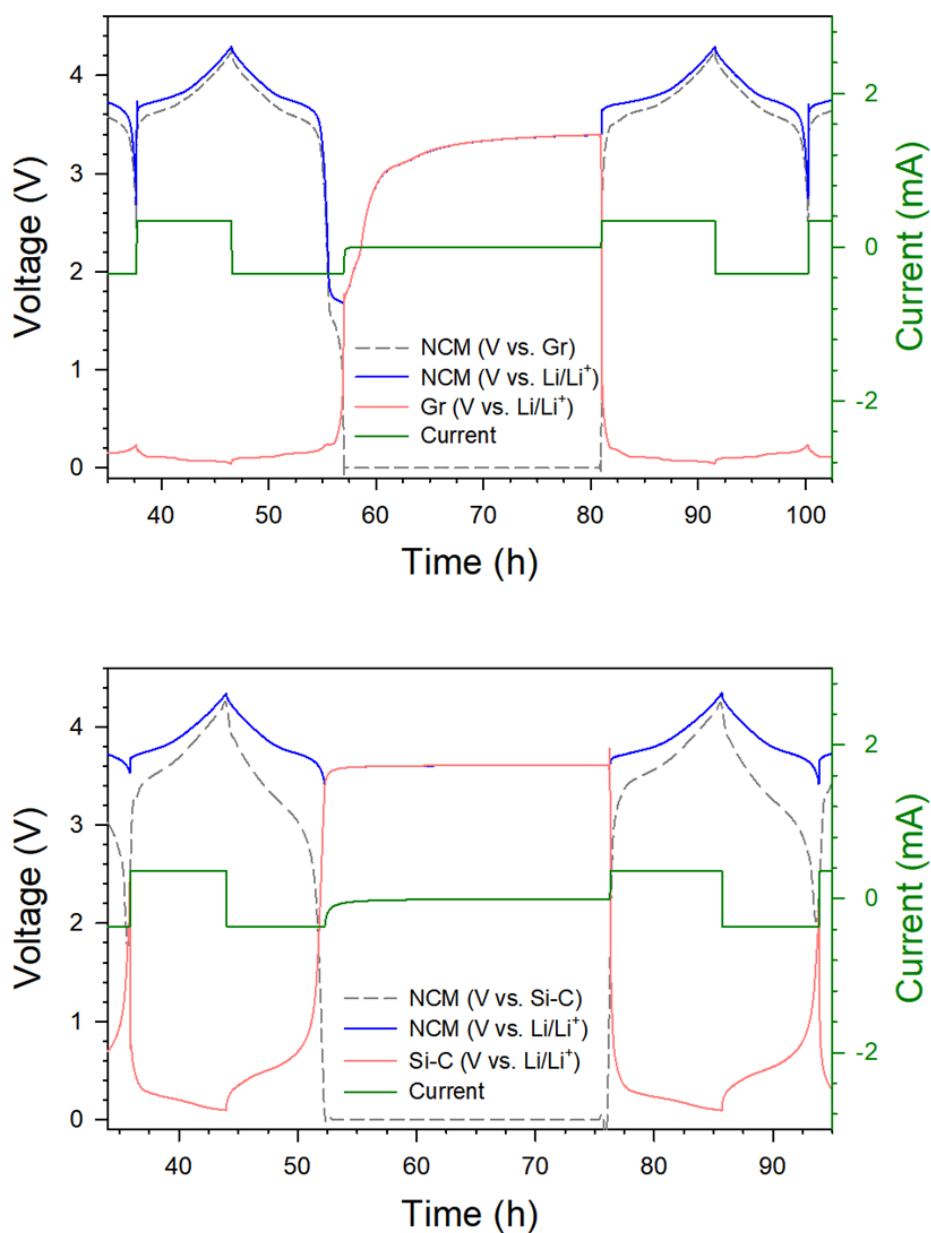


Figure 55. Results for NCM/Gr and NCM/Si-C all-solid-state three-electrode cells discharged to 0 V. Transient charge-discharge voltage profiles for each electrode for a) NCM/Gr and b) NCM/Si-C cells during discharge to 0 V. Note the higher cutoff voltage for Si-C electrode in (b) than that for Gr electrode in (a) (indicated by ‘*’) during normal discharge. Also note the lower terminal voltage for NCM electrode in NCM/Gr cell (indicated by an arrow) in (a) than that for NCM electrode in NCM/Si-C cell in (b) upon discharge to 0 V.

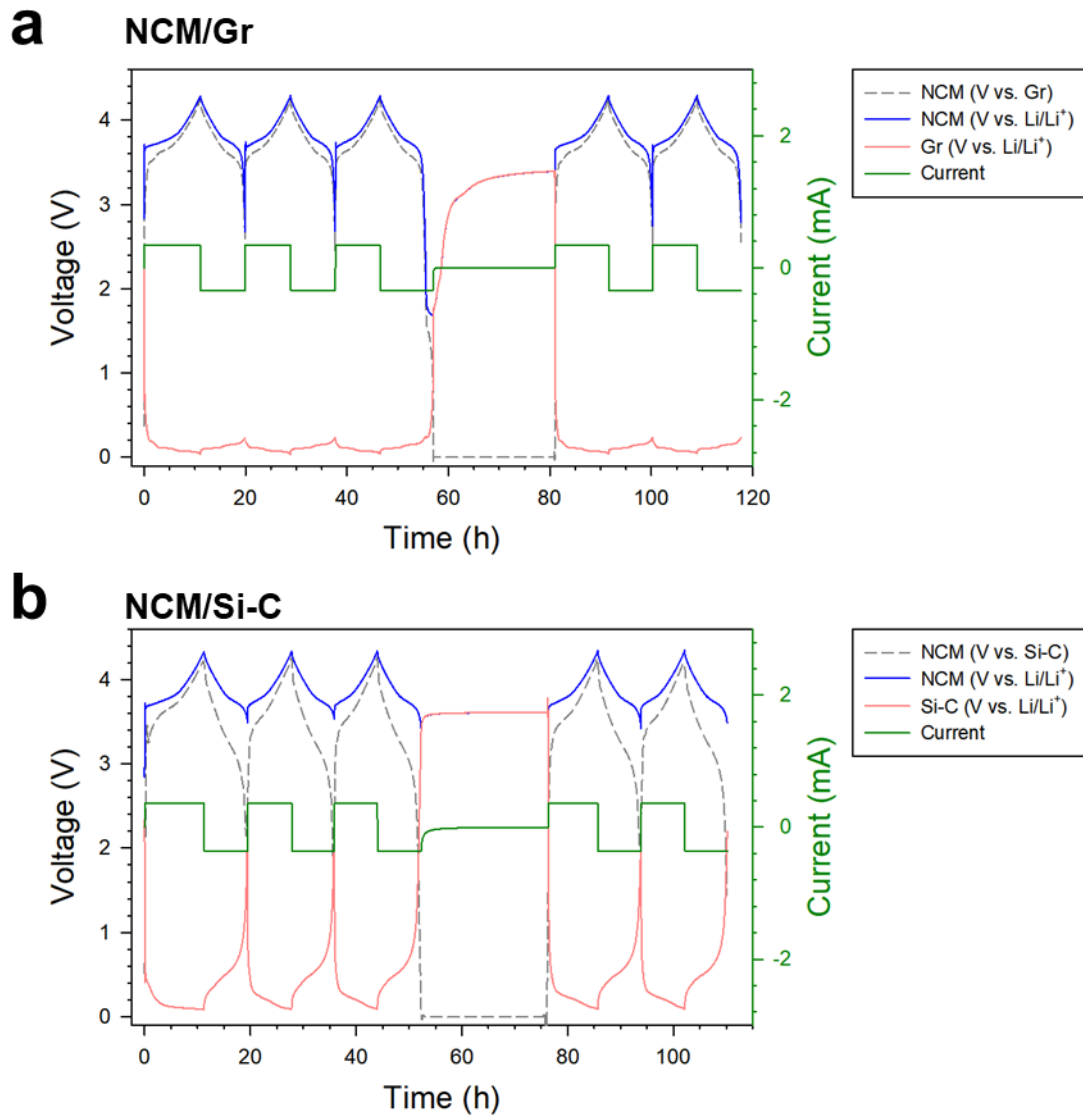


Figure 56. Transient charge-discharge voltage profiles of each electrode for a) NCM/Gr and b) NCM/Si-C all-solid-state three-electrode cells during discharge to 0 V. Figure 55 is the enlarged view in x-axis.

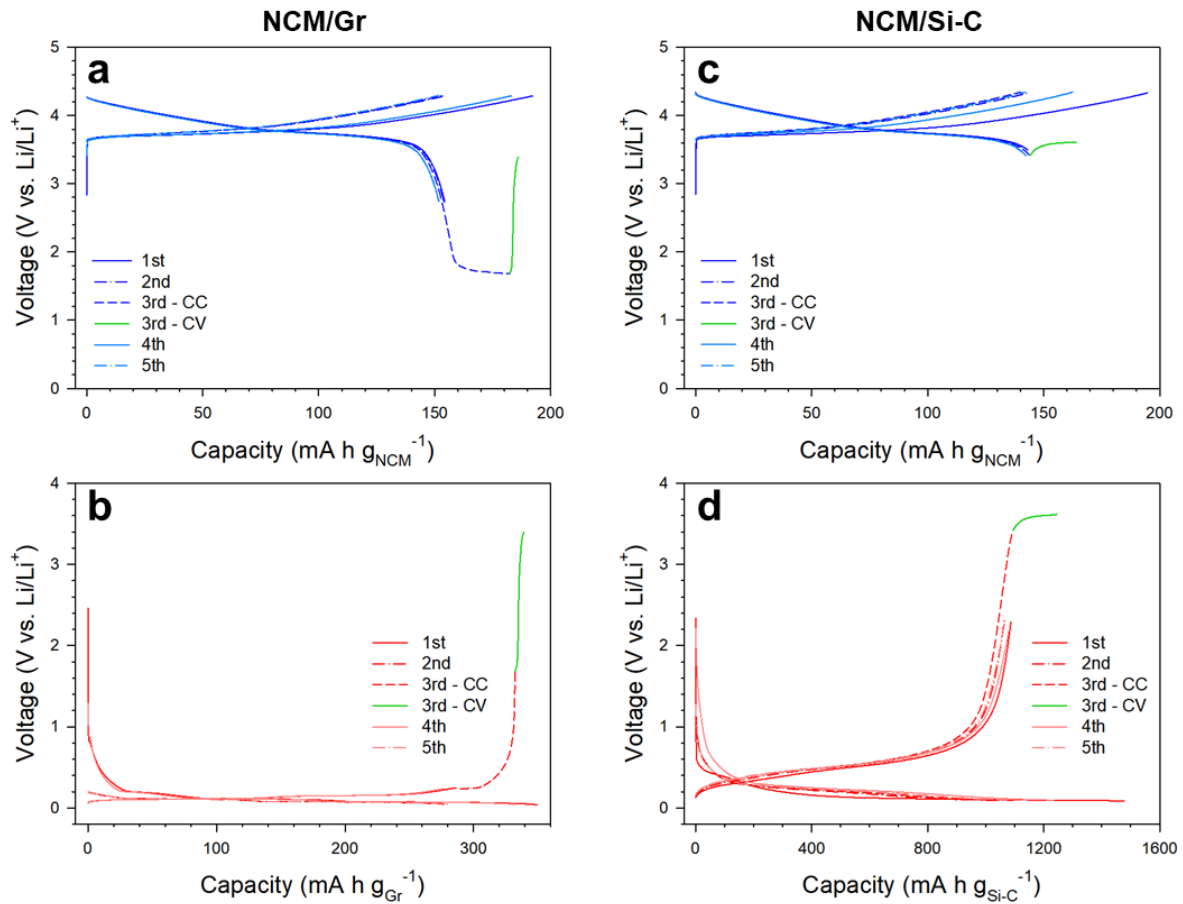


Figure 57. Charge-discharge voltage profiles of a, c) NCM electrodes, b) Gr electrode, and d) Si-C electrode for NCM/Gr or NCM/Si-C all-solid-state three-electrode cells during discharge to 0 V.

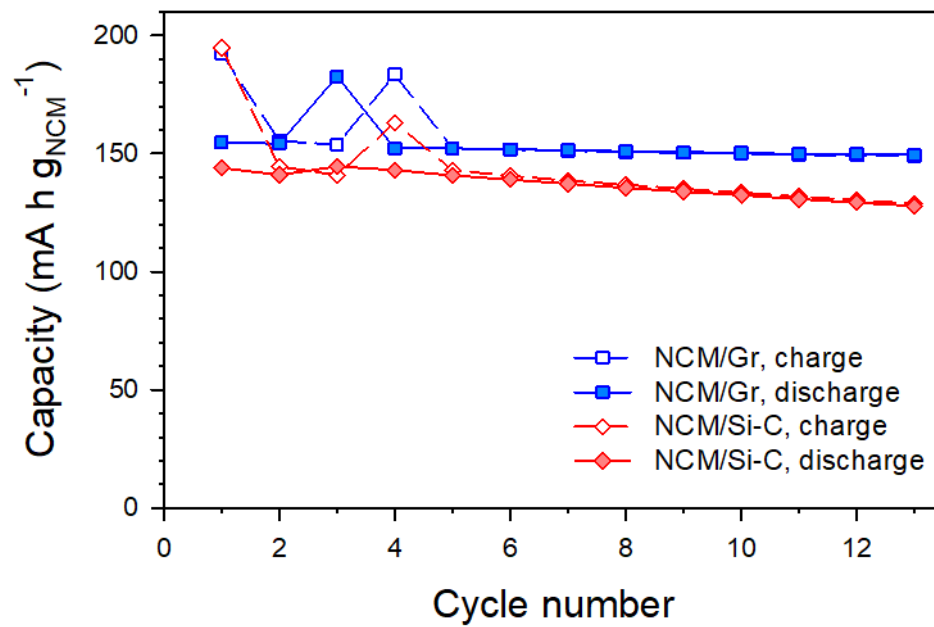


Figure 58. Cycling performances of NCM/Gr and NCM/Si-C all-solid-state cells during discharge to 0 V. The corresponding charge-discharge voltage profiles are shown in Figures 55-57.

4.2.2. Pressure Monitoring System

To date, many studies of ASLBs have focused on investigating the electrode chemistries. Conventional electrode materials used for LIBs, such as Li_xMO_2 ($M = \text{Co}, \text{Ni}, \text{Mn}$), graphite, and $\text{Li}_4\text{Ti}_5\text{O}_{12}$, have been investigated for application in ASLBs. High-capacity sulfur- or Li_2S -based composite electrodes have also been developed for application to ASLBs. However, their highly insulating characteristics and large changes in dimension upon insertion/extraction of lithium ions pose critical challenges to realizing ASLBs with reliable and sustainable electrochemical properties. In contrast, the high operating voltage ($\sim 4 \text{ V vs. Li/Li}^+$), low volume change during charge-discharge (e.g. 1.9% for LiCoO_2), and moderate electrical conductivity of the conventional Li_xMO_2 (e.g. $\sim 10^{-3} \text{ S cm}^{-1}$ for LiCoO_2 and $\sim 20 \text{ S cm}^{-1}$ for $\text{Li}_{0.5}\text{CoO}_2$) make Li_xMO_2 well-suited for application in ASLBs.⁶⁶⁻⁶⁷ Li_xMO_2 has poor compatibility with sulfide SE, however, and a variety of surface modification treatments (in particular, metal oxide coatings) have been performed on Li_xMO_2 in order to overcome this drawback. Other than the protective coatings, while surface chemistries of the bare Li_xMO_2 is also known to be critical on the performance of the conventional liquid electrolyte cells, investigation on the performance of bare Li_xMO_2 varied by surface chemistry is scarce for ASLBs. Recently, Janek and co-workers claimed that ionic contacts between Li_xMO_2 and SEs are also deteriorated by their low volume change during charge-discharge.^{66-67, 134, 148} In this regard, as most studies of ASLBs were performed under high external pressure (tens of MPa), these problems are considered as a critical hurdle for the practical applications.⁶⁶⁻⁶⁷ Thus, the understanding and controlling of interfacial behavior in terms of mechanical stress from volume expansion of active materials and/or decomposition of SE is imperative for the development of ASLBs.⁶⁶⁻⁶⁷

In this part, the pressure monitoring in operating cells is proposed for the state-of-charge (SOC) estimation of graphite electrode in NCM/Gr full-cells from volume changes of graphite electrode with various weight fraction of LGPS, which has irreversible reaction at the low potential. Also, as the rearrangement of electrodes during cycling was observed, the formation process in terms of pressure stabilization including decomposition of SE, internal volume changes of active materials and external applied pressure should be considered as achieving high performance of ASLBs.

4.2.2.1. SOC Estimation of Graphite Electrode from Pressure Change of NCM/Gr full-cells

As the state-of-charge (SOC) estimation of lithium rechargeable batteries is an indicator that represents the remaining capacity in cells, it has been considered as one of the promising key factors in battery management systems (BMS).¹⁴⁹⁻¹⁵¹ Although it is difficult to be measured directly from battery system, many approaches based on precise electrochemical battery models for extracting SOC information from outputs of lithium rechargeable batteries have been reported. However, to obtain accurate SOC values using electrochemical models, as their electrochemical parameters are required for the information of components in battery system, which is affected by internal environments, it is highly complicated method for the SOC estimation.¹⁴⁹⁻¹⁵¹ Thus, the volume change of electrode during cycling is easily tracking the electrochemical behavior of battery system. As the electrochemical performance of all-solid-state lithium batteries (ASLBs) is greatly affected by external applied pressure, the setup of pressure monitoring in operating is imperative.

In this regard, generally, as the volume change of $\text{Li}_x\text{MoO}_2/\text{Gr}$ full-cells are affected strongly by that of anode materials, the electrochemical behavior of Li-ion intercalation into Gr electrode and decomposition of SEs was investigated. Figure 59 represents the voltage profiles of graphite/Li-In-SE half-cells with different weight fraction of SE (LPSCl:LGPS=100-x:x). The initial Coulombic efficiency of Gr half-cells decreases with increasing weight fraction of LGPS because of narrow electrochemical window of LGPS.^{44-45, 53, 101} And then, the discharge capacity of NCM/Gr full-cells also decreases with same trends of the results of half-cells (Figure 60). To verify the irreversible reaction of LGPS, which is consuming the Li-ions from NCM materials, ex-situ XRD patterns of NCM/Gr full-cells were performed. NCM/Gr (LPSCl) full-cell shows normal behavior of Li movements from NCM to Gr during charge. And then, at the discharge, the reversible Li-ion movements was observed (Figure 61a).^{147, 152-153} However, the graphite electrode with 20, 80 wt% LGPS shows high irreversible capacity and incomplete lithiation behaviors of XRD patterns and photo images of Gr electrode with 0, 100 wt% LGPS (Figure 61).^{147, 152-153}

To tracking the interfacial behavior of NCM/Gr full-cells with different wt % LGPS in Gr electrode, the pure volume changes of Gr electrodes is essential for accurate analysis. As volume changes of NCM electrode with the same amount of extracted Li-ion are required, $\text{Li}_4\text{Ti}_5\text{O}_{12}$, which is well-known zero-strain materials, are used as counter electrode (Figure 62). Thus, Figure 63 represents that the pure volume change of Gr electrode with 0 wt% LGPS is in good agreement with total volume changes of lithium-graphite system (Li_xC_6).^{113, 152} From the results of NCM/Gr full-cell simulation and differential capacity ($dP/(m dQ)$), the SOC values of Gr electrode in NCM/Gr full-cells were estimated successfully (Figure 64 and Table 6). Furthermore, as NCM/Gr full-cells with 10, 20 wt% LGPS shows similar behavior of pressure changes and differential capacity, low SOC value at the starting point of discharge process is easily estimated (Figure 64). Consequently, the pressure monitoring in operating

cells allows SOC estimation without interruption of unfavorable reaction including decomposition of SEs and contacts loss from internal volume change of active materials during cycling. Thus, it will be one of the most promising electrochemical test protocols for understanding of complex interfacial chemistries^{85-86, 134, 138} and architectures^{134, 148}.

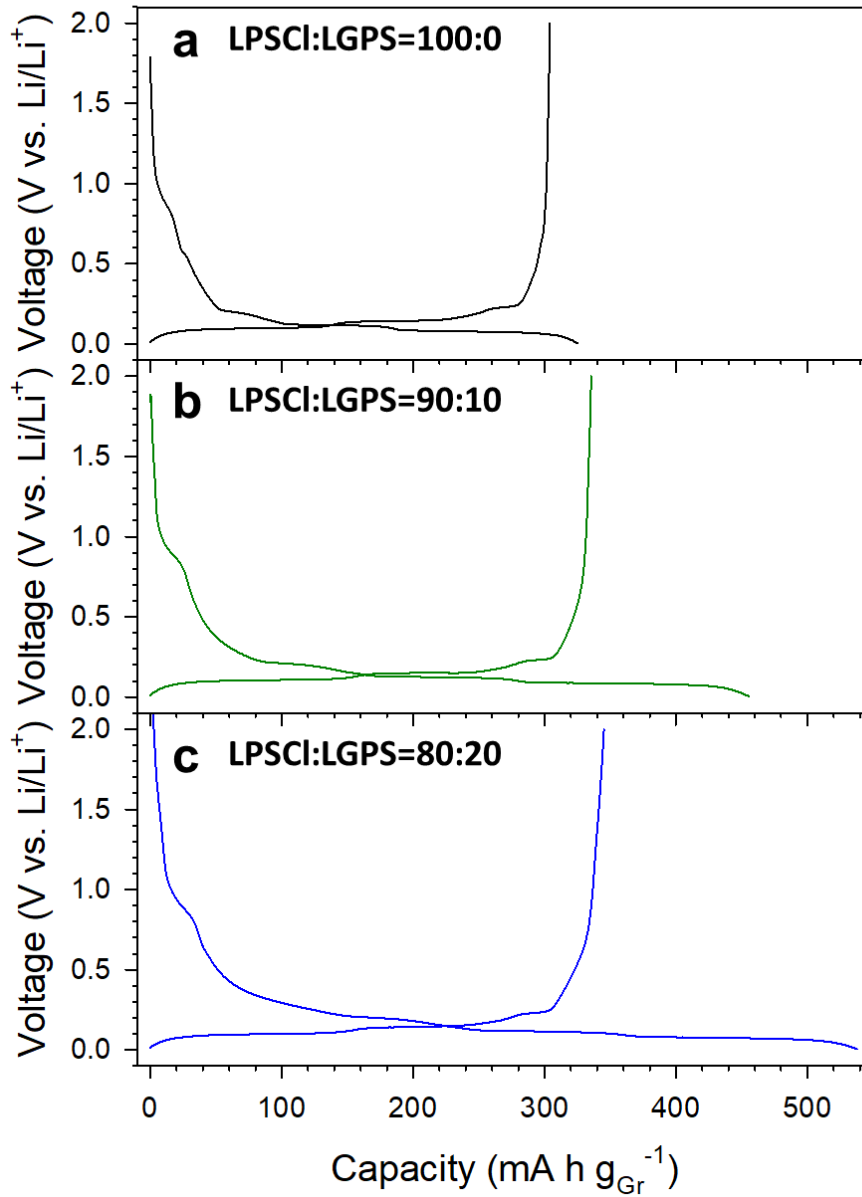


Figure 59. First charge-discharge voltage profiles of the graphite half-cells with different weight fraction of LGPS.

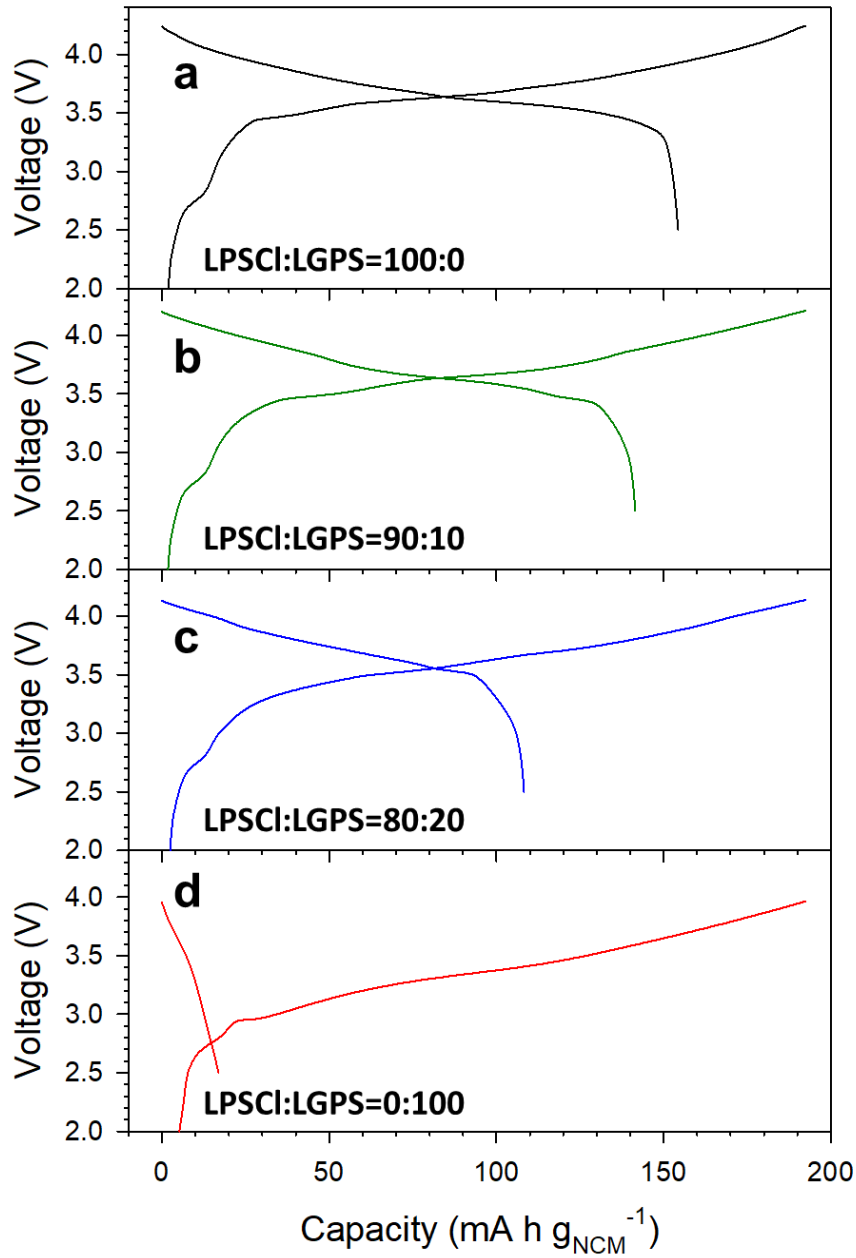


Figure 60. First charge-discharge voltage profiles of the NCM/graphite full-cells with different weight fraction of LGPS in graphite electrode.

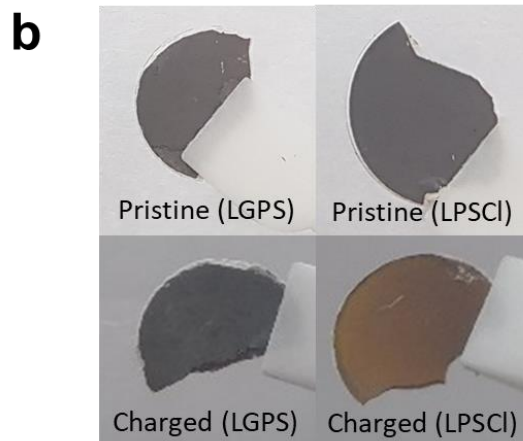
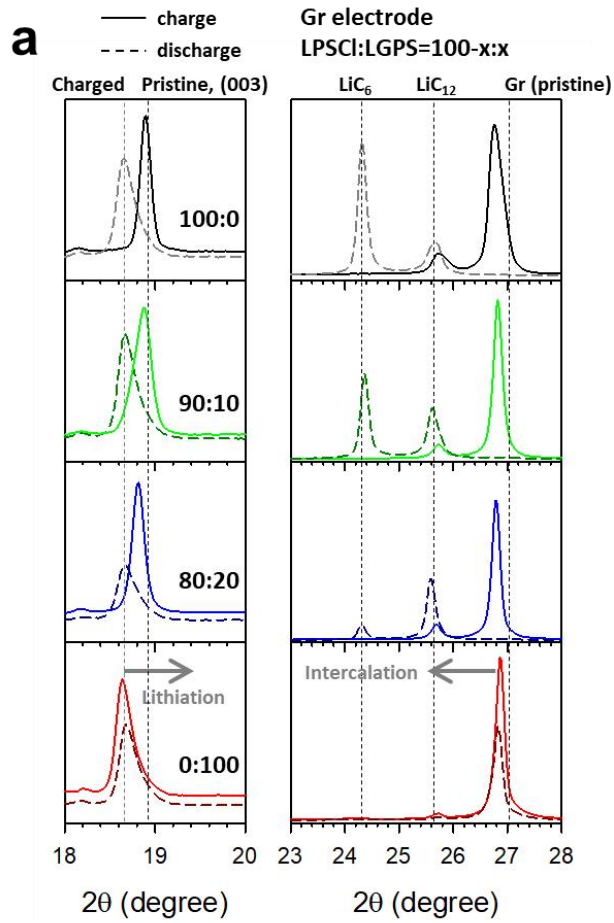


Figure 61. a) ex-situ XRD patterns of NCM and graphite electrodes at charge with different weight fraction of LGPS in graphite electrode at charged (dash line) and charge-discharged (solid line). b) Photographs of Gr electrodes with LGPS and LPSCI at charged.

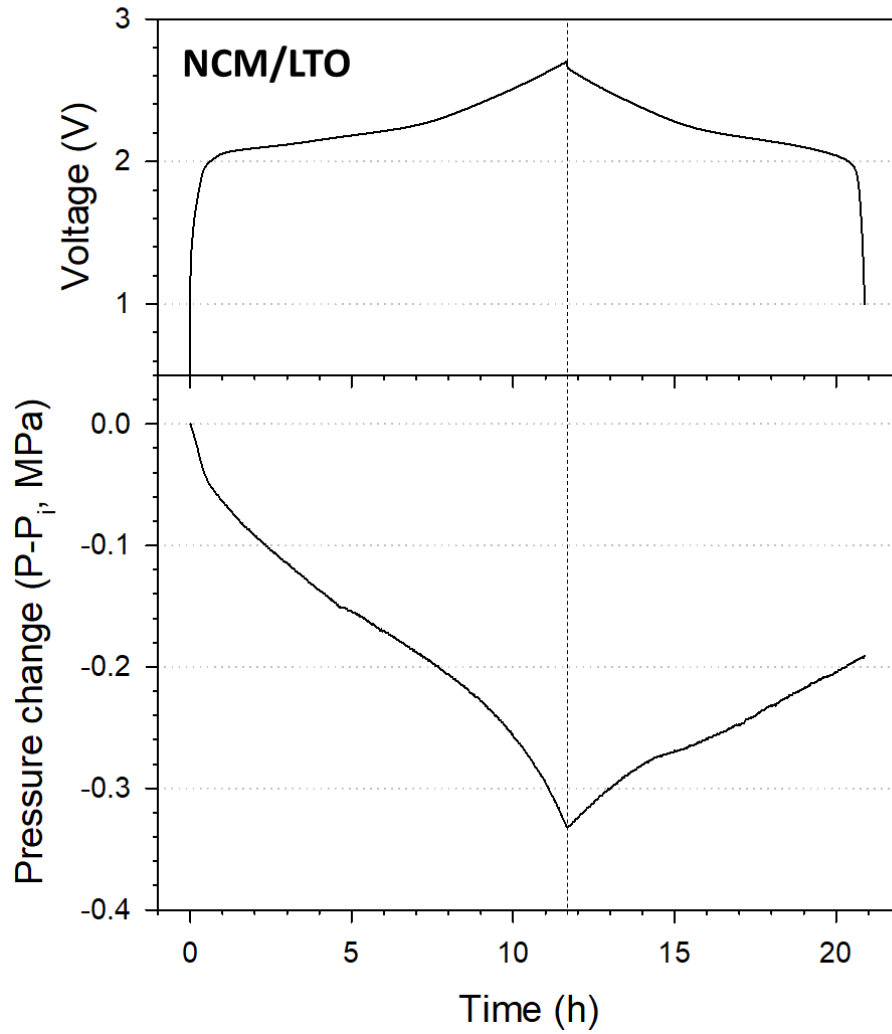


Figure 62. First charge-discharge voltage profiles of the NCM/LTO full-cells and the corresponding pressure change curve.

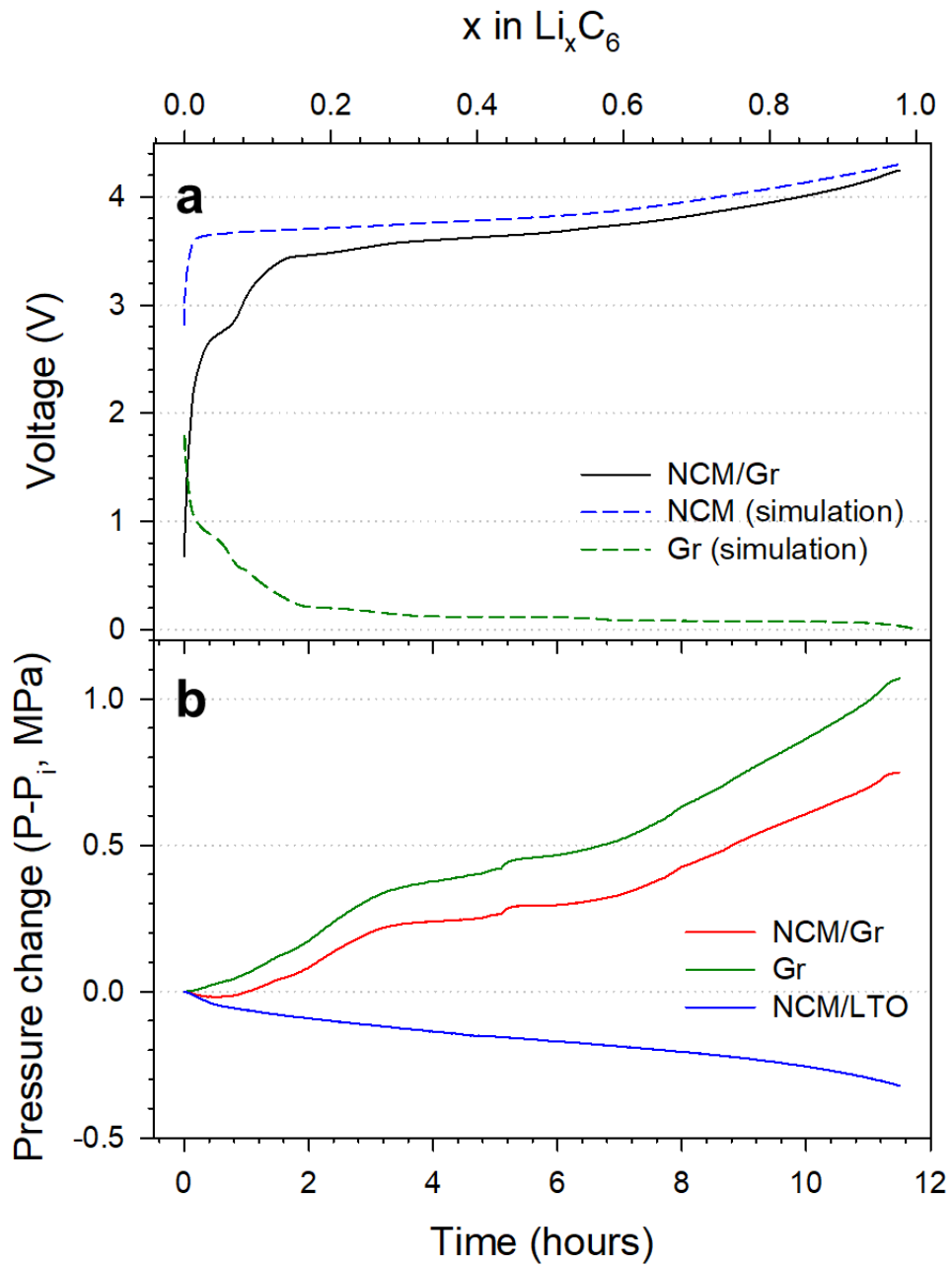


Figure 63. a) Voltage profile of NCM/Gr full-cell and simulation of NCM and graphite electrode, respectively. b) Pressure change of NCM/Gr full-cell, Gr electrode, NCM/LTO, respectively.

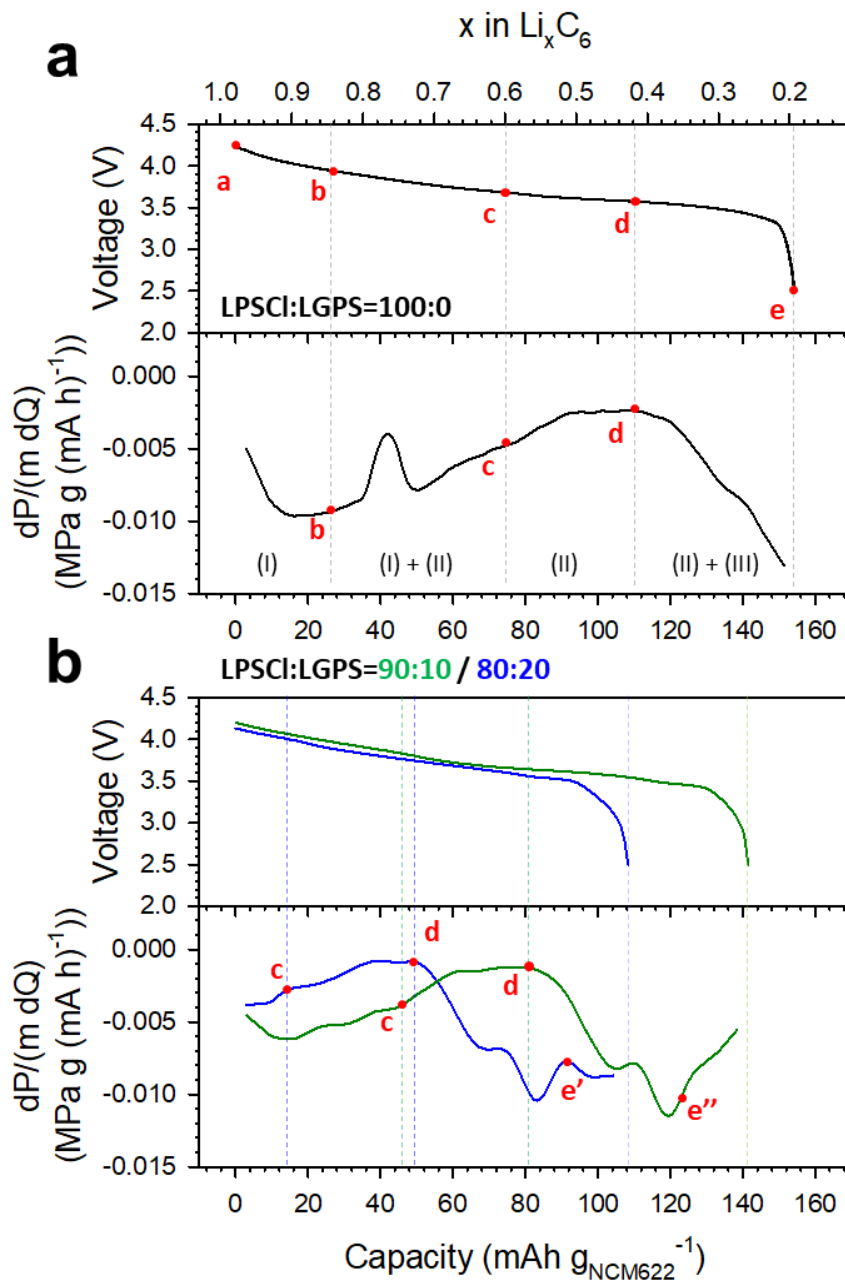


Figure 64. a) Voltage profile of NCM/Gr full-cell with 0 wt% LGPS in graphite electrode and the corresponding differential capacity plot. b) Voltage profiles of NCM/Gr full-cells with 10, 20 wt% LGPS and the corresponding differential capacity plot. The points (a-e, e' and e'') are estimated from pressure change of NCM/Gr full-cell in a).

Table 6. SOC estimation of graphite electrode from the results of pressure change.

Point	a	b	c	d	e	e'	e''
x (Li _x C ₆)	0.98	0.85	0.6	0.42	0.2	~0.2	~0.2
Phase	LiC ₆	LiC ₆	LiC ₁₂ + LiC ₆	LiC ₁₂	Dilute region	Dilute region	Dilute region

4.2.2.2. Rearrangement of Particles in Electrodes During Cycling

Another interesting feature found in the behavior of all-solid-state NCM/Gr full-cell in Figure 65 is the balance in pressure in positive and negative electrodes. As the all-solid-state NCM/Gr full-cells is ended by termination of NCM electrode, the volume expansion of graphite electrode slightly occurs. However, the cross-sectional FESEM image and their corresponding EDXS elemental maps of pristine Gr electrode indicate that the pore exists in pristine graphite electrode (Figure 66a). After cycling of NCM/Gr full-cells, it was deformed by volume expansion of graphite materials (Figure 65). As a result, the pressure change during cycling is almost zero at the fifth cycle (Figure 65). Although the electrochemical performance wasn't affected by net volume change of NCM/Gr full-cells due to their high external applied pressures (~60 MPa) during cycling, for practical point of view, this behavior should be controlled by formation process. For example, when the unfavorable reaction including decomposition of SE (Figure 67) occurs at the interface, which exhibits higher volume expansion than graphite electrode ASLBs suffer from the contact loss, it will deteriorate the well-designed microstructure of electrodes.

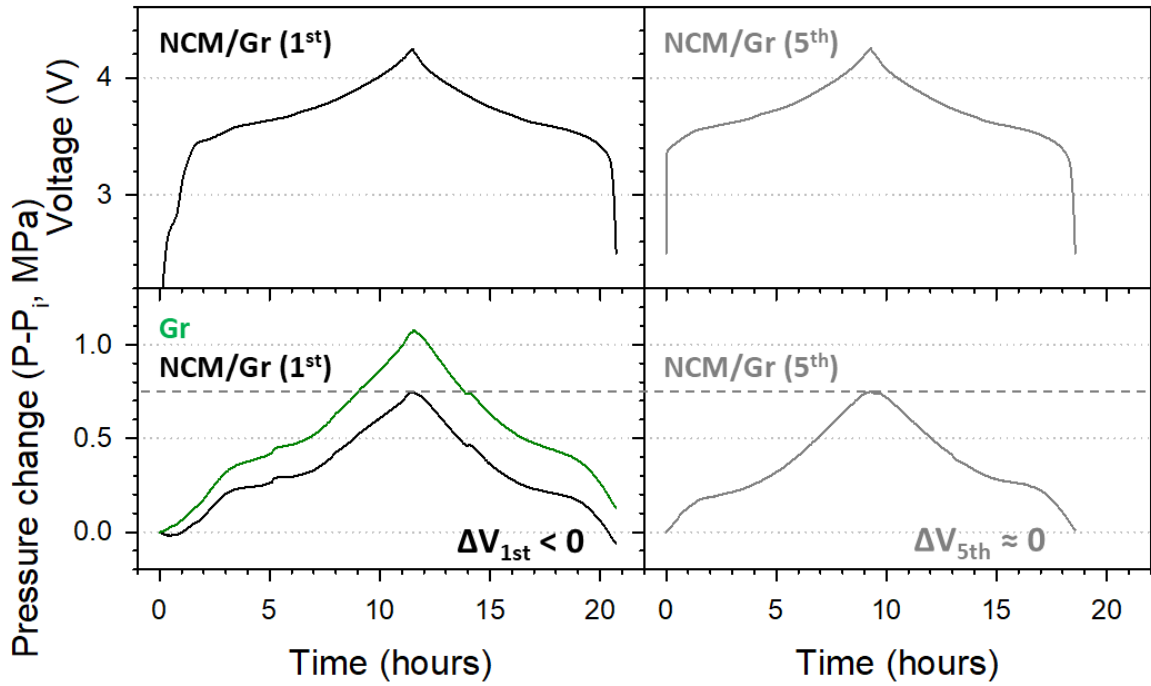


Figure 65. First and fifth voltage profiles of NCM/Gr full-cell with 0 wt% LGPS and the corresponding pressure change.

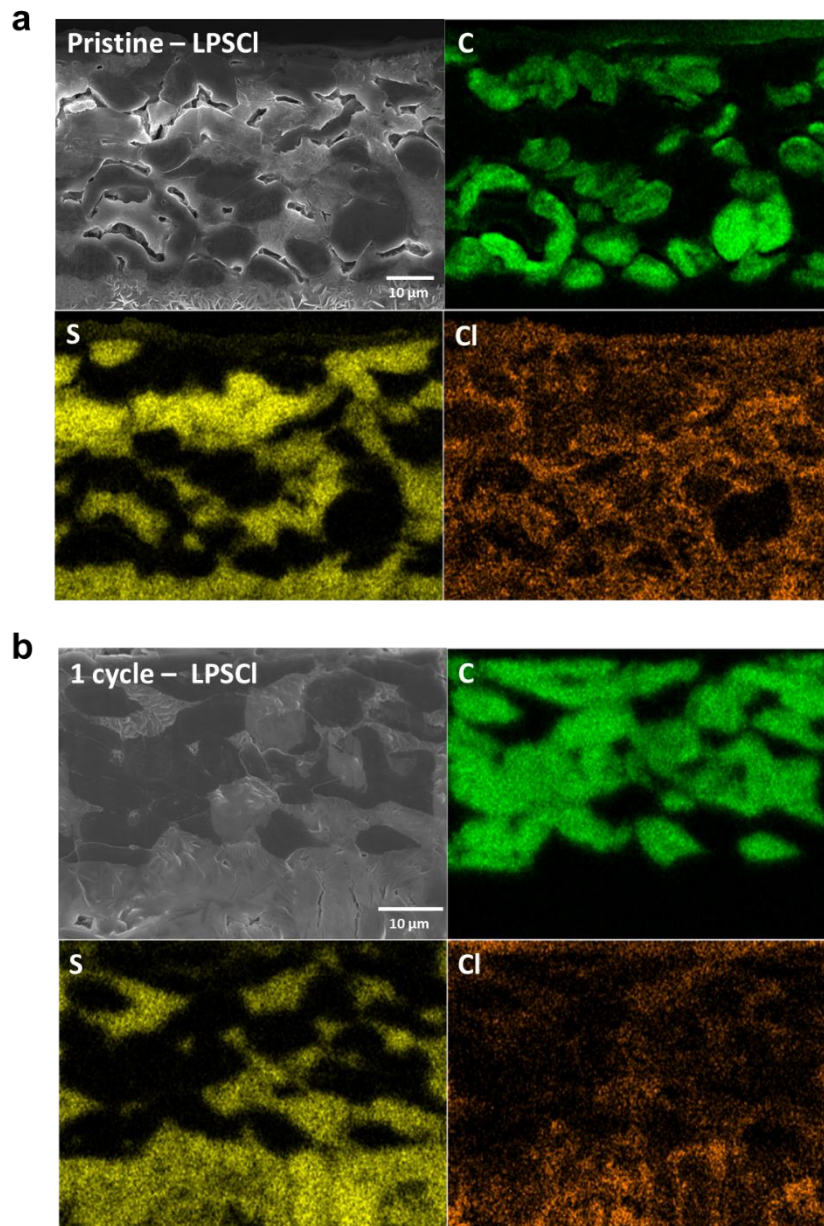


Figure 66. Cross-sectional FESEM images of Gr electrode with 0 wt% LGPS of a) before cycling and b) after 1 cycle.

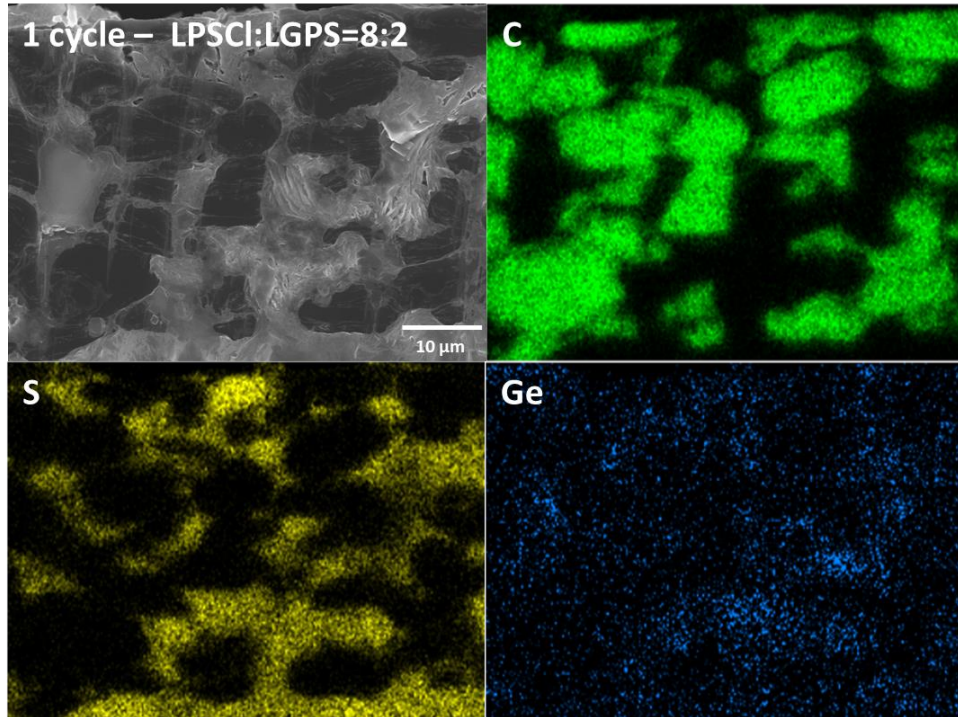


Figure 67. Cross-sectional FESEM images of Gr electrode with 20 wt% LGPS of after 1 cycle.

5. Conclusion

In this study, the fabrication of sheet-type electrodes and SE films and their diagnostic study for bulk-type all-solid-state lithium batteries were successfully demonstrated. The use of the powder form of sulfide SEs allows scalable fabrication of sheet-type electrodes and SE films, which is an ideal solution for practical applications. Thus, scalable fabrications of sheet-type electrodes and SE-films were demonstrated using polymeric binders and porous membranes. Moreover, their electrochemical performances of SE-films, dry- and slurry-mixed electrodes were systematically investigated. However, the presence of polymeric binders and porous membranes, which are ionically blocking regions, led to the slight decrease of the electrochemical performances due to poorer ionic contacts between active materials and SEs. Nevertheless, as the scalable fabrication using polymers is considered as ideal solution for practical ASLBs, these results provide a new route for the development of practical ASLBs.

As a groundwork for the development of electrochemical test protocols for ASLBs, a novel bulk-type all-solid-state three-electrode cell and pressure monitoring in operating cells were demonstrated successfully. For Sn/Li–In half-cells, it was clearly revealed that the overall capacity was limited by the Li–In CEs, not by the Sn WEs. Lithiation (discharge) of Sn was ended by the impeded Li^+ movement by the formation of Li-depleted insulating In layers at the interface between SE layer and Li–In CEs. As this problem was solved by the percolation with sulfide SEs (Li–In–SE CEs), it served as a reliable test protocol for all-solid-state half-cells. Moreover, for the case of NCM/Gr full-cells, the interfacial behavior for NCM/Gr full-cells was investigated. However, unfortunately, the observation of ISC behaviors by the penetrating growth of Li metal for Li-metal-free all-solid-state full-cells remained as a serious technical challenge in the future. By means of monitoring pressure changes, the SOC estimation of electrodes in all-solid-state batteries was successfully demonstrated. Also, the results of initial pressure changes imply that the formation process for all-solid-state technology could be developed in terms of rearrangement of particles in electrodes from for practical applications.

The as-developed electrochemical test protocols in this work will serve as a reliable platform for the interpretation of performances of complex interfacial chemistries and behaviors. Also, they provide new insight into the design of materials, electrodes and battery architectures for in-depth all-solid-state technology.

References

1. Tarascon, J. M.; Armand, M., Issues and challenges facing rechargeable lithium batteries. *Nature* **2001**, *414*, 359.
2. Goodenough, J. B.; Kim, Y., Challenges for Rechargeable Li Batteries. *Chemistry of Materials* **2010**, *22* (3), 587-603.
3. Etacheri, V.; Marom, R.; Elazari, R.; Salitra, G.; Aurbach, D., Challenges in the development of advanced Li-ion batteries: a review. *Energy & Environmental Science* **2011**, *4* (9), 3243-3262.
4. Jeong, G.; Kim, Y. U.; Kim, H.; Kim, Y. J.; Sohn, H. J., Prospective materials and applications for Li secondary batteries. *Energy & Environmental Science* **2011**, *4* (6), 1986-2002.
5. Xu, K., Nonaqueous liquid electrolytes for lithium-based rechargeable batteries. *Chem Rev* **2004**, *104* (10), 4303-417.
6. Arora, P.; Zhang, Z., Battery Separators. *Chemical Reviews* **2004**, *104* (10), 4419-4462.
7. Jung, Y. S.; Oh, D. Y.; Nam, Y. J.; Park, K. H., Issues and Challenges for Bulk-Type All-Solid-State Rechargeable Lithium Batteries using Sulfide Solid Electrolytes. *Israel Journal of Chemistry* **2015**, *55* (5), 472-485.
8. Park, K. H.; Bai, Q.; Kim, D. H.; Oh, D. Y.; Zhu, Y.; Mo, Y.; Jung, Y. S., Design Strategies, Practical Considerations, and New Solution Processes of Sulfide Solid Electrolytes for All-Solid-State Batteries. *Advanced Energy Materials* **2018**, *8* (18), 1800035.
9. Janek, J.; Zeier, W. G., A solid future for battery development. *Nature Energy* **2016**, *1*, 16141.
10. Mao, Z.; Farkhondeh, M.; Pritzker, M.; Fowler, M.; Chen, Z., Calendar Aging and Gas Generation in Commercial Graphite/NMC-LMO Lithium-Ion Pouch Cell. *Journal of The Electrochemical Society* **2017**, *164* (14), A3469-A3483.
11. Finegan, D. P.; Scheel, M.; Robinson, J. B.; Tjaden, B.; Hunt, I.; Mason, T. J.; Millichamp, J.; Di Michiel, M.; Offer, G. J.; Hinds, G.; Brett, D. J. L.; Shearing, P. R., In-operando high-speed tomography of lithium-ion batteries during thermal runaway. *Nature communications* **2015**, *6*, 6924.
12. Jung, Y. S.; Cavanagh, A. S.; Gedvilas, L.; Widjonarko, N. E.; Scott, I. D.; Lee, S.-H.; Kim, G.-H.; George, S. M.; Dillon, A. C., Improved Functionality of Lithium-Ion Batteries Enabled by Atomic Layer Deposition on the Porous Microstructure of Polymer Separators and Coating Electrodes. *Advanced Energy Materials* **2012**, *2* (8), 1022-1027.

13. Wu, H.; Zhuo, D.; Kong, D.; Cui, Y., Improving battery safety by early detection of internal shorting with a bifunctional separator. *Nature communications* **2014**, *5*, 5193.
14. Kamaya, N.; Homma, K.; Yamakawa, Y.; Hirayama, M.; Kanno, R.; Yonemura, M.; Kamiyama, T.; Kato, Y.; Hama, S.; Kawamoto, K.; Mitsui, A., A lithium superionic conductor. *Nature materials* **2011**, *10*, 682.
15. Kato, Y.; Hori, S.; Saito, T.; Suzuki, K.; Hirayama, M.; Mitsui, A.; Yonemura, M.; Iba, H.; Kanno, R., High-power all-solid-state batteries using sulfide superionic conductors. *Nature Energy* **2016**, *1*, 16030.
16. Wang, Y. G.; He, P.; Zhou, H. S., Olivine LiFePO₄: development and future. *Energy & Environmental Science* **2011**, *4* (3), 805-817.
17. Abe, T.; Fukuda, H.; Iriyama, Y.; Ogumi, Z., Solvated Li-Ion Transfer at Interface Between Graphite and Electrolyte. *Journal of The Electrochemical Society* **2004**, *151* (8), A1120-A1123.
18. Chiku, M.; Tsujiwaki, W.; Higuchi, E.; Inoue, H., Microelectrode Studies on Kinetics of Charge Transfer at an Interface of Li Metal and Li₂S-P₂S₅ Solid Electrolytes. *Electrochemistry* **2012**, *80* (10), 740-742.
19. Wang, B.; Bates, J. B.; Hart, F. X.; Sales, B. C.; Zuhr, R. A.; Robertson, J. D., Characterization of thin-film rechargeable lithium batteries with lithium cobalt oxide cathodes. *Journal of the Electrochemical Society* **1996**, *143* (10), 3203-3213.
20. Bates, J. B.; Dudney, N. J.; Neudecker, B.; Ueda, A.; Evans, C. D., Thin-film lithium and lithium-ion batteries. *Solid State Ionics* **2000**, *135* (1), 33-45.
21. Garbayo, I.; Struzik, M.; Bowman, W. J.; Pfenninger, R.; Stilp, E.; Rupp, J. L. M., Glass-Type Polyamorphism in Li-Garnet Thin Film Solid State Battery Conductors. *Advanced Energy Materials* **2018**, *8* (12), 1702265.
22. Patil, A.; Patil, V.; Wook Shin, D.; Choi, J.-W.; Paik, D.-S.; Yoon, S.-J., Issue and challenges facing rechargeable thin film lithium batteries. *Materials Research Bulletin* **2008**, *43* (8), 1913-1942.
23. Oh, D. Y.; Nam, Y. J.; Park, K. H.; Jung, S. H.; Cho, S.-J.; Kim, Y. K.; Lee, Y.-G.; Lee, S.-Y.; Jung, Y. S., Excellent Compatibility of Solvate Ionic Liquids with Sulfide Solid Electrolytes: Toward Favorable Ionic Contacts in Bulk-Type All-Solid-State Lithium-Ion Batteries. *Advanced Energy Materials* **2015**, *5* (22), 1500865.
24. Sakuda, A.; Hayashi, A.; Tatsumisago, M., Sulfide solid electrolyte with favorable mechanical property for all-solid-state lithium battery. *Scientific reports* **2013**, *3*, 2261.

25. Oh, D. Y.; Kim, D. H.; Jung, S. H.; Han, J.-G.; Choi, N.-S.; Jung, Y. S., Single-step wet-chemical fabrication of sheet-type electrodes from solid-electrolyte precursors for all-solid-state lithium-ion batteries. *Journal of Materials Chemistry A* **2017**, *5* (39), 20771-20779.
26. Park, K. H.; Oh, D. Y.; Choi, Y. E.; Nam, Y. J.; Han, L.; Kim, J.-Y.; Xin, H.; Lin, F.; Oh, S. M.; Jung, Y. S., Solution-Processable Glass LiI-Li₄SnS₄ Superionic Conductors for All-Solid-State Li-Ion Batteries. *Advanced Materials* **2016**, *28* (9), 1874-1883.
27. Kim, D. H.; Oh, D. Y.; Park, K. H.; Choi, Y. E.; Nam, Y. J.; Lee, H. A.; Lee, S.-M.; Jung, Y. S., Infiltration of Solution-Processable Solid Electrolytes into Conventional Li-Ion-Battery Electrodes for All-Solid-State Li-Ion Batteries. *Nano Letters* **2017**, *17* (5), 3013-3020.
28. Mizuno, F.; Hayashi, A.; Tadanaga, K.; Tatsumisago, M., Effects of Conductive Additives in Composite Positive Electrodes on Charge-Discharge Behaviors of All-Solid-State Lithium Secondary Batteries. *Journal of The Electrochemical Society* **2005**, *152* (8), A1499-A1503.
29. Yamamoto, M.; Terauchi, Y.; Sakuda, A.; Takahashi, M., Binder-free sheet-type all-solid-state batteries with enhanced rate capabilities and high energy densities. *Scientific reports* **2018**, *8* (1), 1212.
30. Stramare, S.; Thangadurai, V.; Weppner, W., Lithium Lanthanum Titanates: A Review. *Chemistry of Materials* **2003**, *15* (21), 3974-3990.
31. Aono, H.; Sugimoto, E.; Sadaoka, Y.; Imanaka, N.; Adachi, G.-y., Ionic Conductivity of the Lithium Titanium Phosphate (Li_{1+x}M_xTi_{2-x}(PO₄)₃, M = Al, Sc, Y, and La) Systems. *Journal of The Electrochemical Society* **1989**, *136* (2), 590-591.
32. Murugan, R.; Thangadurai, V.; Weppner, W., Fast lithium ion conduction in garnet-type Li₇La₃Zr₂O₁₂. *Angewandte Chemie* **2007**, *46* (41), 7778-7781.
33. Kotobuki, M.; Munakata, H.; Kanamura, K.; Sato, Y.; Yoshida, T., Compatibility of Li₇La₃Zr₂O₁₂ Solid Electrolyte to All-Solid-State Battery Using Li Metal Anode. *Journal of The Electrochemical Society* **2010**, *157* (10), A1076-A1079.
34. Kim, K. H.; Iriyama, Y.; Yamamoto, K.; Kumazaki, S.; Asaka, T.; Tanabe, K.; Fisher, C. A. J.; Hirayama, T.; Murugan, R.; Ogumi, Z., Characterization of the interface between LiCoO₂ and Li₇La₃Zr₂O₁₂ in an all-solid-state rechargeable lithium battery. *Journal of Power Sources* **2011**, *196* (2), 764-767.
35. Hayashi, A.; Minami, K.; Mizuno, F.; Tatsumisago, M., Formation of Li⁺ superionic crystals from the Li₂S-P₂S₅ melt-quenched glasses. *Journal of Materials Science* **2008**, *43*, 1885.
36. Kanno, R.; Murayama, M., Lithium Ionic Conductor Thio-LISICON. *Journal of The*

Electrochemical Society **2001**, *148* (7), A742-A746.

37. Deiseroth, H. J.; Kong, S. T.; Eckert, H.; Vannahme, J.; Reiner, C.; Zaiss, T.; Schlosser, M., $\text{Li}_6\text{PS}_5\text{X}$: a class of crystalline Li-rich solids with an unusually high Li^+ mobility. *Angewandte Chemie* **2008**, *47* (4), 755-758.
38. Boulineau, S.; Courty, M.; Tarascon, J.-M.; Viallet, V., Mechanochemical synthesis of Li-argyrodite $\text{Li}_6\text{PS}_5\text{X}$ ($\text{X}=\text{Cl}, \text{Br}, \text{I}$) as sulfur-based solid electrolytes for all solid state batteries application. *Solid State Ionics* **2012**, *221*, 1-5.
39. Muramatsu, H.; Hayashi, A.; Ohtomo, T.; Hama, S.; Tatsumisago, M., Structural change of $\text{Li}_2\text{S}-\text{P}_2\text{S}_5$ sulfide solid electrolytes in the atmosphere. *Solid State Ionics* **2011**, *182* (1), 116-119.
40. Ohtomo, T.; Hayashi, A.; Tatsumisago, M.; Kawamoto, K., Suppression of H_2S gas generation from the $75\text{Li}_2\text{S}\cdot 25\text{P}_2\text{S}_5$ glass electrolyte by additives. *Journal of Materials Science* **2013**, *48* (11), 4137-4142.
41. Kanno, R.; Hata, T.; Kawamoto, Y.; Irie, M., Synthesis of a new lithium ionic conductor, thio-LISICON–lithium germanium sulfide system. *Solid State Ionics* **2000**, *137*, 97-104.
42. Kim, Y.; Saienga, J.; Martin, S. W., Anomalous Ionic Conductivity Increase in $\text{Li}_2\text{S} + \text{GeS}_2 + \text{GeO}_2$ Glasses. *The Journal of Physical Chemistry B* **2006**, *110* (33), 16318-16325.
43. Hori, S.; Kato, M.; Suzuki, K.; Hirayama, M.; Kato, Y.; Kanno, R.; Sprenkle, V., Phase Diagram of the Li_4GeS_4 - Li_3PS_4 Quasi-Binary System Containing the Superionic Conductor $\text{Li}_{10}\text{GeP}_2\text{S}_{12}$. *Journal of the American Ceramic Society* **2015**, *98* (10), 3352-3360.
44. Mo, Y.; Ong, S. P.; Ceder, G., First Principles Study of the $\text{Li}_{10}\text{GeP}_2\text{S}_{12}$ Lithium Super Ionic Conductor Material. *Chemistry of Materials* **2011**, *24* (1), 15-17.
45. Ong, S. P.; Mo, Y.; Richards, W. D.; Miara, L.; Lee, H. S.; Ceder, G., Phase stability, electrochemical stability and ionic conductivity of the $\text{Li}_{10\pm 1}\text{MP}_2\text{X}_{12}$ ($\text{M} = \text{Ge}, \text{Si}, \text{Sn}, \text{Al}$ or P , and $\text{X} = \text{O}, \text{S}$ or Se) family of superionic conductors. *Energy Environ. Sci.* **2013**, *6* (1), 148-156.
46. Wang, Y.; Richards, W. D.; Ong, S. P.; Miara, L. J.; Kim, J. C.; Mo, Y.; Ceder, G., Design principles for solid-state lithium superionic conductors. *Nature materials* **2015**, *14*, 1026.
47. Zhu, Y.; He, X.; Mo, Y., Strategies Based on Nitride Materials Chemistry to Stabilize Li Metal Anode. *Advanced Science* **2017**, *4* (8), 1600517.
48. Adams, S.; Prasada Rao, R., Structural requirements for fast lithium ion migration in $\text{Li}_{10}\text{GeP}_2\text{S}_{12}$. *Journal of Materials Chemistry* **2012**, *22* (16), 7687-7691.

49. Sakuda, A.; Hayashi, A.; Ohtomo, T.; Hama, S.; Tatsumisago, M., LiCoO₂ Electrode Particles Coated with Li₂S–P₂S₅ Solid Electrolyte for All-Solid-State Batteries. *Electrochemical and Solid-State Letters* **2010**, *13* (6), A73-A75.
50. Teragawa, S.; Aso, K.; Tadanaga, K.; Hayashi, A.; Tatsumisago, M., Liquid-phase synthesis of a Li₃PS₄ solid electrolyte using N-methylformamide for all-solid-state lithium batteries. *Journal of Materials Chemistry A* **2014**, *2* (14), 5095-5099.
51. Yubuchi, S.; Teragawa, S.; Aso, K.; Tadanaga, K.; Hayashi, A.; Tatsumisago, M., Preparation of high lithium-ion conducting Li₆PS₅Cl solid electrolyte from ethanol solution for all-solid-state lithium batteries. *Journal of Power Sources* **2015**, *293*, 941-945.
52. Choi, Y. E.; Park, K. H.; Kim, D. H.; Oh, D. Y.; Kwak, H.; Lee, Y.-G.; Jung, Y. S., Coatable Li₄SnS₄ Solid Electrolytes Prepared from Aqueous Solutions for All-Solid-State Lithium-Ion Batteries. *Chemosuschem* **2017**, *10* (12), 2605-2611.
53. Richards, W. D.; Miara, L. J.; Wang, Y.; Kim, J. C.; Ceder, G., Interface Stability in Solid-State Batteries. *Chemistry of Materials* **2016**, *28* (1), 266-273.
54. Zhu, Y.; He, X.; Mo, Y., First principles study on electrochemical and chemical stability of solid electrolyte–electrode interfaces in all-solid-state Li-ion batteries. *Journal of Materials Chemistry A* **2016**, *4* (9), 3253-3266.
55. Shin, B. R.; Nam, Y. J.; Oh, D. Y.; Kim, D. H.; Kim, J. W.; Jung, Y. S., Comparative Study of TiS₂/Li-In All-Solid-State Lithium Batteries Using Glass-Ceramic Li₃PS₄ and Li₁₀GeP₂S₁₂ Solid Electrolytes. *Electrochimica Acta* **2014**, *146*, 395-402.
56. Jung, S. H.; Oh, K.; Nam, Y. J.; Oh, D. Y.; Brüner, P.; Kang, K.; Jung, Y. S., Li₃BO₃-Li₂CO₃: Rationally Designed Buffering Phase for Sulfide All-Solid-State Li-Ion Batteries. *Chemistry of Materials* **2018**, *30* (22), 8190-8200.
57. Woo, J. H.; Trevey, J. E.; Cavanagh, A. S.; Choi, Y. S.; Kim, S. C.; George, S. M.; Oh, K. H.; Lee, S.-H., Nanoscale Interface Modification of LiCoO₂ by Al₂O₃ Atomic Layer Deposition for Solid-State Li Batteries. *Journal of the Electrochemical Society* **2012**, *159* (7), A1120-A1124.
58. Sakuda, A.; Hayashi, A.; Tatsumisago, M., Interfacial Observation between LiCoO₂ Electrode and Li₂S–P₂S₅ Solid Electrolytes of All-Solid-State Lithium Secondary Batteries Using Transmission Electron Microscopy. *Chemistry of Materials* **2010**, *22* (3), 949-956.
59. Ohta, N.; Takada, K.; Sakaguchi, I.; Zhang, L.; Ma, R.; Fukuda, K.; Osada, M.; Sasaki, T., LiNbO₃-coated LiCoO₂ as cathode material for all solid-state lithium secondary batteries.

Electrochemistry Communications **2007**, *9* (7), 1486-1490.

60. Ohta, N.; Takada, K.; Zhang, L. Q.; Ma, R. Z.; Osada, M.; Sasaki, T., Enhancement of the high-rate capability of solid-state lithium batteries by nanoscale interfacial modification. *Advanced Materials* **2006**, *18* (17), 2226-2229.
61. Okada, K.; Machida, N.; Naito, M.; Shigematsu, T.; Ito, S.; Fujiki, S.; Nakano, M.; Aihara, Y., Preparation and electrochemical properties of LiAlO₂-coated Li(Ni_{1/3}Mn_{1/3}Co_{1/3})O₂ for all-solid-state batteries. *Solid State Ionics* **2014**, *255*, 120-127.
62. Woo, J. H.; Travis, J. J.; George, S. M.; Lee, S.-H., Utilization of Al₂O₃ Atomic Layer Deposition for Li Ion Pathways in Solid State Li Batteries. *Journal of The Electrochemical Society* **2015**, *162* (3), A344-A349.
63. Ito, Y.; Sakurai, Y.; Yubuchi, S.; Sakuda, A.; Hayashi, A.; Tatsumisago, M., Application of LiCoO₂ Particles Coated with Lithium Ortho-Oxosalt Thin Films to Sulfide-Type All-Solid-State Lithium Batteries. *Journal of The Electrochemical Society* **2015**, *162* (8), A1610-A1616.
64. Ito, S.; Fujiki, S.; Yamada, T.; Aihara, Y.; Park, Y.; Kim, T. Y.; Baek, S.-W.; Lee, J.-M.; Doo, S.; Machida, N., A rocking chair type all-solid-state lithium ion battery adopting Li₂O-ZrO₂ coated LiNi_{0.8}Co_{0.15}Al_{0.05}O₂ and a sulfide based electrolyte. *Journal of Power Sources* **2014**, *248*, 943-950.
65. Sakuda, A.; Kuratani, K.; Yamamoto, M.; Takahashi, M.; Takeuchi, T.; Kobayashi, H., All-Solid-State Battery Electrode Sheets Prepared by a Slurry Coating Process. *Journal of the Electrochemical Society* **2017**, *64* (12), A2474-A2478.
66. Zhang, W.; Schroder, D.; Arlt, T.; Manke, I.; Koerver, R.; Pinedo, R.; Weber, D. A.; Sann, J.; Zeier, W. G.; Janek, J., (Electro)chemical expansion during cycling: monitoring the pressure changes in operating solid-state lithium batteries. *Journal of Materials Chemistry A* **2017**, *5* (20), 9929-9936.
67. Koerver, R.; Zhang, W.; de Biasi, L.; Schweidler, S.; Kondrakov, A.; Kolling, S.; Brezesinski, T.; Hartmann, P.; Zeier, W.; Janek, J., Chemo-mechanical expansion of lithium electrode materials - On the route to mechanically optimized all-solid-state batteries. *Energy & Environmental Science* **2018**, *11* (8), 2142-2158.
68. Bartsch, T.; Strauss, F.; Hatsukade, T.; Schiele, A.; Kim, A. Y.; Hartmann, P.; Janek, J.; Brezesinski, T., Gas Evolution in All-Solid-State Battery Cells. *ACS Energy Letters* **2018**, *3* (10), 2539-2543.
69. Jung, Y. S.; Cavanagh, A. S.; Riley, L. A.; Kang, S.-H.; Dillon, A. C.; Groner, M. D.; George, S. M.; Lee, S.-H., Ultrathin Direct Atomic Layer Deposition on Composite Electrodes for Highly

Durable and Safe Li-Ion Batteries. *Advanced Materials* **2010**, 22 (19), 2172-2176.

70. Bruce, P. G., *Solid State Electrochemistry*. Cambridge University Press: Cambridge, **1994**.
71. Ren, Y.; Chen, K.; Chen, R.; Liu, T.; Zhang, Y.; Nan, C.-W., Oxide Electrolytes for Lithium Batteries. *Journal of the American Ceramic Society* **2015**, 98 (12), 3603-3623.
72. Mizuno, F.; Hayashi, A.; Tadanaga, K.; Tatsumisago, M., New, highly ion-conductive crystals precipitated from $\text{Li}_2\text{S-P}_2\text{S}_5$ glasses. *Advanced Materials* **2005**, 17 (7), 918-921.
73. Homma, K.; Yonemura, M.; Kobayashi, T.; Nagao, M.; Hirayama, M.; Kanno, R., Crystal structure and phase transitions of the lithium ionic conductor Li_3PS_4 . *Solid State Ionics* **2011**, 182 (1), 53-58.
74. Dietrich, C.; Weber, D. A.; Sedlmaier, S. J.; Indris, S.; Culver, S. P.; Walter, D.; Janek, J.; Zeier, W. G., Lithium ion conductivity in $\text{Li}_2\text{S-P}_2\text{S}_5$ glasses – building units and local structure evolution during the crystallization of superionic conductors Li_3PS_4 , $\text{Li}_7\text{P}_3\text{S}_{11}$ and $\text{Li}_4\text{P}_2\text{S}_7$. *Journal of Materials Chemistry A* **2017**, 5 (34), 18111-18119.
75. Dietrich, C.; Sadowski, M.; Sicolo, S.; Weber, D. A.; Sedlmaier, S. J.; Weldert, K. S.; Indris, S.; Albe, K.; Janek, J.; Zeier, W. G., Local Structural Investigations, Defect Formation, and Ionic Conductivity of the Lithium Ionic Conductor $\text{Li}_4\text{P}_2\text{S}_6$. *Chemistry of Materials* **2016**, 28 (23), 8764-8773.
76. Richards, W. D.; Wang, Y.; Miara, L. J.; Kim, J. C.; Ceder, G., Design of $\text{Li}_{1+2x}\text{Zn}_{1-x}\text{PS}_4$, a new lithium ion conductor. *Energy & Environmental Science* **2016**, 9 (10), 3272-3278.
77. Kraft, M. A.; Culver, S. P.; Calderon, M.; Böcher, F.; Krauskopf, T.; Senyshyn, A.; Dietrich, C.; Zevalkink, A.; Janek, J.; Zeier, W. G., Influence of Lattice Polarizability on the Ionic Conductivity in the Lithium Superionic Argyrodites $\text{Li}_6\text{PS}_5\text{X}$ (X = Cl, Br, I). *Journal of the American Chemical Society* **2017**, 139 (31), 10909-10918.
78. Kraft, M. A.; Ohno, S.; Zinkevich, T.; Koerver, R.; Culver, S. P.; Fuchs, T.; Senyshyn, A.; Indris, S.; Morgan, B. J.; Zeier, W. G., Inducing High Ionic Conductivity in the Lithium Superionic Argyrodites $\text{Li}_{6+x}\text{P}_{1-x}\text{Ge}_x\text{S}_5\text{I}$ for All-Solid-State Batteries. *Journal of the American Chemical Society* **2018**, 140 (47), 16330-16339.
79. Ohtomo, T.; Hayashi, A.; Tatsumisago, M.; Kawamoto, K., All-solid-state batteries with $\text{Li}_2\text{O-Li}_2\text{S-P}_2\text{S}_5$ glass electrolytes synthesized by two-step mechanical milling. *Journal of Solid State Electrochemistry* **2013**, 17 (10), 2551-2557.
80. Hayashi, A.; Muramatsu, H.; Ohtomo, T.; Hama, S.; Tatsumisago, M., Improvement of chemical stability of Li_3PS_4 glass electrolytes by adding M_xO_y (M = Fe, Zn, and Bi) nanoparticles.

Journal of Materials Chemistry A **2013**, *1* (21), 6320-6326.

81. Tao, Y.; Chen, S.; Liu, D.; Peng, G.; Yao, X.; Xu, X., Lithium Superionic Conducting Oxy sulfide Solid Electrolyte with Excellent Stability against Lithium Metal for All-Solid-State Cells. *Journal of The Electrochemical Society* **2016**, *163* (2), A96-A101.
82. Mo, S.; Lu, P.; Ding, F.; Xu, Z.; Liu, J.; Liu, X.; Xu, Q., High-temperature performance of all-solid-state battery assembled with 95(0.7Li₂S-0.3P₂S₅)-5Li₃PO₄ glass electrolyte. *Solid State Ionics* **2016**, *296*, 37-41.
83. Auvergniot, J.; Cassel, A.; Ledeuil, J. B.; Viallet, V.; Seznec, V.; Dedryvere, R., Interface Stability of Argyrodite Li₆PS₅Cl toward LiCoO₂, LiNi_{1/3}Co_{1/3}Mn_{1/3}O₂, and LiMn₂O₄ in Bulk All-Solid-State Batteries. *Chemistry of Materials* **2017**, *29* (9), 3883-3890.
84. Auvergniot, J.; Cassel, A.; Foix, D.; Viallet, V.; Seznec, V.; Dedryvere, R., Redox activity of argyrodite Li₆PS₅Cl electrolyte in all-solid-state Li-ion battery: An XPS study. *Solid State Ionics* **2017**, *300*, 78-85.
85. Zhang, W.; Richter, F. H.; Culver, S. P.; Leichtweiss, T.; Lozano, J. G.; Dietrich, C.; Bruce, P. G.; Zeier, W. G.; Janek, J., Degradation Mechanisms at the Li₁₀GeP₂S₁₂/LiCoO₂ Cathode Interface in an All-Solid-State Lithium-Ion Battery. *ACS Applied Materials & Interfaces* **2018**, *10* (26), 22226-22236.
86. Zhang, W.; Leichtweiß, T.; Culver, S. P.; Koerver, R.; Das, D.; Weber, D. A.; Zeier, W. G.; Janek, J., The Detrimental Effects of Carbon Additives in Li₁₀GeP₂S₁₂-Based Solid-State Batteries. *ACS Applied Materials & Interfaces* **2017**, *9* (41), 35888-35896.
87. Park, K. H.; Kim, D. H.; Kwak, H.; Jung, S. H.; Lee, H.-J.; Banerjee, A.; Lee, J. H.; Jung, Y. S., Solution-derived glass-ceramic NaI-Na₃SbS₄ superionic conductors for all-solid-state Na-ion batteries. *Journal of Materials Chemistry A* **2018**, *6* (35), 17192-17200.
88. Kim, T. W.; Park, K. H.; Choi, Y. E.; Lee, J. Y.; Jung, Y. S., Aqueous-solution synthesis of Na₃SbS₄ solid electrolytes for all-solid-state Na-ion batteries. *Journal of Materials Chemistry A* **2018**, *6* (3), 840-844.
89. Zheng, G.; Lee, S. W.; Liang, Z.; Lee, H. W.; Yan, K.; Yao, H.; Wang, H.; Li, W.; Chu, S.; Cui, Y., Interconnected hollow carbon nanospheres for stable lithium metal anodes. *Nat Nanotechnol* **2014**, *9* (8), 618.
90. Qian, J.; Henderson, W. A.; Xu, W.; Bhattacharya, P.; Engelhard, M.; Borodin, O.; Zhang, J. G., High rate and stable cycling of lithium metal anode. *Nature communications* **2015**, *6*, 6362.

91. Liu, Y.; Lin, D.; Yuen, P. Y.; Liu, K.; Xie, J.; Dauskardt, R. H.; Cui, Y., An Artificial Solid Electrolyte Interphase with High Li-Ion Conductivity, Mechanical Strength, and Flexibility for Stable Lithium Metal Anodes. *Adv Mater* **2017**, *29* (10), 1605531.
92. Lu, Y.; Tu, Z.; Archer, L. A., Stable lithium electrodeposition in liquid and nanoporous solid electrolytes. *Nature materials* **2014**, *13* (10), 961.
93. Yan, K.; Lu, Z.; Lee, H.-W.; Xiong, F.; Hsu, P.-C.; Li, Y.; Zhao, J.; Chu, S.; Cui, Y., Selective deposition and stable encapsulation of lithium through heterogeneous seeded growth. *Nature Energy* **2016**, *1*, 16010.
94. Lin, D.; Liu, Y.; Cui, Y., Reviving the lithium metal anode for high-energy batteries. *Nat Nanotechnol* **2017**, *12* (3), 194-206.
95. Lu, D.; Shao, Y.; Lozano, T.; Bennett, W. D.; Graff, G. L.; Polzin, B.; Zhang, J.; Engelhard, M. H.; Saenz, N. T.; Henderson, W. A.; Bhattacharya, P.; Liu, J.; Xiao, J., Failure Mechanism for Fast-Charged Lithium Metal Batteries with Liquid Electrolytes. *Advanced Energy Materials* **2015**, *5* (3), 1400993.
96. Liu, Y. D.; Liu, Q.; Xin, L.; Liu, Y. Z.; Yang, F.; Stach, E. A.; Xie, J., Making Li-metal electrodes rechargeable by controlling the dendrite growth direction. *Nature Energy* **2017**, *2* (7), 17083.
97. Nagao, M.; Hayashi, A.; Tatsumisago, M.; Kanetsuku, T.; Tsuda, T.; Kuwabata, S., In situ SEM study of a lithium deposition and dissolution mechanism in a bulk-type solid-state cell with a $\text{Li}_2\text{S-P}_2\text{S}_5$ solid electrolyte. *Physical chemistry chemical physics : PCCP* **2013**, *15* (42), 18600-18606.
98. Porz, L.; Swamy, T.; Sheldon, B. W.; Rettenwander, D.; Fromling, T.; Thaman, H. L.; Berendts, S.; Uecker, R.; Carter, W. C.; Chiang, Y. M., Mechanism of Lithium Metal Penetration through Inorganic Solid Electrolytes. *Advanced Energy Materials* **2017**, *7* (20), 1701003.
99. Cheng, E. J.; Sharafi, A.; Sakamoto, J., Intergranular Li metal propagation through polycrystalline $\text{Li}_{6.25}\text{Al}_{0.25}\text{La}_3\text{Zr}_2\text{O}_{12}$ ceramic electrolyte. *Electrochimica Acta* **2017**, *223*, 85-91.
100. Sang, L. Z.; Haasch, R. T.; Gewirth, A. A.; Nuzzo, R. G., Evolution at the Solid Electrolyte/Gold Electrode Interface during Lithium Deposition and Stripping. *Chemistry of Materials* **2017**, *29* (7), 3029-3037.
101. Wenzel, S.; Randau, S.; Leichtweiß, T.; Weber, D. A.; Sann, J.; Zeier, W. G.; Janek, J., Direct Observation of the Interfacial Instability of the Fast Ionic Conductor $\text{Li}_{10}\text{GeP}_2\text{S}_{12}$ at the Lithium Metal Anode. *Chemistry of Materials* **2016**, *28* (7), 2400-2407.
102. Kato, A.; Kowada, H.; Deguchi, M.; Hotehama, C.; Hayashi, A.; Tatsumisago, M., XPS and

SEM analysis between Li/Li₃PS₄ interface with Au thin film for all-solid-state lithium batteries. *Solid State Ionics* **2018**, 322, 1-4.

103. Suyama, M.; Kato, A.; Sakuda, A.; Hayashi, A.; Tatsumisago, M., Lithium dissolution/deposition behavior with Li₃PS₄-LiI electrolyte for all-solid-state batteries operating at high temperatures. *Electrochimica Acta* **2018**, 286, 158-162.

104. Xu, R.; Han, F.; Ji, X.; Fan, X.; Tu, J.; Wang, C., Interface engineering of sulfide electrolytes for all-solid-state lithium batteries. *Nano Energy* **2018**, 53, 958-966.

105. Gao, Y.; Wang, D.; Li, Y.; Yu, Z.; Mallouk, T.; Wang, D., Salt-based organic-inorganic nanocomposites: towards a stable lithium metal/Li₁₀GeP₂S₁₂ solid electrolyte interface. *Angewandte Chemie International Edition* **2018**, 57 (41), 13608-13612.

106. Kato, A.; Suyama, M.; Hotehama, C.; Kowada, H.; Sakuda, A.; Hayashi, A.; Tatsumisago, M., High-Temperature Performance of All-Solid-State Lithium-Metal Batteries Having Li/Li₃PS₄ Interfaces Modified with Au Thin Films. *Journal of The Electrochemical Society* **2018**, 165 (9), A1950-A1954.

107. Nagao, M.; Hayashi, A.; Tatsumisago, M., Bulk-Type Lithium Metal Secondary Battery with Indium Thin Layer at Interface between Li Electrode and Li₂S-P₂S₅ Solid Electrolyte. *Electrochemistry* **2012**, 80 (10), 734-736.

108. Winter, M.; Wrodnigg, G. H.; Besenhard, J. O.; Biberacher, W.; Novák, P., Dilatometric Investigations of Graphite Electrodes in Nonaqueous Lithium Battery Electrolytes. *Journal of The Electrochemical Society* **2000**, 147 (7), 2427-2431.

109. Wuersig, A.; Scheifele, W.; Novák, P., CO₂ Gas Evolution on Cathode Materials for Lithium-Ion Batteries. *Journal of The Electrochemical Society* **2007**, 154 (5), A449-A454.

110. Wang, H.; Rus, E.; Sakuraba, T.; Kikuchi, J.; Kiya, Y.; Abruña, H. D., CO₂ and O₂ Evolution at High Voltage Cathode Materials of Li-Ion Batteries: A Differential Electrochemical Mass Spectrometry Study. *Analytical Chemistry* **2014**, 86 (13), 6197-6201.

111. Kondrakov, A. O.; Schmidt, A.; Xu, J.; Geßwein, H.; Mönig, R.; Hartmann, P.; Sommer, H.; Brezesinski, T.; Janek, J., Anisotropic Lattice Strain and Mechanical Degradation of High- and Low-Nickel NCM Cathode Materials for Li-Ion Batteries. *The Journal of Physical Chemistry C* **2017**, 121 (6), 3286-3294.

112. Sauerteig, D.; Ivanov, S.; Reinshagen, H.; Bund, A., Reversible and irreversible dilation of lithium-ion battery electrodes investigated by in-situ dilatometry. *Journal of Power Sources* **2017**, 342, 939-946.

113. Schweidler, S.; de Biasi, L.; Schiele, A.; Hartmann, P.; Brezesinski, T.; Janek, J., Volume Changes of Graphite Anodes Revisited: A Combined Operando X-ray Diffraction and In Situ Pressure Analysis Study. *The Journal of Physical Chemistry C* **2018**, *122* (16), 8829-8835.
114. Jung, Y. S.; Lee, K. T.; Kim, J. H.; Kwon, J. Y.; Oh, S. M., Thermo-electrochemical Activation of an In–Cu Intermetallic Electrode for the Anode in Lithium Secondary Batteries. *Advanced Functional Materials* **2008**, *18* (19), 3010-3017.
115. Whiteley, J. M.; Kim, J. W.; Kang, C. S.; Cho, J. S.; Oh, K. H.; Lee, S.-H., Tin Networked Electrode Providing Enhanced Volumetric Capacity and Pressureless Operation for All-Solid-State Li-Ion Batteries. *Journal of the Electrochemical Society* **2015**, *162* (4), A711-A715.
116. Whiteley, J. M.; Kim, J. W.; Piper, D. M.; Lee, S.-H., High-Capacity and Highly Reversible Silicon-Tin Hybrid Anode for Solid-State Lithium-Ion Batteries. *Journal of the Electrochemical Society* **2016**, *163* (2), A251-A254.
117. Trevey, J. E.; Rason, K. W.; Stoldt, C. R.; Lee, S.-H., Improved Performance of All-Solid-State Lithium-Ion Batteries Using Nanosilicon Active Material with Multiwalled-Carbon-Nanotubes as a Conductive Additive. *Electrochem Solid St* **2010**, *13* (11), A154-A157.
118. Piper, D. M.; Yersak, T. A.; Lee, S.-H., Effect of Compressive Stress on Electrochemical Performance of Silicon Anodes. *Journal of the Electrochemical Society* **2013**, *160* (1), A77-A81.
119. Yersak, T. A.; Son, S.-B.; Cho, J. S.; Suh, S.-S.; Kim, Y.-U.; Moon, J.-T.; Oh, K. H.; Lee, S.-H., An All-Solid-State Li-Ion Battery with a Pre-Lithiated Si-Ti-Ni Alloy Anode. *Journal of the Electrochemical Society* **2013**, *160* (9), A1497-A1501.
120. Dunlap, N. A.; Kim, S.; Jeong, J. J.; Oh, K. H.; Lee, S.-H., Simple and inexpensive coal-tar-pitch derived Si-C anode composite for all-solid-state Li-ion batteries. *Solid State Ionics* **2018**, *324*, 207-217.
121. Kato, A.; Yamamoto, M.; Sakuda, A.; Hayashi, A.; Tatsumisago, M., Mechanical Properties of $\text{Li}_2\text{S-P}_2\text{S}_5$ Glasses with Lithium Halides and Application in All-Solid-State Batteries. *ACS Applied Energy Materials* **2018**, *1* (3), 1002-1007.
122. Nagata, H.; Chikusa, Y., A lithium sulfur battery with high power density. *Journal of Power Sources* **2014**, *264*, 206-210.
123. Yersak, T. A.; Trevey, J. E.; Lee, S.-H., In situ lithiation of TiS_2 enabled by spontaneous decomposition of Li_3N . *Journal of Power Sources* **2011**, *196* (22), 9830-9834.
124. Benedetti-Pichler, A. A.; Cefola, M., Warder's method for the titration of carbonates. *Industrial*

& Engineering Chemistry Analytical Edition **1939**, *II* (6), 327-332.

125. Kuhn, A.; Kohler, J.; Lotsch, B. V., Single-crystal X-ray structure analysis of the superionic conductor $\text{Li}_{10}\text{GeP}_2\text{S}_{12}$. *Physical chemistry chemical physics : PCCP* **2013**, *15* (28), 11620-11622.

126. Shaju, K. M.; Subba Rao, G. V.; Chowdari, B. V. R., Influence of Li-Ion Kinetics in the Cathodic Performance of Layered $\text{Li}(\text{Ni}_{1/3}\text{Co}_{1/3}\text{Mn}_{1/3})\text{O}_2$. *Journal of The Electrochemical Society* **2004**, *151* (9), A1324-A1332.

127. Seol, J.-H.; Won, J.-H.; Yoon, K.-S.; Hong, Y. T.; Lee, S.-Y., SiO_2 nanoparticles-coated poly(paraphenylene terephthalamide) nonwovens as reinforcing porous substrates for proton-conducting, sulfonated poly(arylene ether sulfone)-impregnated composite membranes. *Solid State Ionics* **2011**, *190* (1), 30-37.

128. Kuhn, A.; Duppel, V.; Lotsch, B. V., Tetragonal $\text{Li}_{10}\text{GeP}_2\text{S}_{12}$ and Li_7GePS_8 - exploring the Li ion dynamics in LGPS Li electrolytes. *Energy & Environmental Science* **2013**, *6* (12), 3548-3552.

129. Lee, S.-Y.; Choi, K.-H.; Choi, W.-S.; Kwon, Y. H.; Jung, H.-R.; Shin, H.-C.; Kim, J. Y., Progress in flexible energy storage and conversion systems, with a focus on cable-type lithium-ion batteries. *Energy & Environmental Science* **2013**, *6* (8), 2414-2423.

130. Chen, Z.; Dahn, J. R., Improving the Capacity Retention of LiCoO_2 Cycled to 4.5 V by Heat-Treatment. *Electrochemical and Solid-State Letters* **2004**, *7* (1), A11-A14.

131. Liu, H. S.; Zhang, Z. R.; Gong, Z. L.; Yang, Y., Origin of Deterioration for LiNiO_2 Cathode Material during Storage in Air. *Electrochemical and Solid-State Letters* **2004**, *7* (7), A190-A193.

132. Mijung, N.; Lee, Y.; Cho, J., Water Adsorption and Storage Characteristics of Optimized LiCoO_2 and $\text{LiNi}_{1/3}\text{Co}_{1/3}\text{Mn}_{1/3}\text{O}_2$ Composite Cathode Material for Li-Ion Cells. *Journal of The Electrochemical Society* **2006**, *153* (5), A935-A940.

133. Ogihara, N.; Itou, Y.; Sasaki, T.; Takeuchi, Y., Impedance Spectroscopy Characterization of Porous Electrodes under Different Electrode Thickness Using a Symmetric Cell for High-Performance Lithium-Ion Batteries. *J Phys Chem C* **2015**, *119* (9), 4612-4619.

134. Koerver, R.; Aygun, I.; Leichtweiss, T.; Dietrich, C.; Zhang, W. B.; Binder, J. O.; Hartmann, P.; Zeier, W. G.; Janek, J., Capacity Fade in Solid-State Batteries: Interphase Formation and Chemomechanical Processes in Nickel-Rich Layered Oxide Cathodes and Lithium Thiophosphate Solid Electrolytes. *Chemistry of Materials* **2017**, *29* (13), 5574-5582.

135. Sun, Y.-K.; Chen, Z.; Noh, H.-J.; Lee, D.-J.; Jung, H.-G.; Ren, Y.; Wang, S.; Yoon, C. S.; Myung, S.-T.; Amine, K., Nanostructured high-energy cathode materials for advanced lithium batteries.

Nature materials **2012**, *11*, 942.

136. Lopez, C. F.; Jeevarajan, J. A.; Mukherjee, P. P., Experimental Analysis of Thermal Runaway and Propagation in Lithium-Ion Battery Modules. *Journal of The Electrochemical Society* **2015**, *162* (9), A1905-A1915.

137. Albertus, P.; Babinec, S.; Litzelman, S.; Newman, A., Status and challenges in enabling the lithium metal electrode for high-energy and low-cost rechargeable batteries. *Nature Energy* **2018**, *3* (1), 16.

138. Zhang, W.; Weber, D. A.; Weigand, H.; Arlt, T.; Manke, I.; Schroder, D.; Koerver, R.; Leichtweiss, T.; Hartmann, P.; Zeier, W. G.; Janek, J., Interfacial Processes and Influence of Composite Cathode Microstructure Controlling the Performance of All-Solid-State Lithium Batteries. *ACS Appl Mater Interfaces* **2017**, *9* (21), 17835-17845.

139. Jung, Y. S.; Lu, P.; Cavanagh, A. S.; Ban, C.; Kim, G.-H.; Lee, S.-H.; George, S. M.; Harris, S. J.; Dillon, A. C., Unexpected Improved Performance of ALD Coated LiCoO₂/Graphite Li-Ion Batteries. *Advanced Energy Materials* **2013**, *3* (2), 213-219.

140. Bhide, A.; Hofmann, J.; Katharina Durr, A.; Janek, J.; Adelhelm, P., Electrochemical stability of non-aqueous electrolytes for sodium-ion batteries and their compatibility with Na_{0.7}CoO₂. *Physical Chemistry Chemical Physics* **2014**, *16* (5), 1987-1998.

141. Yu, X.; Bates, J. B.; Jellison, G. E.; Hart, F. X., A Stable Thin-Film Lithium Electrolyte: Lithium Phosphorus Oxynitride. *Journal of The Electrochemical Society* **1997**, *144* (2), 524-532.

142. Arora, P.; Doyle, M.; White, R. E., Mathematical Modeling of the Lithium Deposition Overcharge Reaction in Lithium-Ion Batteries Using Carbon-Based Negative Electrodes. *Journal of The Electrochemical Society* **1999**, *146* (10), 3543-3553.

143. Uhlmann, C.; Illig, J.; Ender, M.; Schuster, R.; Ivers-Tiffée, E., In situ detection of lithium metal plating on graphite in experimental cells. *Journal of Power Sources* **2015**, *279*, 428-438.

144. Downie, L. E.; Krause, L. J.; Burns, J. C.; Jensen, L. D.; Chevrier, V. L.; Dahn, J. R., In Situ Detection of Lithium Plating on Graphite Electrodes by Electrochemical Calorimetry. *Journal of The Electrochemical Society* **2013**, *160* (4), A588-A594.

145. Tsai, C. L.; Roddatis, V.; Chandran, C. V.; Ma, Q.; Uhlenbruck, S.; Bram, M.; Heitjans, P.; Guillon, O., Li₇La₃Zr₂O₁₂ Interface Modification for Li Dendrite Prevention. *ACS Appl Mater Interfaces* **2016**, *8* (16), 10617-10626.

146. Crompton, K. R.; Landi, B. J., Opportunities for near zero volt storage of lithium ion batteries.

Energy & Environmental Science **2016**, 9 (7), 2219-2239.

147. Wang, P.; Li, P.; Yi, T.-F.; Yu, H.; Lin, X.; Qian, S.; Zhu, Y.-R.; Shui, M.; Shu, J., In-situ X-ray diffraction study on the structural reversibility of lithium nickel cobalt oxide in a broad electrochemical window of 1.35–4.3V. *Electrochimica Acta* **2016**, 190, 248-257.

148. Strauss, F.; Bartsch, T.; de Biasi, L.; Kim, A. Y.; Janek, J.; Hartmann, P.; Brezesinski, T., Impact of Cathode Material Particle Size on the Capacity of Bulk-Type All-Solid-State Batteries. *ACS Energy Letters* **2018**, 3, 992-996.

149. Xu, J.; Cao, B.; Chen, Z.; Zou, Z., An online state of charge estimation method with reduced prior battery testing information. *International Journal of Electrical Power & Energy Systems* **2014**, 63, 178-184.

150. Liu, X.; He, Y.; Zheng, X.; Zhang, J.; Zeng, G., A new state-of-charge estimation method for electric vehicle lithium-ion batteries based on multiple input parameter fitting model. *International Journal of Energy Research* **2017**, 41 (9), 1265-1276.

151. Xiong, R.; Cao, J.; Yu, Q.; He, H.; Sun, F., Critical Review on the Battery State of Charge Estimation Methods for Electric Vehicles. *IEEE Access* **2018**, 6, 1832-1843.

152. Reynier, Y.; Yazami, R.; Fultz, B., XRD evidence of macroscopic composition inhomogeneities in the graphite–lithium electrode. *Journal of Power Sources* **2007**, 165 (2), 616-619.

153. de Biasi, L.; Kondrakov, A. O.; Geßwein, H.; Brezesinski, T.; Hartmann, P.; Janek, J., Between Scylla and Charybdis: Balancing Among Structural Stability and Energy Density of Layered NCM Cathode Materials for Advanced Lithium-Ion Batteries. *The Journal of Physical Chemistry C* **2017**, 121 (47), 26163-26171.

Permission

* Chapter 4.1.1. is reproduced in part with permission of Y. J. Nam, S.-J. Cho, D. Y. Oh, J.-M. Lim, S. Y. Kim, J. H. Song, Y.-G. Lee, S.-Y. Lee, Y. S. Jung., "Bendable and Thin Sulfide Solid Electrolyte Film: A New Electrolyte Opportunity for Free-Standing and Stackable High-Energy All-Solid-State Lithium-Ion Batteries". Copyright 2015, Nano Letters



RightsLink®

Home

Account
Info

Help



ACS Publications
Most Trusted. Most Cited. Most Read.

Title:

Bendable and Thin Sulfide Solid Electrolyte Film: A New Electrolyte Opportunity for Free-Standing and Stackable High-Energy All-Solid-State Lithium-Ion Batteries

Logged in as:

Young Jin Nam

LOGOUT

Author: Young Jin Nam, Sung-Ju Cho, Dae Yang Oh, et al

Publication: Nano Letters

Publisher: American Chemical Society

Date: May 1, 2015

Copyright © 2015, American Chemical Society

PERMISSION/LICENSE IS GRANTED FOR YOUR ORDER AT NO CHARGE

This type of permission/license, instead of the standard Terms & Conditions, is sent to you because no fee is being charged for your order. Please note the following:

- Permission is granted for your request in both print and electronic formats, and translations.
- If figures and/or tables were requested, they may be adapted or used in part.
- Please print this page for your records and send a copy of it to your publisher/graduate school.
- Appropriate credit for the requested material should be given as follows: "Reprinted (adapted) with permission from (COMPLETE REFERENCE CITATION). Copyright (YEAR) American Chemical Society." Insert appropriate information in place of the capitalized words.
- One-time permission is granted only for the use specified in your request. No additional uses are granted (such as derivative works or other editions). For any other uses, please submit a new request.

BACK

CLOSE WINDOW

Copyright © 2018 Copyright Clearance Center, Inc. All Rights Reserved. [Privacy statement](#). [Terms and Conditions](#).
Comments? We would like to hear from you. E-mail us at customer@copyright.com

* Chapter 4.1.2. is reproduced in part with permission of Y. J. Nam, D. Y. Oh, D. Y. Oh, Y. S. Jung.,
“Toward practical all-solid-state lithium-ion batteries with high energy density and safety:
Comparative study for electrodes fabricated by dry- and slurry-mixing processes”. Copyright 2018,
Journal of Power Sources



RightsLink®

Home

Account
Info

Help



Title: Toward practical all-solid-state
lithium-ion batteries with high
energy density and safety:
Comparative study for
electrodes fabricated by dry-
and slurry-mixing processes

Author: Young Jin Nam, Dae Yang
Oh, Sung Hoo Jung, Yoon Seok
Jung

Publication: Journal of Power Sources

Publisher: Elsevier

Date: 31 January 2018

© 2017 Elsevier B.V. All rights reserved.

Logged in as:

Young Jin Nam

LOGOUT

Please note that, as the author of this Elsevier article, you retain the right to include it in a thesis or dissertation, provided it is not published commercially. Permission is not required, but please ensure that you reference the journal as the original source. For more information on this and on your other retained rights, please visit: <https://www.elsevier.com/about/our-business/policies/copyright#Author-rights>

BACK

CLOSE WINDOW

Copyright © 2018 [Copyright Clearance Center, Inc.](#) All Rights Reserved. [Privacy statement.](#) [Terms and Conditions.](#)
Comments? We would like to hear from you. E-mail us at customer@copyright.com

* Chapter 4.2.1. is reproduced in part with permission of Y. J. Nam, K. H. Park, D. Y. Oh, W. H. An, Y. S. Jung., "Diagnosis of failure modes for all-solid-state Li-ion batteries enabled by three-electrode cells". Copyright 2018, Journal of Materials Chemistry A



RightsLink®

Account
Info

Help



Title: Journal of materials chemistry.
A, Materials for energy and
sustainability

Article ID: 2050-7496

Publication: Publication1

Publisher: CCC Republication

Date: Jan 1, 2013

Copyright © 2013, CCC Republication

Logged in as:
Young Jin Nam
Account #:
3001380176

LOGOUT

Order Completed

Thank you for your order.

This Agreement between Young Jin Nam ("You") and Royal Society of Chemistry ("Royal Society of Chemistry") consists of your order details and the terms and conditions provided by Royal Society of Chemistry and Copyright Clearance Center.

License number	Reference confirmation email for license number
License date	Dec, 18 2018
Licensed content publisher	Royal Society of Chemistry
Licensed content title	Journal of materials chemistry. A, Materials for energy and sustainability
Licensed content date	Jan 1, 2013
Type of use	Thesis/Dissertation
Requestor type	Publisher, not-for-profit
Format	Print, Electronic
Portion	chapter/article
The requesting person/organization	First author / UNIST
Title or numeric reference of the portion (s)	All
Title of the article or chapter the portion is from	N/A
Editor of portion(s)	N/A
Author of portion(s)	N/A
Volume of serial or monograph	N/A
Page range of portion	
Publication date of portion	2019/02/28
Rights for	Main product
Duration of use	Life of current edition
Creation of copies for the disabled	no
With minor editing privileges	no
For distribution to	Worldwide
In the following language(s)	Original language of publication
With incidental promotional use	no
Lifetime unit quantity of new product	Up to 499
Title	All-Solid-State Lithium-Ion Batteries using Sheet-Type Electrodes and Solid Electrolyte Films and Their Diagnostic Study

Institution name	UNIST
Expected presentation date	Feb 2019
Requestor Location	Mr. Young Jin Nam Suwon
	Suwon, 16699 Korea, Republic Of Attn: Mr. Young Jin Nam
Billing Type	Invoice
Billing address	Mr. Young Jin Nam Suwon
	Suwon, Korea, Republic Of 16699 Attn: Mr. Young Jin Nam
Total (may include CCC user fee)	0.00 USD
Total	0.00 USD

CLOSE WINDOW

Copyright © 2018 [Copyright Clearance Center, Inc.](#) All Rights Reserved. [Privacy statement](#). [Terms and Conditions](#).
Comments? We would like to hear from you. E-mail us at customercare@copyright.com

